SIMULATION OF SILICON AND DIAMOND DETECTOR SYSTEMS BY GEANT4 SIMULATION TECHNIQUES

Nicholas Rattray Erasmus

A thesis submitted in partial fulfillment of the requirements for the degree
of
Magister Philosophiae in the Department of Physics,
University of Western Cape

Supervisor: J.N. Orce, University of the Western Cape
Co-supervisor: S. Halindintwali, University of the Western Cape

June 2014

Declaration

I declare that *SIMULATION OF SILICON AND DIAMOND DETECTOR SYSTEMS BY GEANT4 SIMULATION TECHNIQUES* is my own work, that it has not been submitted for any degree or examination in any other university, and that all sources I have used or quoted have been indicated and acknowledged by complete references.

Nicholas Rattray Erasmus June 2014

Signature:

Abstract

There is a constant need for improvement in nuclear particle detection methods. Silicon surface barrier detectors have proved very valuable during the last decades. Diamond is a viable alternative to silicon as a semiconductor detector. It offers significant advantages over silicon due to its high radiation hardness and low drift currents.

A Coulomb-excitation study has been carried out at TRIUMF using a 59.7 MeV ^{12}C beam impinging on a ^{194}Pt target. The particles underwent elastic Rutherford scattering in the target, and a double sided silicon S3 CD detector was used to measure the resulting particle energy spectra. These spectra were simulated in GEANT4 and compared to the experimental results. Subsequently, the silicon was replaced with diamond and the simulation was repeated. Such simulations of particle energy spectra, properly incorporating elastic Rutherford scattering, have not been carried out with GEANT4 before.

An accurate simulation of the elastic peak obtained from particle spectra will provide a methodology for applying particle-gamma coincidence techniques. The study of the inelastic peak in ^{12}C and similar nuclei will benefit from such developments. Such simulations will also offer high energy calibration points for the experimental data, and the possibility of testing the experimental conditions including the target thickness, beam energy, and linearity of electronic modules (e.g. the preamplifier).

The simulation offered results comparable to the experimental case. GEANT4 was found to simulate the Rutherford cross sections at specific scattering angles as well as the position of the simulated energy peaks accurately when compared with the experimental case. As expected, the experimentally obtained particle energy spectra displayed more broadening than the simulated spectra, though the shape of the peaks were very similar.

The simulation of the double sided diamond detector was a tentative first step in its testing as a particle detector. The sophisticated methods required to properly simulate and test diamond for nuclear physics experiments were not implemented. This simulation may serve as a starting point for further testing of diamond detectors, using advanced simulation techniques.

Acknowledgments

Firstly, I would like to thank my supervisor, Prof. Nico Orce, for his great enthusiasm for physics and his never-say-die attitude. Specifically, I would like to thank him for refusing to let me quit when I was on the verge of doing so. In hindsight, I am grateful for the challenging project he gave me to do.

I am most indebted to Jeyasingam Jeyasugiththan (Sugi) from the University of Cape Town for helping me learn GEANT4. He gave a great deal of his valuable time whilst helping me and did this without any type of obligation. I'm also grateful to have had someone share in my frustrations regarding the simulation of Rutherford scattering in GEANT4.

At UWC I would like to thank Prof. Robbie Lindsay, who gave me the opportunity to study physics again after 3 years in the wild. And thank you to my co-supervisor, Dr. Sylvain Halindintwali for his help with this work.

To all the others that gave me physics related help; Dr. Steve Peterson from UCT for his excellent "Introduction to GEANT4" workshop, Dr. Alexander Howard from CERN who took an interest in the problem I had with simulating Rutherford scattering, and the fine researchers from iThemba LABS who allowed me to partake in experiments there over the weekends these last two years - thank you.

On a personal note, I would like to thank my family, especially my Mother and Johan, for their continuing support and love. And to Ruan who allowed me to live for free with him for a whole year when I didn't know where else to go - thanks my friend, I don't know what I would have done without your help.

A special thank you to Nasreen who inspired me to take pride in my work and gave me invaluable encouragement and support throughout this time. You have been phenomenal.

Table of Contents

Contents

List of Figures

List of Tables

1 Introduction

A remarkable feature of atomic nuclei, particularly for those along or close to the valley of stability, is their ability to adopt different shapes for a small cost in energy compared to their total binding energy (see figure 1). Nuclear shapes are important for understanding phenomena such as beta decay, shape coexistence, and collective nuclear motion. Nuclear shapes can be determined using Coulomb excitation reactions at energies well below the Coulomb barrier so as to avoid unknown nuclear excitations.

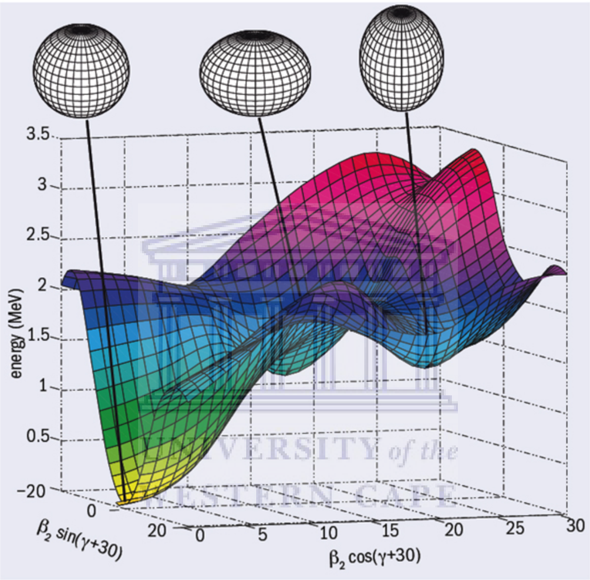

Figure 1: The different shapes and configurations of ^{186}Pb. [6].

The spectroscopic quadrupole moment, or the nuclear charge distribution in the laboratory frame, of excited states with angular momenta $J \neq 0$ or $\pm 1/2$ can be determined using the reorientation effect, RE, which generates a time-dependent hyperfine splitting of the nuclear levels [1]. This spectroscopic quadrupole moment gives a measure of the charge distribution of the nucleus, and hence describes its deviation from a spherical shape [3]. The population of different magnetic substates in the beam (target) nucleus, through the time-dependent electric-field gradient of the target (beam), depends on the particular spectroscopic quadrupole moment, either enhancing or inhibiting the asymmetry of the angular distribution of the de-excitation gamma-rays. This change in the angular distribution as a function of the scattering angle θ of the incident beam provides a spectroscopic probe for the measurement of the spectroscopic quadrupole moment.

A relevant point regarding RE measurements of accelerated ions is the use of high-Z targets, which enhances the RE because of the stronger time-dependent field gradient. The combination of accelerated beams of physical interest and heavy targets yield higher statistics and a more precise measurement of the nuclear charge distribution. Hence, the relevance of developing new beams and particle-detection techniques with large and precise angular coverage to accommodate new nuclear physics research at facilities such as iThemba LABS.

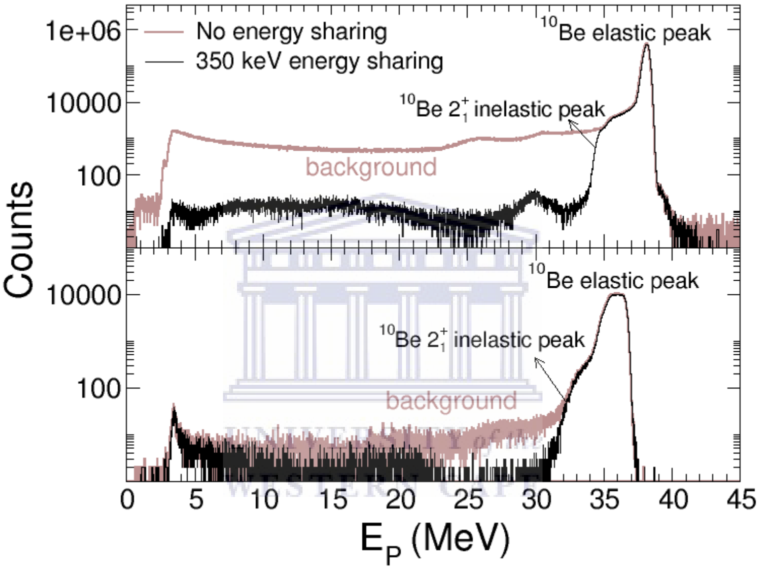

Figure 2: Typical particle energy spectra for the innermost ring (top) and outermost ring (bottom) with and without an energy sharing condition [2].

Collective states, mainly, are populated in Coulomb-excitation reactions, with the nucleus being excited from the ground state. Typical cross sections yield relatively small inelastic peaks for these excited states compared to the overwhelming elastic peak. Figure 2 shows the particle energy spectra of a ^{194}Pt(^{10}Be,^{10}Be*)^{194}Pt* reaction at 41 MeV used for particle-γ coincidence measurements with doubled sided silicon detectors. A typical feature of semiconductor detectors is the noise associated with charge sharing between the active layers and the dead layers in the detector. The double sided silicon CD detector enables a typical energy sharing condition of $\mid E_{ring} - E_{sector} \mid \leq 350$ keV which permits a good identification of the 2_1^+ inelastic peak at 3,368 keV in ^{10}Be. The reduction of the background noise due to this condition is shown in figure 2. The increase in scattering angle results in the peak (bottom spectrum) being at lower energy, broadened significantly and having fewer counts.

For an accurate characterization of the inelastic peak in such particle energy spectra, a detailed understanding of the shape and position of the elastic peaks through the different angular ranges in the silicon detector is important. This work aims at simulating the elastic peaks of an incident ^{12}C beam through a 3 mg/cm^2 ^{194}Pt target at different angular coverages in a doubled-sided S3 silicon detector using GEANT4 [12] and comparing these simulations with previous experimental work at TRIUMF [11].

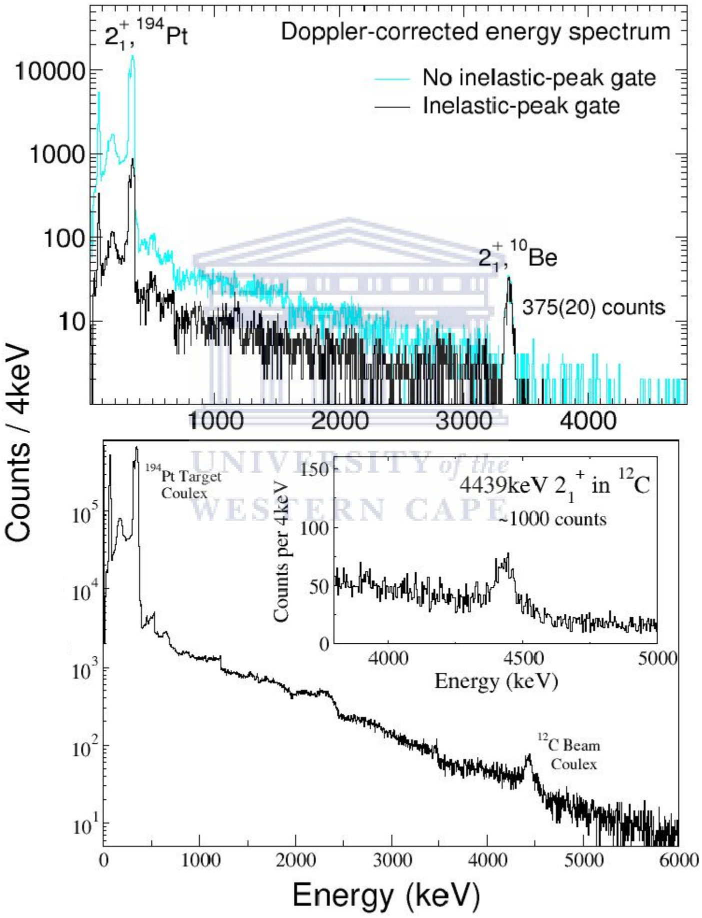

Figure 3: Gamma-ray energy spectra obtained by application of an inelastic-peak gate through particle-γ coincidence techniques (top panel) [2], and an example of a γ-ray spectrum without any particle tagging condition (bottom panel). The overwhelming background in the latter shows the power of the particle-γ coinicidence technique.

The first practical reason for an accurate simulation of the elastic peak is to be able to avoid reaction products arising from the elastic peak (e.g. from the ^{nat}Si(^{12}C, X) fusion-evaporation reaction, where X are the evaporated particles), which would permit a cleaner coincidence condition by precisely tagging in the region of interest in the particle spectra. As shown in figure 3, this coincidence technique yields clean γ-ray spectra for offline data analysis. For this purpose, a good simulation of the shape of the elastic peak is required. A second relevant point concerns the experimental conditions: an accurate simulation of the elastic peak centroids will permit testing deviations in the beam energy, target thickness and electronics performance. For example, the linearity of the preamplifiers within its characteristic energy range may be tested since the extrapolation of a typical α-source calibration toward higher energies may be inaccurate due to a nonlinearity of the preamplifiers at the high beam energies involved in Coulomb-excitation studies. In any case, the increasing stopping powers involved for larger apparent thicknesses as the ring angular coverage increases and an accurate reproduction of elastic Rutherford scattering have to be simulated accurately for these purposes.

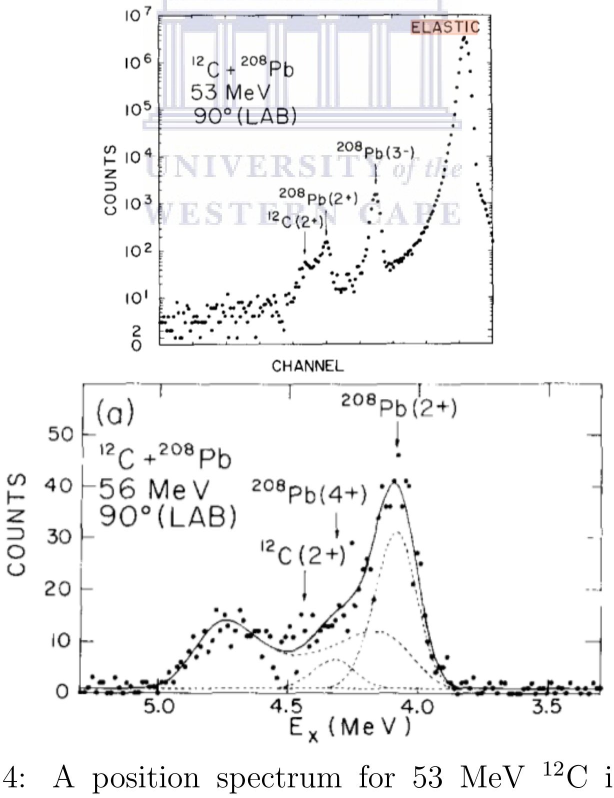

Figure 4: A position spectrum for 53 MeV ^{12}C incident on ^{208}Pb (top panel), including both elastic- and inelastic-scattering peaks, and a plot extracted from a similar spectrum, but at 56 MeV, for the relevant excitation energies (bottom panel) [5].

The deformation of the ^{12}C nucleus is an important quantity for understanding the structure of light nuclei. For example, α-clustering models predict the ground state of ^{12}C to be oblate. Early calculations of ^{12}C deformations have ranged from spherical to strongly oblate [10]. The most accurate value of the spectroscopic quadrupole moment of the first excited state of ^{12}C, $Q_s(2_1^+)$, was determined through the use of the RE [5]. In this case however, only particle energy spectra were used, which accounts for the large uncertainty in the value ($Q_s(2_1^+) = +0.06(3)$ eb). The effect of the overwhelming elastic peak can be seen in figure 4. The poor definition of the peak corresponding to the 2_1^+ state in ^{12}C is also evident. Through the use of particle-γ coincidence techniques, a more accurate measurement of $Q_s(2_1^+)$ in ^{12}C is expected. GEANT4 simulations of the elastic peak offer the possibility of refining the techniques of making such a measurement.

The design and use of diamond semiconductor detectors for particle detection is an ongoing area of research. Due to irradiation, semiconductor detectors only operate for a certain lifetime. Along with several other benefits, the radiation hardness, and hence lifetime, of diamond is greater than that of silicon [19]. Particle detection used for particle-γ coincidence techniques would thus benefit from the development of diamond detectors. A first attempt at simulating a diamond detector system with a geometry identical to the double sided silicon S3 detector through GEANT4 simulation techniques is presented in this work.

In conclusion, an accurate simulation of particle spectra will benefit any future experiments at iThemba LABS involving particle-γ coincidence measurements – either understanding shape coexistence and nuclear chirality or determining the photon strength function and nuclear lifetimes.

2 Semiconductor Detectors

Silicon detectors are the most widely used semiconductors for charged particle detection. Their applications range from the detection of leptons, quarks, gluons, gauge bosons and the search for the Higgs boson on the scale of $< 10^{-20}$m and extend to investigations on the scale of the entire Universe ($> 10^{28}$m). In between these extreme scales, they are used in Nuclear Physics experiments, Crystallography and Medical Physics. The GEANT4 simulation described in section 4 uses a silicon CD detector to measure the energy and position of the scattered beam particle from the recoiling target. In this section, the principle of operation and theory of semiconductor detectors [34] is presented along with the description of a silicon S3 CD detector.

2.1 Theory of Semiconductor Particle Detectors

Semiconductor detectors are made of crystalline semiconductor materials such as silicon or germanium. They are widely used in nuclear physics and particle physics for the detection of traversing charged particles or the absorption of photons. Semiconductors are defined as insulators with small forbidden band gaps. The operating principle behind silicon and germanium detectors is identical, but germanium is more widely used for gamma-ray detection. Crystal type detectors systems were first explored in the 1930s [34], but were only available commercially since the 1960s. The basic operating principle in semiconductors detectors is analogous to that of gas ionization devices, but the solid-state semiconductor holds several advantages such as greater energy resolution, faster response times and greater stopping power.

2.1.1 Band Theory of Solids

In a solid such as silicon, the lattice structure of crystalline materials creates a periodic potential that exhibits two energy bands that participate in the electrical conductivity of the material. The energy gap between these two bands, the conduction band and the valence band, determines whether the material is classified as a conductor, semiconductor or insulator. Figure 5 schematically represents this structure of a valence band, a “forbidden” energy gap and a conduction band for a hypothetical insulator, conductor and semiconductor. The electrons in the valence band are tightly bound and not free to move, whereas the electrons in the conduction band have enough energy to move through the entire crystal and thus contribute to the electrical conductivity of the material.

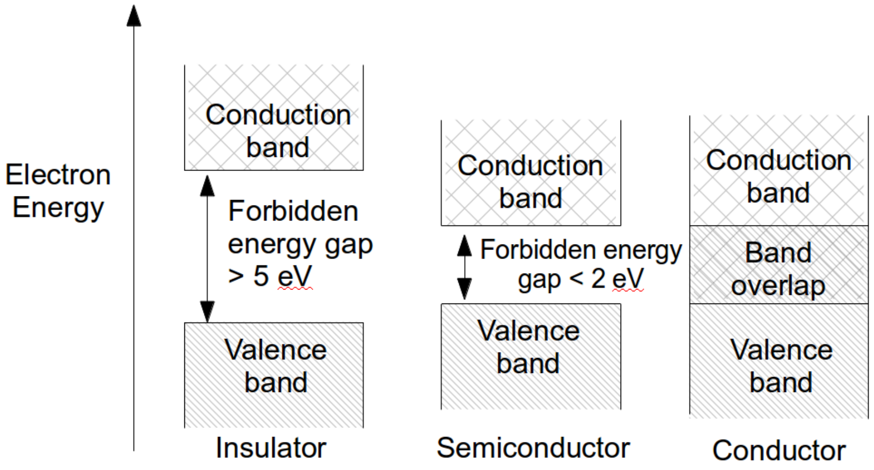

Figure 5: The energy band structure in various materials.

The aforementioned energy bands are not actually continuous energy levels. Because of the close, periodic arrangement of the atoms in the crystal, the electron wavefunctions overlap to cause many discrete energy levels that are so closely spaced that they can be considered to be continuous. The Pauli exclusion principle forbids more than one electron in the same state, and this causes the degeneracy in the outer atomic shells to break and form many discrete energy levels that are only slightly separated from each other. There are thus as many energy levels as there are pairs of electrons in the crystal. This degeneracy breaking does not affect the inner atomic levels however, since they are screened from each other.

The size of the band gap is determined by the lattice spacing between the atoms in the material. This spacing is therefore dependent on the temperature and pressure of the material. For germanium, the band gap is very small at room temperature, and the electrons are excited from the valence band to the conduction band too easily which results in too much electrical noise for useful spectroscopic data. It is for this reason that germanium detectors need to be cooled down considerably [35]. For an insulator,this gap is large, typically 5 eV or more, whereas a substance behaves like a semiconductor whenever the gap is less than 2 eV. In a conducting material the valence band and conduction band overlap so that there is no energy gap. The electrons are thus free to migrate throughout the material.

2.1.2 Charge Carriers in Semiconductors

In the lowest energy state of a semiconductor (at 0 Kelvin), all the electrons in the valence band are bound between the atoms by covalent bonds. In both silicon and germanium there are four valence electrons in the lattice structure. At room temperature, thermal excitation leads to some of these valence electrons being excited into the conduction band, leaving a vacancy or *hole* behind. This hole may then be filled by a neighbouring electron in the valence band, and when this process repeats, the hole appears to migrate through the crystal. When an external electric field is applied to this system, a negative current will flow in the direction of the electric field due to the free electrons in the conduction band. Conversely, the hole states will move in the opposite direction to the electrons and act as positive charge carriers. While a conducting material has only electrons that act as charge carriers, both the electrons in the conduction band and the holes left behind in the valence band act as charge carriers in semiconductors.

Due to thermal excitation, electron-hole pairs are constantly being created inside the semiconductor material. Many of these electron-hole pairs recombine spontaneously, and the difference between the number of created electron-hole pairs and those that recombine gives the effective number of charge carriers created by the excitation process. When conditions are stable, an equilibrium concentration of these electron-hole pairs is established. If n_i, also known as intrinsic carriers, denotes the concentration of electron-hole pairs and T the temperature, then

$$n_i = \sqrt{N_c N_v} exp\left(\frac{-E_g}{2kT}\right) \tag{1}$$

where N_c represents the number of states in the conduction band, N_v the number in the valence band, E_g the energy gap between the valence band and the conduction band of the material at 0 K and k the Boltzmann constant. In silicon, the typical value for n_i at room temperature is on the order of 10^{10} cm^{-3}. Considering that there are about 10^{22} atoms.cm^{-3} in silicon, this means that only about 1 in 10^{12} atoms in silicon is ionized.

2.1.3 Doped Semiconductors and the pn Semiconductor Junction

In a pure semiconductor, the number of holes in the valence band equals the number of electrons in the conduction band. By doping the crystal with a small amount of impurity atoms, this balance is changed in order to improve the efficiency of the production of charge carriers in the crystal. Such a crystal is called a *doped* or *extrinsic* semiconductor.

For semiconductors, a pentavalent[1] dopant, conventionally phosphorous, is used to provide extra electrons in the conduction band, and a trivalent[2] dopant, conventionally boron, to provide extra holes in the valence band. Crystals that are heavily doped with a pentavalent or a trivalent impurity are called n-type semiconductors and p-type semiconductors respectively.

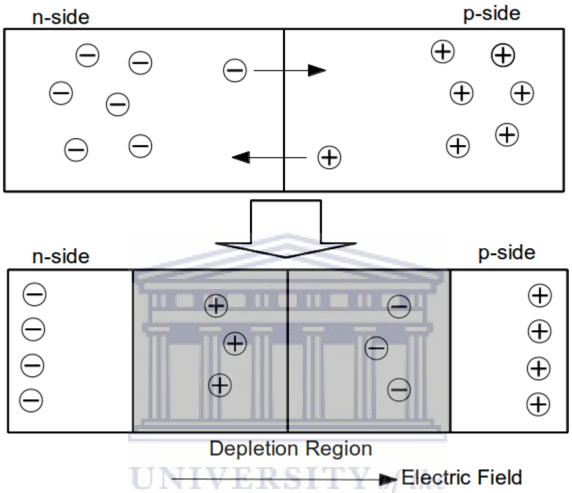

Figure 6: The depletion region of the PN-Junction in a doped semiconductor.

All semiconductor detectors function on the basis of a so-called semiconductor-junction. This configuration is usually obtained by diffusing p-type impurities into one end of a n-type semiconductor so that the end becomes p-type. This formation of a pn junction creates a zone between the two materials known as the depletion region. The difference in the concentration of electrons and holes between the two materials causes an initial diffusion of electrons toward the p-side and holes toward the n-side. Within the depletion region then, electrons fill up holes on the p-side and holes capture electrons on the n-side of the junction. This situation is illustrated in figure 6. This diffusion of electrons and holes causes an intrinsic electric field to form across the junction pointing in the direction of the p-side. This electric field prevents any further diffusion of holes or electrons leaving a region of immobile space charge known as the depletion region. This configuration causes any electron that enters this region to be swept toward the n-side,

---

[1] A pentavalent dopant has 5 electrons in its outer shell.

[2] A trivalent dopant has 3 electrons in its outer shell.

and any hole will conversely be be swept toward the p-side of the junction. It is this property of the pn junction that is exploited in radiation detection.

2.1.4 Reverse Biasing of Semiconductor Diode Detectors

When a nuclear particle enters a crystalline material it loses energy through interactions with the electrons in the semiconductor. Two principal processes can then occur [35]. The particle can ionize the crystal by exciting an electron from the valence band to the conduction band which creates a free electron and a free hole. Or it can excite an electron to a band located just below the conduction band. The electron and hole pair can remain bound in this state, and can move freely through the material. This is known as an exciton. A crystal that contains impurity atoms can then have locally created electronic levels in the forbidden energy gap. This happens when the impurity atom is ionized by a migrating free hole or electron hole pair. An electron that migrates into this region may then fall into the opening left by the hole and de-excite from its excited state to the ground state. If such a transition mode is allowed, then the electron will emit the corresponding radiation, otherwise the impurity center becomes a *trap* and the energy is lost to other subsequent processes. The contribution of the first process, the excitation of an electron to the conduction band, contributes the majority of the energy loss of the incident particle, and the other process can thus be ignored [34].Because of the small forbidden energy gap in Si, an *average* energy of about 3 eV is required for this process. This is much smaller than the *average* required energy of about 30 eV for a typical inert gas-filled ionization detector.

Let ϵ denote this *average* energy required to create an electron-hole pair. If the total energy loss of the charged particles in a p-n junction is ΔE, then the total number of electron-hole pairs produced is given by:

$$\text{Number of Electron-Hole Pairs} = \Delta E/\epsilon \tag{2}$$

The electric field in the depletion region then causes the electrons and holes to accumulate on the n-side and p-side of the p-n junction respectively. By applying a charge sensitive preamplifier to this configuration, a signal can be created on each side of the junction.

As is expected from the preceding discussion, the strength of the intrinsic electric field is proportional to the width of the depletion region. However, this intrinsic electric field which is caused by the initial diffusion of charge carriers is, in general, not strong enough for efficient charge collection. Because of this an external bias is required for signal collection. If a forward bias is applied to the p-n junction, from the p-side to the n-side, the intrinsic electric field of the depletion region will be canceled which would cause the energy gap to disappear and then the p-n junction would simply be a conductor. If, however, a reverse bias is applied across the depletion region, then the potential between the p-n junction will increase which results in a broadening of the width of the depletion region and a consequent increase in the charge collection. One would obviously like to increase this external bias as much as possible, but there is of course a limit to this process, exceeding which the p-n junction diode is destroyed.

2.2 Double Sided Silicon S3 CD Detector

The silicon S3 CD detector on which this work is based was developed by the Edinburgh-Louvain collaboration [8] for Coulomb Excitation and charged-particle reactions with radioactive ion beams. The detector is small enough to be mounted inside a target chamber as it was done at the TIGRESS spectrometer [11] where the data presented in this thesis were taken from. Figure 7 is a photo of the CD detector mounted in the BAMBINO scattering chamber at TRIUMF. The detector was used as an end detector in the experiment and simulations, and has been tested extensively for this purpose [24]. Section 2.2.1 describes this silicon S3 CD detector.

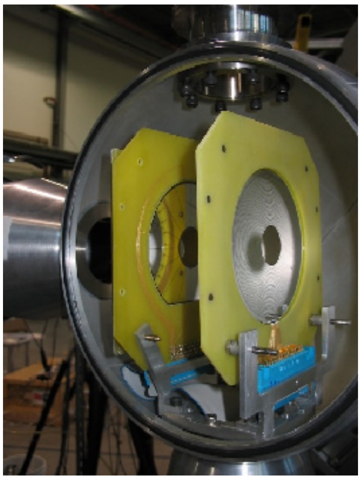

Figure 7: Photo of a mounted S3 detector at forward angles (right) and a S2 detector at backward angles (left) in a scattering chamber at TRIUMF.

2.2.1 Description and Dimensions of a Silicon CD Detector

The silicon S3 CD detector is a microstrip detector. That is, in order to detect not only the energy deposited by an particle that hits the detector, but also its position, there is a discrete array of many silicon microstrips. Because each microstrip element gives its own readout through which a signal can be observed, the detector thus gives position information of the particle that caused the signal. There are two types of position sensitive detectors. Along with this silicon microstrip detector, there is also the continuous position sensitive detector [8].

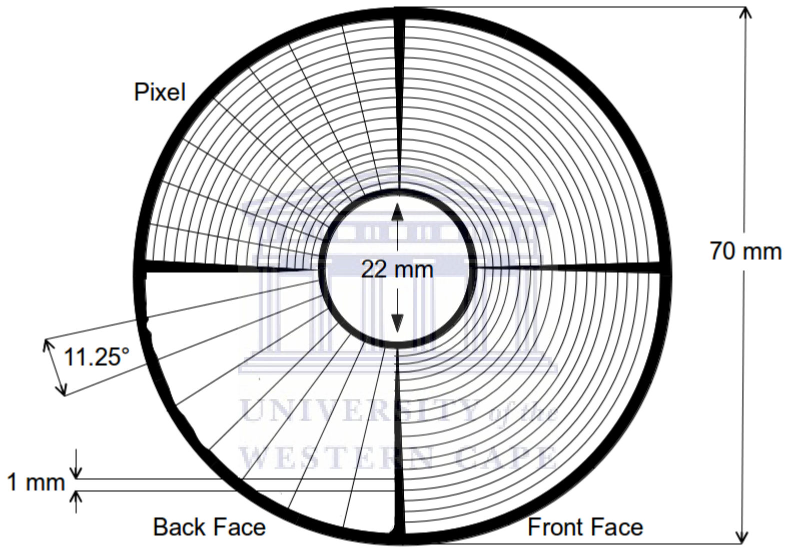

Figure 8: Schematic of the silicon S3 CD detector.

The CD detector has dimensions similar to that of an actual compact disc, which is why it is called a CD detector. It has an inner diameter of 22 mm and an outer diameter of 70 mm. It has 24 annular strips of width 1 mm on the front and 32 sectors of equal size at the back. This is represented graphically in figure 8. The two right-hand quadrants show the 24 annular strips on the front of the detector. The bottom left quadrant of the schematic shows the back view of the detector with its sectors, while the top left quadrant shows how the quasi pixels are formed by the overlap of the front and back strips. Throughout this work the 24 rings will be labeled alphabetically from A to X with A being the innermost ring and X the outermost. The 32 sectors will be numbered from 1 to 32. In the case of the sectors, the starting point is arbitrary. The hole in the center of the CD detector enables most of the beam particles to pass through the detector without damaging it.

Only the particles with larger scattering angles due to Rutherford scattering are stopped in the various rings and sectors of the detector. This greatly enhances the lifespan of the detector instrument.

The aforementioned dimensions of the silicon detector are its *total* physical dimensions. What is of importance in a simulation of high accuracy are the dimensions of the individual, active, silicon strips and sectors. In table 1 the exact specifications of the silicon S3 CD detector's annular rings are shown.

Table 1: Exact dimensions of each of the 24 annular rings of a silicon S3 CD detector.

Ring	Inner Radius (mm)	Outer Radius (mm)	Ring Width (mm)
A	11.480	12.366	0.866
B	12.466	13.352	0.866
C	13.452	14.338	0.866
D	14.438	15.324	0.866
E	15.424	16.310	0.866
F	16.410	17.296	0.866
G	17.396	18.282	0.866
H	18.382	19.268	0.866
I	19.368	20.254	0.866
J	20.354	21.240	0.866
K	21.340	22.226	0.866
L	22.326	23.212	0.866
M	23.312	24.198	0.866
N	24.298	25.184	0.866
O	25.284	26.170	0.866
P	26.270	27.156	0.866
Q	27.256	28.142	0.866
R	28.242	29.128	0.866
S	29.228	30.114	0.866
T	30.214	31.100	0.866
U	31.200	32.086	0.866
V	32.186	33.072	0.866
W	33.172	34.058	0.866
X	34.158	35.044	0.866

The detector is called *double sided* because of the two discrete arrays on its front and back. For a single sided silicon strip detector, only 1D information can be obtained, and thus the geometrical position of the signal's origin is not very well known. When a particle is incident on the double sided detector however, two concurrent signals are produced: one from the rings on the front side and one from the sectors on the back. Because these two layers of strips are orthogonal with respect to each other, the particle's position information is 2D. The resolution of its position is related to the quasi pixels shown in figure 8.

From the top left quadrant of the schematic, it can be seen that the position sensitivity of the detector is high. Indeed, at a typical distance of 5 cm from the target, the horizontal and azimuthal angular resolution is $\Delta\Theta = 2^\circ$and $\Delta\Phi = 3.4^\circ$respectively. The detector is slightly obstructed by the signal PCB tracks of the annular strips on its front side, which decrease the azimuthal angular coverage from 90°to 82°.

Silicon detectors are made in a variety of thicknesses depending on their intended use. A thin CD detector (of the order 10 μm) can be used for particle identification when combined with a residual detector [8]. However, the S3 detector described herein is used as an end-detector and thus has a much larger thickness of about 140 μm that allows the stopping of the relevant incident particle.

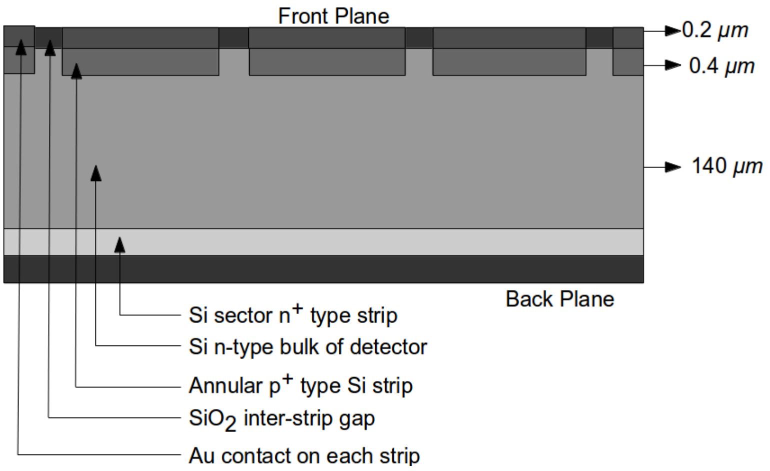

Figure 9: The cross section of silicon CD detector.

In figure 9 the cross section of the detector is shown. During fabrication, annular strips of p-type silicon are directly implanted on one side of the n-type silicon bulk, while sector strips of n-type silicon are implanted on the other side. The implantation depth for these layers is 0.4-0.5 μm. A gold contact of thickness 0.2-0.3 μm is implanted on the top of each strip. These gold contacts are insulated from each other by a SiO_2 gap which is also 0.2-0.3 μm thick.

For the type of experiment studied in this work, a notable benefit is offered by the array of rings and sectors in the CD detector. The rings offer a γ-ray angular distribution in correlation with the incident particles as a function of scattering angle, whereas the sectors provide Doppler correction for γ-rays emitted at typical particle velocities of $v/c \approx 0.1$.

2.3 Diamond Detectors

Diamond has several material qualities that make it a favorable candidate for particle detection in nuclear physics experiments [15]. Unlike silicon, the properties of diamond are not so strongly affected by damage due to high-doses of radiation [17]. Furthermore, charge collection is fast and the signal to noise ratio is good. Chemical vapour deposited (CVD) diamonds hold several advantages over natural diamonds. Geometrically, natural diamonds don't lend themselves well to being incorporated into a particle detection system since they are typically smaller than a few centimeters across. CVD diamonds however, can be deposited with a diameter up to 10 cm. Furthermore, CVD diamond is (in most cases) much more pure than natural diamond. Figure 10 is a basic representation of the cross section of a diamond detector.

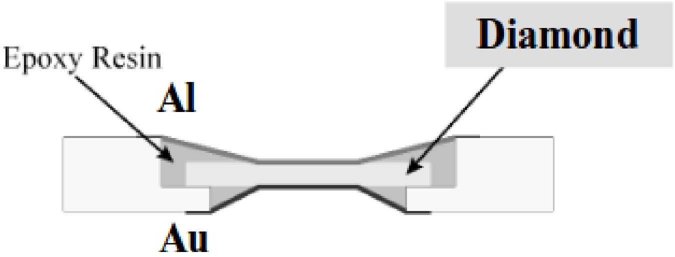

Figure 10: The cross section of a diamond detector. [16]

CVD diamonds are manufactured by passing the plasma or vapour of low pressure decomposed gases that contain carbon, such as methane, over a heated substrate. This substrate is heated, which causes the gases to break down and form diamond. The manufacturing process has seen several refinements [18] that eliminate the difficulties the material exhibits with regards to the sensitivity and stability of its detector response. These refinement techniques are generally related to the fine tuning of its growth conditions and device preparation. At present it is possible to manufacture CVD diamonds for detection purposes with thicknesses ranging from 5 μm to 500 μm, and these are being actively used in research centers such as the LHC at CERN. There are different variations of diamond detector technology, including hybrid detectors which use ideal CVD diamonds as the insulator in a silicon on insulator (SOI) substrate (see figure 11). Regardless of these variations, the benefits of using diamond, especially with regards to its radiation hardness, remain a crucial factor in the motivation behind such research.

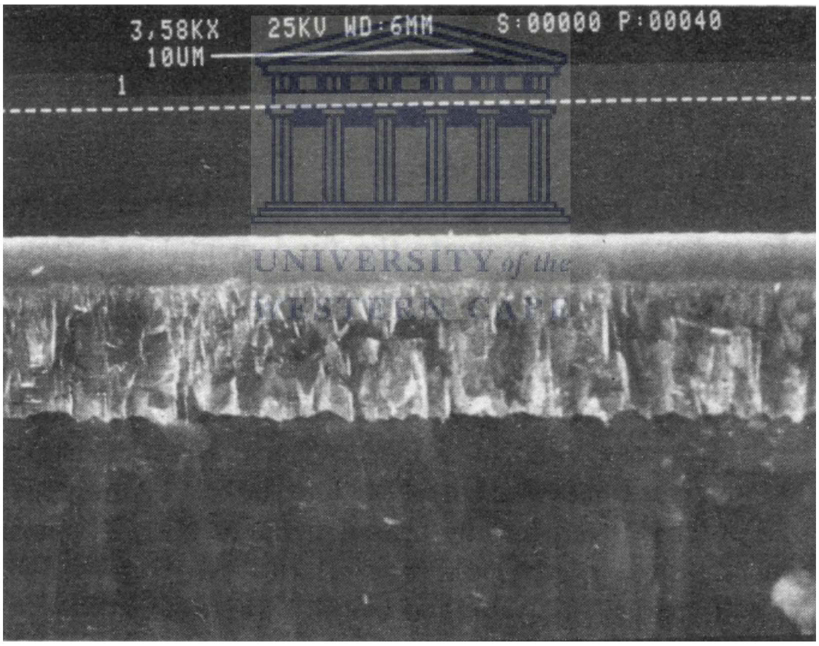

Figure 11: A cross sectional scan of silicon on diamond. The top and bottom layers are silicon and the middle layer diamond. The white scale marker represents 10 μm [19].

Semiconducting diamonds are attractive for electronic applications due to their superior transport properties compared to silicon [19]. For example, diamonds display electron-hole mobility on the order of 70 times greater than that of silicon [20]. It has also been found that silicon has a greater leakage current on the order of 1 nA or more than diamond [16]. Diamond holds all these benefits over silicon, whilst maintaining an energy resolution comparable to that of silicon - see figure 12.

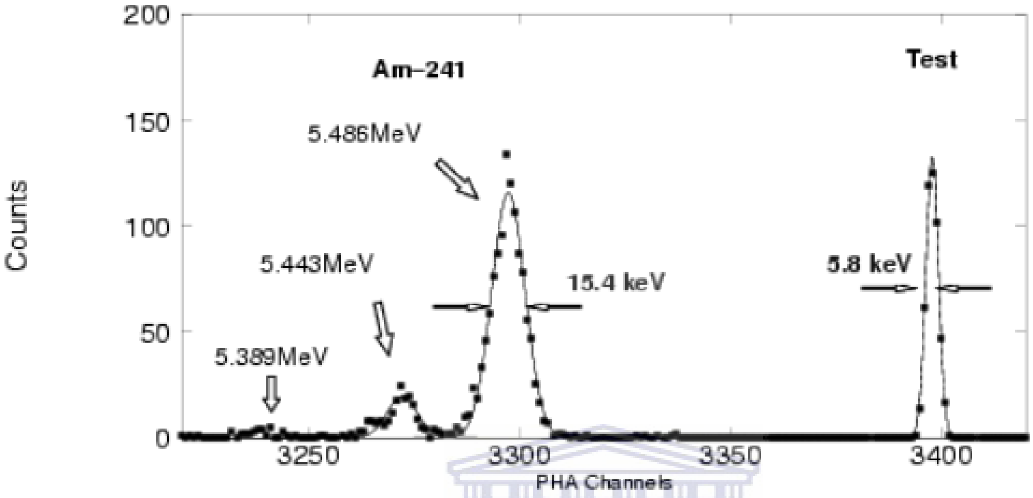

Figure 12: A test of the energy resolution in diamond detector systems [16].

3 Charged Particle Collisions, Energy Loss, Scattering

In this section the theory of charged particle collisions is presented, along with data from the SRIM calculations that correspond to the experiment detailed in section 5. The experiment (and simulation) that this work is based on was done at energies well below the Coulomb barrier, thus energy transfer due to (elastic and inelastic) Coulomb interaction is the principal process discussed. The theory of Rutherford scattering was one of the greatest breakthroughs in the study of nuclear phenomena. Therefore a detailed presentation on the development and findings of this theory is presented.

3.1 Rutherford Scattering Theory

In 1911, Ernst Rutherford discovered the atomic nucleus [7] by analyzing the scattering of α-particles by gold nuclei. This experiment was carried out under his direction by his students, Geiger and Marsden, and the interpretation of the results replaced Thomson's plum pudding model of the atom. The elastic Coulomb scattering of charged particles by the atomic nucleus is thus also known as Rutherford scattering.

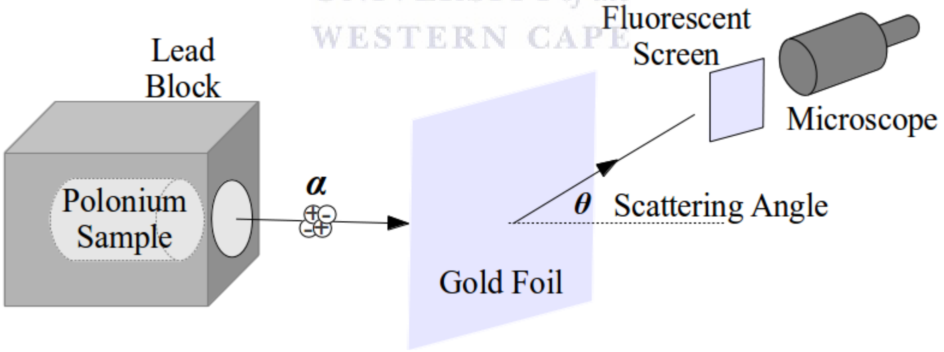

Figure 13: Geiger and Marsden's experiment.

The α-particles emitted by a radioactive sample were collimated with a lead block, and the focused beam of radiated α-particles were made to impinge upon a very thin gold foil. A fluorescent screen and microscope were then used to literally count the number of scattered particles at different angles. The α-particles were detected at angles that were too large to be explained by the prevailing model of Thomson. Based on these results, Rutherford postulated the nucleus, and nuclear physics was born.

The following were the only assumptions made by Rutherford in order to explain the experimental data: The atom contains a nucleus of charge Ze, where Z is the atomic number of the atom and e the magnitude of the electric charge of an electron, the nucleus may be treated as a point particle. The mass of the nucleus compared to the incident particle is large enough to ignore nuclear recoil, the collision is elastic, and only the laws of classical mechanics and electromagnetism are applicable to this phenomenon.

Consider the situation in which the incident particle hits the nucleus head-on. Let T be the particle's kinetic energy and ze it's electric charge. The distance of closest approach D is then obtained by equating the initial kinetic energy to the Coulomb energy at distance D

$$T = \frac{zZe^2}{4\pi\epsilon_0 D} \tag{3}$$

or when rearranged

$$D = \frac{zZe^2}{4\pi\epsilon_0 T} \tag{4}$$

As is shown in figure 14, such a collision would result in the α-particle reversing direction, i.e. the scattering angle θ would be equal to π. This is a special case however; it is far more likely that the collision will not be exactly head on. In the next section the relation between the scattering angle and impact parameter is derived for these cases.

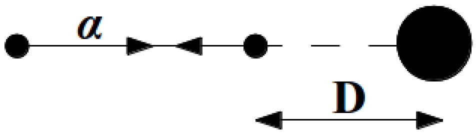

Figure 14: Distance of closest approach in a head-on collision.

3.2 Scattering Angle and Impact Parameter

The description of many physical processes are considerably simplified when the coordinate system is chosen to be at rest with respect to the center of momentum. The simplification of this center of mass (CM) frame is used in this section and in section 3.3 for the derivation of useful relationships in Rutherford scattering, while its relationship with the laboratory (LAB) frame is derived in section 3.4. Relativistic effects are ignored in these derivations.

A projectile particle with mass m_1 incident on a target particle with mass m_2 at rest in the LAB frame can be converted to an equivalent interaction in the CM frame. In the CM frame the total linear momentum of the system must be zero. If **p** is the momentum of m_1 in the CM frame, then m_2 will approach the collision point with momentum equal in magnitude to that of m_1, but in the opposite direction. Similarly, if **p'** is the momentum of m_1 after the collision, then m_2 will have momentum **-p'** after the collision. This scattering process in the CM frame is depicted in figure 15. Furthermore, the interaction force between these two particles is conservative, therefore, due to no energy being lost during the interaction, the magnitude of the final momentum vector **p'** is equal to the magnitude of the initial momentum vector **p**. This means that the entire collision event is completely specified if the scattering angle in the CM frame, ψ, is known.

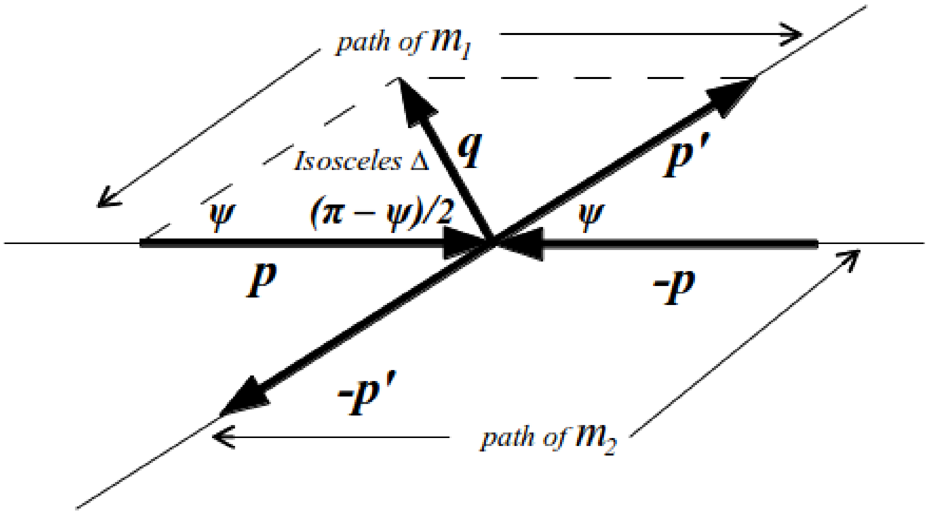

Figure 15: A collision between two particles in the CM frame.

This two-body interaction can be converted into an equivalent one-body interaction by letting $m_{eq} = m_1 m_2/(m_1 + m_2)$ and by assuming a fixed scattering potential for the interaction. This assumption is analogous to the assumption of zero nuclear recoil made by Rutherford, which is why the equavalent one-body diagram, as depicted in figure 15, may be used. Using Newton's Second Law of Motion, Coulomb's law provides the force exerted on m_{eq} by the stationary scattering potential. Together with this, the conservation of angular momentum allows the relationship between the impact parameter, b and the scattering angle, ψ, to be derived. If $\mathbf{q}$ is the change in momentum of m_p, then an isosceles triangle with angle ψ is formed as in figure 15. The vector $\mathbf{q}$ is in the same direction as the line joining the fixed scattering center to the point of closest approach in figure 16.

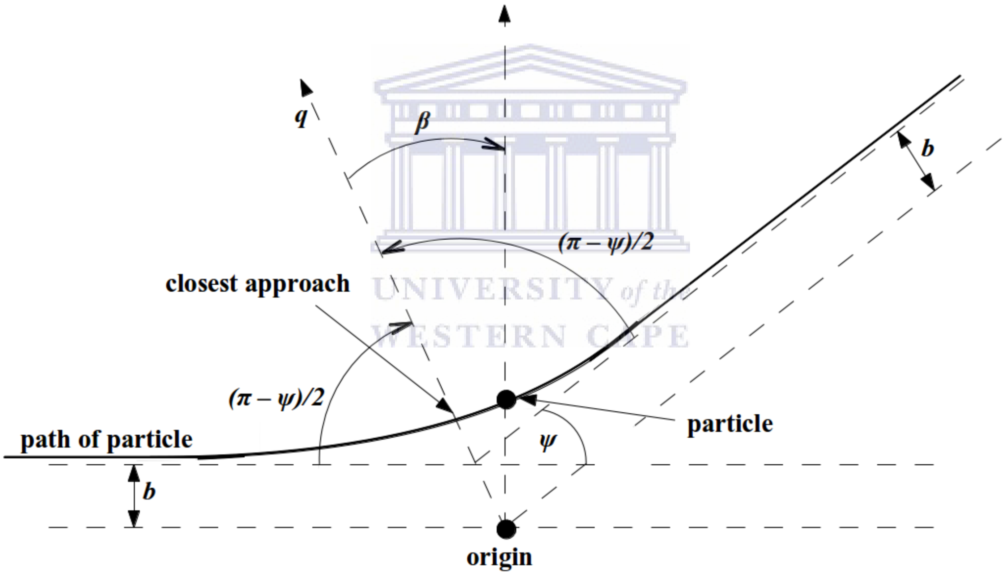

Figure 16: Rutherford scattering reduced to an equivalent 1-body interaction.

The position of m_{eq} can be described in terms of two-dimensional polar coordinates r and β with the fixed scattering center at the origin and $\beta = 0$ chosen as the point of closest approach. From Newton's second law, the rate of change of the momentum in the direction of $\mathbf{q}$ is equal to the component of the force acting on m_{eq} due to the fixed scattering potential at the origin. From Coulomb's law, the magnitude of this force is equal to

$$F = \frac{zZe^2}{4\pi\epsilon_0 r^2} \tag{5}$$

where Ze is the electric charge of m_2 and ze is the electric charge of m_1.

Combining equations 4 and 5, it follows that

$$F = \frac{TD}{r^2} \tag{6}$$

The component of this force in the direction of q is given by

$$F_q(t) = \frac{TD}{r^2} cos\beta(t) \tag{7}$$

From $F_q(t) = dq\ /dt$, it follows that

$$q = \int \frac{TD}{r^2} cos\beta \, \mathrm{d}t = \int \frac{zZe^2}{4\pi\epsilon_0 r^2} cos\beta \, \mathrm{d}t \tag{8}$$

Let $\dot{\beta} = d\beta/dt$. The integral over time can be replaced by an integral over the angle β by using

$$dt = \frac{d\beta}{\dot{\beta}} \tag{9}$$

where $\dot{\beta}$ is obtained from the conservation of angular momentum,

$$L = m_{eq} r^2 \dot{\beta} \tag{10}$$

The initial angular momentum is given by

$$L = bp \tag{11}$$

so that

$$\dot{\beta} = \frac{bp}{m_{eq} r^2} \tag{12}$$

Combining equations 8, 9 and 12, and using $T = p^2/2\mathrm{m}_{eq}$, it follows that

$$q = \int \frac{TDm_{eq}r^2}{r^2 bp} cos\beta \, \mathrm{d}\beta = \int \frac{Dp}{2b} cos\beta \, \mathrm{d}\beta \tag{13}$$

As shown in figure 16, the limits on β are $\pm 1/2(\pi - \psi)$, so that the integral resolves to

$$q = \frac{Dp}{2b} 2sin\frac{1}{2}(\pi - \psi) \tag{14}$$

From figure 16, the following can be obtained by using the sine rule,

$$\frac{q}{p} = \frac{\sin\psi}{\sin\frac{1}{2}(\pi - \psi)} = 2\sin\frac{\psi}{2} \tag{15}$$

Substituting this into equation 14,

$$2psin\frac{\psi}{2} = \frac{Dp}{2b} 2sin\frac{1}{2}(\pi - \psi) \tag{16}$$

from where the desired relation follows

$$tan(\frac{\psi}{2}) = \frac{D}{2b} \tag{17}$$

3.3 Flux and Cross Section

The number of incident particles arriving per unit area per unit time at the target is defined as the *flux*, F. The number of particles scattered into the area between the concentric rings in figure 17 is therefore given by:

$$dN(b) = F\pi(b+db)^2 - F\pi b^2 = F\pi(b^2 + 2b.db + db^2 - b^2) = F\pi(2b.db + db^2)$$

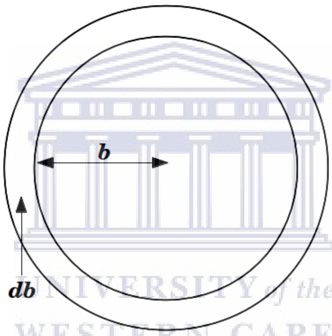

Figure 17: Geometrical representation of impact parameter.

If db is made arbitrarily small, then db^2 is negligible compared to $b.db$ so that $dN(b) \approx F2\pi bdb$. Substituting the result from the previous section, $tan(\psi/2) = D/2b$ and its derivative

$$db = -\frac{D}{4sin^2(\psi/2)}d\psi \tag{18}$$

into $dN(b) = F2\pi bdb$ gives

$$dN(\psi) = F\pi\frac{D^2}{4}\frac{cos(\psi/2)}{sin^3(\psi/2)}d\psi \tag{19}$$

This expression gives the number of particles scattered through an angle between ψ and ψ+$d\psi$. Note that the minus sign has been dropped as it is merely an indication that the scattering angle ψ decreases as b increases and $N(\psi)$ must be positive. From here, the *differential cross section* , $d\sigma/d\psi$, with respect to the scattering angle can be defined as the number of scatterings between ψ and $\psi + d\psi$ per unit flux, per unit range of angle, i.e.

$$\frac{d\sigma}{d\psi} = \frac{dN(\psi)}{Fd\psi} = \pi\frac{D^2}{4}\frac{cos(\psi/2)}{sin^3(\psi/2)} \tag{20}$$

The convention is to use the differential cross section with respect to a given solid angle Ω, which in terms of the scattering angle ψ and the azimuthal angle ϕ is given by

$$d\Omega = sin\psi d\psi d\phi = 2sin(\frac{\psi}{2})cos(\frac{\psi}{2})d\psi d\phi \tag{21}$$

From the definition of differential cross section and the fact that ϕ extends from 0 to 2π, it follows that $2\pi d\sigma/d\phi = 1$, so that

$$\frac{d\sigma}{d\psi} = 2\pi\frac{d^2\sigma}{d\psi d\phi} \tag{22}$$

By using equation 20, this can be expressed in terms of $d\sigma/d\psi d\phi$

$$\frac{d\sigma}{d\psi d\phi} = \frac{D^2}{8}\frac{cos(\psi/2)}{sin^3(\psi/2)} \tag{23}$$

From equation 21, $d\psi d\phi$ can be replaced by $d\Omega/(2sin(\psi/2)cos(\psi/2))$

$$\frac{d\sigma}{d\Omega} = \frac{D^2}{8}\frac{cos(\psi/2)}{sin^3(\psi/2)} \cdot \frac{1}{2sin(\psi/2)cos(\psi/2)} = \frac{D^2}{16sin^4(\psi/2)} \tag{24}$$

Recalling that $D = (zZe^2)/(4\pi\epsilon_0 T)$ (equation 4), this can be rewritten as

$$\frac{d\sigma}{d\Omega} = \left(\frac{zZe^2}{16\pi\epsilon_0 T}\right)^2 \frac{1}{sin^4(\psi/2)}. \tag{25}$$

This is the famous equation derived by Rutherford [7]. The equation shows that, due to the fourth power dependence of angle, the probability of finding a particle at larger and larger angles decreases very rapidly. The $\psi/2$ implies that backscattering at angles close to $\psi = \pi$ is very unlikely.

It is worth noting that this derivation is often done in the LAB frame by assuming that $m_2 >> m_1$. Indeed, Rutherford's original derivation made use of this assumption due to the much larger mass of a gold nucleus compared to that of an α-particle. Here it has been derived in the general sense, therefore the simplification offered by the CM frame was used. When formula 25 is applied in the general case, then the scattering angle in the LAB frame, θ, first needs to be converted to the corresponding angle in the CM frame, ψ. When $m_2 >> m_1$ is assumed then the equivalent 1-body problem visualized in figure 16 will be identical to the original 2-body problem in the LAB frame. In such a case $\theta \approx \psi$; this will be proved in the next section.

3.4 Connecting the LAB and CM Frames

The equations that connect CM frame and the LAB frame will be derived in this section. Once again, the only assumptions that are made with regards to this system is the conservation of energy and momentum.

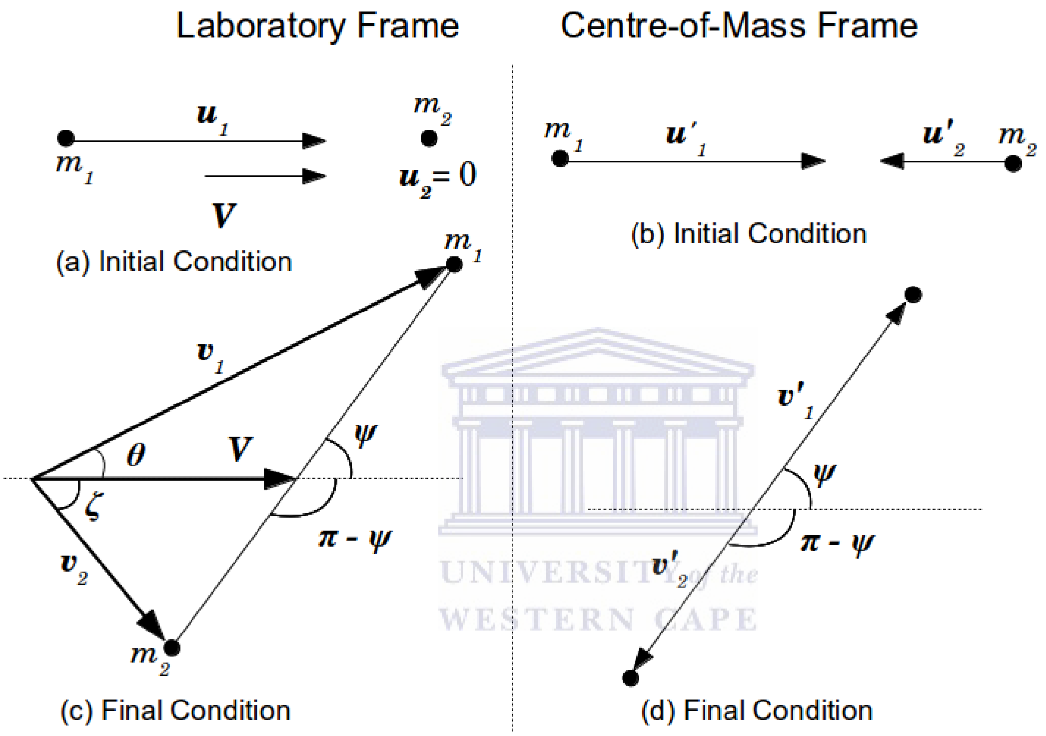

Figure 18: Geometry of an elastic collision in the LAB and CM Frames.

The geometry and notation is presented in figure 18. As can be seen from (b) and (d), the incident particle and the target move directly towards each other before the collision, and exactly in opposite directions after the collision. This is because the linear momentum in the CM frame is always zero. A description of the notation follows:

m_1 = Mass of the moving particle in the LAB system
m_2 = Mass of the stationary particle in the LAB system

In general, primed quantities refer to the CM system:

u_1 = Initial velocity of m_1 in the LAB system
v_1 = Final velocity of m_1 in the LAB system

u'_1 = Initial velocity of m_1 in the CM system
v'_1 = Final velocity of m_1 in the CM system

And similarly for u_2, v_2, u'_2 and v'_2 (but $u_2 = 0$):

T_0 = Total kinetic energy in LAB system
T'_0 = Total kinetic energy in CM system
T_1 = Final kinetic energy of m_1 in LAB system
T'_1 = Final kinetic energy of m_1 in CM system

And similarly for T_2 and T'_2:

V = Velocity of the center of mass in the LAB frame
θ = angle through which m_1 is deflected in the LAB system
ζ = angle through which m_2 is deflected in the LAB system
ψ = angle through which m_1 and m_2 are deflected in the CM system

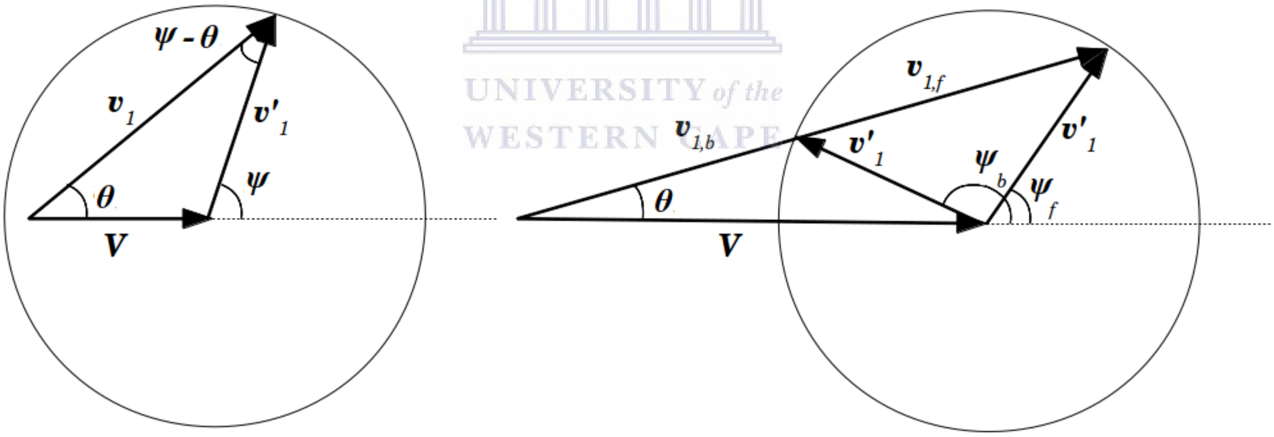

(a) $V < v'_1$

(b) $V > v'_1$

Figure 19: The double-valued final velocity of an incident particle.

In figure 19, the final state of the scattered particle m_1 is shown. Given the scattering angle ψ, the CM velocity V can then be added to the CM velocity v'_1 of the scattered particle. The possible vectors v'_1 then lie on a circle with a radius equal in magnitude to v'_1. The center of the circle is the terminus of the vector V. The LAB velocity v_1 and its corresponding scattering angle θ can then be obtained by connecting the point of origin of V with the terminus of vector v'_1.

Based on the above geometrical arguments, an important distinction is made between the case when $V < v_1'$ and $V > v_1'$. If $V < v_1'$, then only one possible relationship between V, v_1, v_1' and ψ exists. However, if $V < v_1'$, then two possible combinations of LAB velocities and scattering angles exist. The subscripts b and f in figure 19(b) refer to the fact that v_1 scatters *backwards* or *forwards* relative to the CM of the system respectively.

What follows is the derivation of the relationship between various quantities in these two frames of reference. Let $M = m_1 + m_2$. Then, from the definition of the center of mass ($\mathbf{R}$):

$$m_1\mathbf{r_1} + m_2\mathbf{r_2} = M\mathbf{R} \tag{26}$$

By taking the derivative with respect to time, this becomes

$$m_1\mathbf{u_1} + m_2\mathbf{u_2} = M\mathbf{V} \tag{27}$$

Because $\mathbf{u_2} = 0$ in the LAB frame, this equation can be rewritten as

$$\mathbf{V} = \frac{m_1\mathbf{u_1}}{m_1 + m_2} \tag{28}$$

Since m_2 is initially at rest, its velocity in the CM frame will be equal in magnitude to that of the center of mass, but in opposite direction. Therefore

$$\mathbf{u_2'} = -\mathbf{V} = -\frac{m_1\mathbf{u_1}}{m_1 + m_2} \tag{29}$$

Since the collision between the two particles is elastic and linear momentum is conserved, it follows that

$$u_1' = v_1',\ u_2' = v_2' \tag{30}$$

Which when put into equation 29 gives

$$v_2' = \frac{m_1 u_1}{m_1 + m_2} \tag{31}$$

And similarly for v_1'. Note that only the magnitudes are equated here. Since $u_1 = u_1' - u_2'$

$$v_1' = u_1 + u_2' = \frac{m_2 u_1}{m_1 + m_2} \tag{32}$$

From figure 19(a), it can be seen that

$$v_1' sin\psi = v_1 sin\theta \tag{33}$$

and

$$v_1' cos\psi + V = v_1 cos\theta \tag{34}$$

Dividing equation 33 by equation 34 gives

$$tan\theta = \frac{v_1' sin\psi}{v_1' cos\psi + V} = \frac{sin\psi}{cos\psi + (V/v_1')} \tag{35}$$

From equation 28 and equation 32, V/v_1' can be obtained

$$\frac{V}{v_1'} = \frac{m_1 u_1/(m_1 + m_2)}{m_2 u_1/(m_1 + m_2)} = \frac{m_1}{m_2} \tag{36}$$

This result states that the ratio m_1/m_2 determines which of the two scattering processes in figure 19 will take place. That is, figure 19(a) takes place when $m_1 < m_2$, and figure 19(b) takes place when $m_1 > m_2$. Equations 35 and 36 can be combined to give

$$tan\theta = \frac{sin\psi}{cos\psi + m_1/m_2} \tag{37}$$

This important result gives valuable insight into the scattering process. When $m_1 << m_2$, particle m_2 acts as a fixed scattering center and the LAB and CM frames are approximately equal:

$$\theta \approx \psi, \; m_1 << m_2 \tag{38}$$

For the experiment and simulation described in this work, a ^{12}C beam was made to impinge upon a ^{194}Pt target. In this case, $m_1/m_2 \approx 0.06$, so the approximation $\theta \approx \psi$ could be used for calculations that do not require high accuracy. In this work, the results are very sensitive to scattering angle. For an accurate calculation of differential cross sections, the scattering angle in the LAB frame will be converted to the scattering angle in the CM frame.

Therefore a formula for $\psi(\theta)$ is required. This can be obtained by setting $\tan\theta = \sin\theta/\cos\theta$ into equation 37 and multiplying by both sides with $(cos\psi + m_1/m_2)$:

$$cos\psi sin\theta + \frac{m_1}{m_2} sin\theta = sin\psi cos\theta \tag{39}$$

Using the fact that $sin(\psi - \theta) = sin\psi cos\theta - cos\psi sin\theta$, this can be rewritten as

$$sin(\psi - \theta) = \frac{m_1}{m_2} sin\theta \tag{40}$$

From where it follows that

$$\psi(\theta) = \theta + arcsin\left(\frac{m_1}{m_2} sin\theta\right) \cdot \tag{41}$$

In table 2 this equation is used to show the relationship between the LAB and CM scattering angles for a 59.7 MeV ^{12}C projectile and a ^{194}Pt target.

Table 2: Conversion of scattering angle from CM frame to LAB frame according to equation 37 for $m_1 = 12$ and $m_2 = 194$

θ (LAB)	ψ (CM)
0°	0°
10°	10.62°
20°	21.21°
30°	31.77°
40°	42.28°
50°	52.72°
60°	63.07°
70°	73.33°
80°	83.49°
90°	93.55°

3.4.1 Cross Sections

In addition to establishing a relationship between the angles in the LAB and CM frames, it is also of value to have such a relationship between the cross sections in these two frames. This can be obtained from the fact that the number of scattered particles moving through an infinitesimal cross section is the same in both frames. Let ϕ_1 and ϕ be the azimuthal angles in the LAB and CM frames respectively:

$$d\sigma(\theta, \phi_1) = d\sigma(\psi, \phi) \tag{42}$$

What differs in the two frames is the solid angle $d\Omega$. In the LAB frame $d\Omega_1 = sin\theta d\theta d\phi_1$ and in the CM frame $d\Omega = sin\psi d\psi d\phi$. We can therefore write

$$\begin{aligned} (\frac{d\sigma}{d\Omega_1})_{LAB} d\Omega_1 &= (\frac{d\sigma}{d\Omega})_{CM} d\Omega \\ (\frac{d\sigma}{d\Omega_1})_{LAB} &= (\frac{d\sigma}{d\Omega})_{CM} \frac{sin\psi}{sin\theta} \frac{d\psi}{d\theta} \frac{d\phi}{d\phi_1} \end{aligned} \tag{43}$$

Since there is cylindrical symmetry around the direction of the incident beam, it follows that $\phi_1 = \phi$. Therefore

$$(\frac{d\sigma}{d\Omega_1})_{LAB} = (\frac{d\sigma}{d\Omega})_{CM} \frac{d(cos\psi)}{d(cos\theta)} \tag{44}$$

From equation 37 and the fact that $cos\theta = 1/\sqrt{tan^2\theta + 1}$, it follows that

$$cos\theta = \frac{cos\psi + \frac{m1}{m2}}{\sqrt{1 + \frac{m_1^2}{m_2^2} + 2\frac{m_1}{m_2}cos\psi}} \tag{45}$$

Thus,

$$\frac{dcos\theta}{dcos\psi} = \frac{1 + \frac{m_1}{m_2}cos\psi}{(1 + \frac{m_1^2}{m_2^2} + 2\frac{m_1}{m_2}cos\psi)^{3/2}} \tag{46}$$

Combining this result with equation 44, it follows that

$$(\frac{d\sigma}{d\Omega_1})_{LAB} = \frac{(1 + \frac{m_1^2}{m_2^2} + 2\frac{m_1}{m_2}cos\psi)^{3/2}}{1 + \frac{m_1}{m_2}cos\psi} (\frac{d\sigma}{d\Omega})_{CM} \tag{47}$$

In the case where $m_2 >> m_1$, the LAB and CM cross sections are approximately equal, so that

$$\left(\frac{d\sigma}{d\Omega_1}\right)_{LAB} \approx \left(\frac{d\sigma}{d\Omega}\right)_{CM} \tag{48}$$

3.5 Energy Transfer in Elastic Collisions

In an elastic collision, the total energy of the system is the same before and after the collision, therefore

$$m_1u_1^2 = m_1v_1^2 + m_2v_2^2 \tag{49}$$

Rearranging this, gives

$$v_2^2 = m_1(u_1^2 - v_1^2) \tag{50}$$

Using the angles θ and ζ as defined in figure 18(c), the incident direction can be expressed as:

$$m_1u_1 = m_1v_1cos\theta + m_2v_2cos\zeta \tag{51}$$

Rearranging and squaring this gives

$$m_1^2u_1^2 + m_1^2v_1^2cos^2\theta - 2m_1^2u_1v_1cos\theta = m_2^2v_2^2cos^2\zeta \tag{52}$$

Since the initial momentum perpendicular to the incident direction is zero, it follows that

$$0 = m_1v_1sin\theta - m_2v_2sin\zeta \tag{53}$$

Rearranging and squaring gives

$$m_1^2v_1^2sin^2\theta = m_2^2v_2^2sin^2\zeta \tag{54}$$

Adding equations 52 and 54 gives

$$m_1^2u_1^2 + m_1^2v_1^2(cos^2\theta + sin^2\theta) - 2m_1^2u_1v_1cos\theta = m_2^2v_2^2(cos^2\zeta + sin^2\zeta) \tag{55}$$

Which is equal to

$$m_1^2u_1^2 + m_1^2v_1^2 - 2m_1^2u_1v_1cos\theta = m_2^2v_2^2 \tag{56}$$

Substituting equation 50 into the right side of this gives

$$m_1^2u_1^2 + m_1^2v_1^2 - 2m_1^2u_1v_1cos\theta = m_2m_1(u_1^2 - v_1^2) \tag{57}$$

Dividing both sides by $m_1^2u_1^2$ gives

$$1 + \frac{v_1^2}{u_1^2} - \frac{2v_1cos\theta}{u_1} = \frac{m_2}{m_1}(1 - \frac{v_1^2}{u_1^2}) \tag{58}$$

Rearranging this

$$\frac{v_1^2}{u_1^2}(1 + \frac{m_2}{m_1}) - \frac{2v_1cos\theta}{u_1} + (1 - \frac{m_2}{m_1}) = 0 \tag{59}$$

This is a quadratic equation of the form $aX^2 + bX + c = 0$ where $X = v_2/v_0$ with solution

$$X = \frac{-b \pm \sqrt{b^2 - 4ac}}{2a}$$

The solution to equation 59 is therefore

$$\frac{v_1}{u_1} = \frac{2cos\theta \pm \sqrt{4cos^2\theta - (1 - \frac{m_2}{m_1})(1 + \frac{m_2}{m_1})}}{2(1 + \frac{m_2}{m_1})} \tag{60}$$

Canceling the factor 2 and multiplying the factors under the root sign gives

$$\frac{v_1}{u_1} = \frac{cos\theta \pm \sqrt{\frac{m_2}{m_1} + cos^2\theta - 1}}{(1 + \frac{m_2}{m_1})} \tag{61}$$

By multiplying this equation with m_1v_1/m_1u_1, the so called *kinematic factor* $k = E1/E0 = m_1v_1^2/m_1u_1^2$ is obtained

$$k = \frac{T_1}{T_0} = \frac{1}{\left(1 + \frac{m_2}{m_1}\right)^2}\left(cos\theta \pm \sqrt{\frac{m_2}{m_1} - sin^2\theta}\right)^2 \tag{62}$$

Here, m_2/m_1 is often represented by the variable A so that

$$k = \frac{T_1}{T_0} = \frac{1}{(1 + A)^2}\left(cos\theta \pm \sqrt{A - sin^2\theta}\right)^2 \tag{63}$$

Thus, if the initial energy of the incident particle T_0, the mass ratio of the interacting particles m_2/m_1 and the scattering angle θ are known, the energy of the scattered particle after the elastic collision will be

$$T_1 = T_0 \frac{1}{\left(1 + \frac{m_2}{m_1}\right)^2} \left(cos\theta \pm \sqrt{\frac{m_2}{m_1} - sin^2\theta} \right)^2 \tag{64}$$

This result will be used to calculate the energy of the scattered particle for different angles in the following section.

3.6 Stopping Power and SRIM Calculations

Stopping power is defined as the retarding force acting on charged particles that pass through matter. The range of energetic ions in all elements has been extensively documented [31]. For charged particles there are a variety of processes through which energy can be lost when passing through matter. In this section, such energy loss is calculated. Additionally, energy transferred during Rutherford scattering (as derived in section 3.5) is incorporated into this calculation. The principal processes involved for the particles and range of energies investigated in this chapter are: the ionization of atoms in the material and the inelastic interactions of the traversing ion with the electrons in the material.

The SRIM software package [32] enables the calculation of the stopping powers of various materials when bombarded with ions. Such programs have existed since at least the 1980s [23]. At the present it is accurate to about 96% [38] for high energy projectiles. As will be elaborated upon in section 5, a beam of ^{12}C ions at 59.7 MeV was made to impinge upon a 3.0 mg/cm^2 ^{194}Pt target. It is assumed throughout that the Rutherford scattering of the incident particles occurs only once - from the center of the target. It is also assumed that they deposit their energy in the center of each annular ring of the CD detector. An additional energy loss due to the 0.58 mg.cm^{-2} thick gold coating on the silicon CD detector is also calculated.

Using SRIM, energy loss due to the electronic stopping powers of the ^{194}Pt material was found to be -0.9583 MeV/(mg.cm^{-2}) for the 59.7 MeV ^{12}C beam. This energy loss of the moving particle is described by the Bethe formula [14]:

$$-\frac{dE}{dx} = \frac{4\pi n z^2}{m_e v^2} \cdot \left(\frac{e^2}{4\pi\epsilon_0}\right)^2 \cdot [ln(\frac{2m_e v^2}{I})] \tag{65}$$

The energy loss due to the stopping power of the target material is thus dependent on the traversing particle's energy. This is indicated in figure 20. Note that this is the non-relativistic form of the Bethe formula. Since the particle will lose more energy per unit distance traveled at lower energies, an iterative approach to calculating the energy loss will be more accurate than simply using the value of 0.9583 MeV/(mg.cm^{-2}) over the entire length of the target. The benefit of using such an iterative approach is mostly dependent on the thickness of the target.

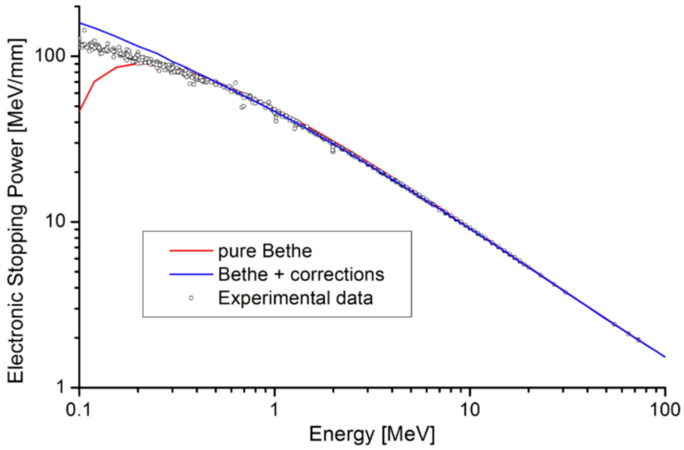

Figure 20: Electronic stopping powers as a function of incident particle energy [25]

Consider the scattering of a particle as shown in figure 21. The particle is assumed to scatter from the center of the target and will thus traverse a greater apparent thickness and hence lose more energy at larger scattering angles. This assumption is of course not true in general, since a beam particle may be scattered by any nucleus within the target material, but on average there is a greater probability of the scattering position being near the center of the target.

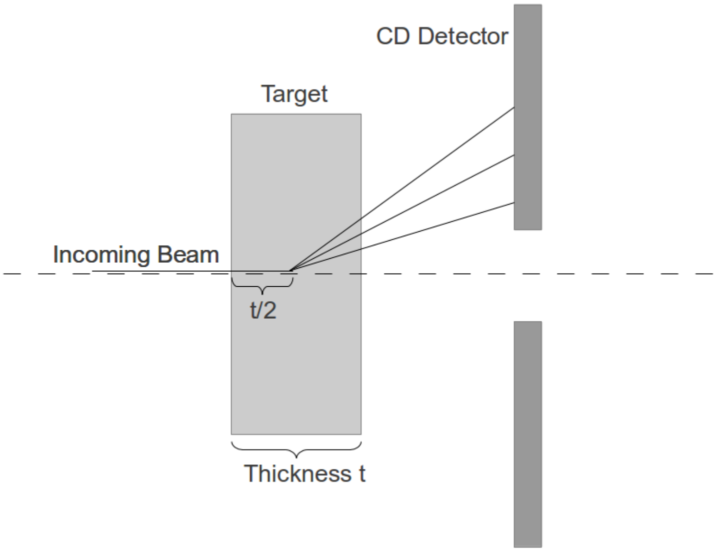

Figure 21: Illustration of the scattering of beam particles by the target.

In table 3 the elastic scattering angle, total distance traveled through the target and total energy loss of particles striking each of the 24 rings in the CD detector is presented.

Table 3: Energy loss of ^{12}C impinging on ^{194}Pt @ 59.7 MeV calculated with SRIM [32]. The angle corresponds to the scattering of a particle to the center of the appropriate ring. The apparent thickness, dx, is also shown.

Ring	Angle (Degrees)	dx (μm)	dE (MeV)
A	31.56	1.520	4.95 ±0.20
B	33.63	1.539	5.14 ±0.21
C	35.60	1.559	5.34 ±0.21
D	37.48	1.581	5.55 ±0.22
E	39.27	1.603	5.75 ±0.23
F	40.97	1.626	5.95 ±0.24
G	42.59	1.649	6.16 ±0.25
H	44.13	1.674	6.36 ±0.25
I	45.59	1.699	6.56 ±0.26
J	46.98	1.724	6.76 ±0.27
K	48.31	1.751	6.96 ±0.28
L	49.56	1.777	7.16 ±0.29
M	50.76	1.805	7.35 ±0.29
N	51.89	1.832	7.54 ±0.30
O	52.98	1.861	7.73 ±0.31
P	54.01	1.889	7.92 ±0.32
Q	54.99	1.918	8.10 ±0.32
R	55.92	1.947	8.29 ±0.33
S	56.82	1.977	8.47 ±0.34
T	57.67	2.007	8.64 ±0.35
U	58.48	2.037	8.82 ±0.35
V	59.26	2.068	8.99 ±0.36
W	60.01	2.098	9.16 ±0.37
X	60.72	2.129	9.33 ±0.37

Here follows a brief explanation of the calculations done to complete the aforementioned table. From the experimental details, the ^{194}Pt target is given the thickness of 3.0 mg/cm^2. Using the known density of platinum, 21.45 g/cm^3, along with this, the target is found to have a thickness of 1.4

μm. The distance between the target and detector, and the dimensions of the CD detector are used to find the scattering angle θ of a particle from the center of the target with thickness t:

$$\theta = tan^{-1}(x_v/19.4mm), \tag{66}$$

where 19.4 mm is the distance from the target to the CD detector, and x_v is the distance from the center of the CD detector to the center of the corresponding ring. This scattering angle θ enables the calculation of the actual distance the particle travels through the target. This total path length is visualized in figure 22 and calculated by using the equation

$$dx = t/2 + \frac{t/2}{cos(\theta)} \tag{67}$$

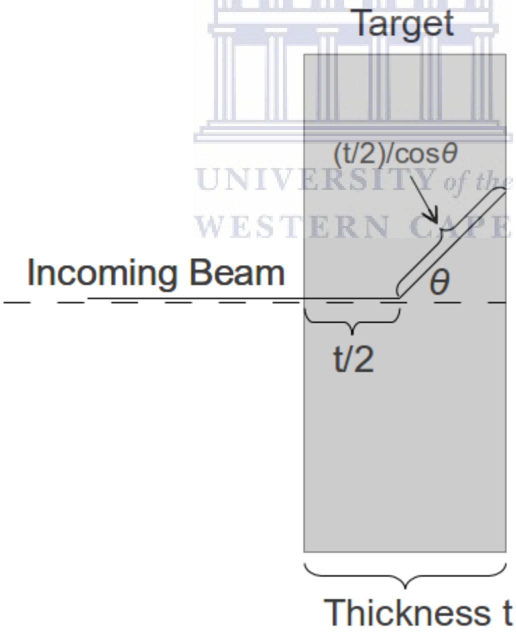

Figure 22: Distance traveled through the target by a scattered particle.

The total energy loss of the incident particle as it moves through the target is calculated in three steps: First the stopping powers obtained from SRIM are used to obtain the energy with which the projectile reaches the center of the target. Second, the energy lost by the projectile due to Rutherford scattering is calculated for all 24 angles using equation 64. SRIM is then used once again to calculate the stopping power for each of the 24 different energies after the elastic Rutherford collision. Lastly, 24 values are then multiplied with each of the 24 different path lengths and each of these is then added together with the energy loss obtained in the first step, along with the energy loss due to Rutherford scattering, to obtain the value of the total energy loss in the target for each of the 24 trajectories. The energy loss for each of the 24 scattering angles due to the gold coating on the silicon detector is then added to this value.

The values calculated with SRIM are not expected to be very accurate for several reasons. Firstly, as mentioned before, the energy lost by a particle in matter is inversely proportional to its kinetic energy. The value of dE/dx should therefore increase as the particle traverses the target material. For this reason the energy of the particle leaving the target calculated with SRIM will be higher than expected. This can be shown by a few calculations. The expected range of a 59.7 MeV ^{12}C ion in ^{194}Pt (as tabulated in SRIM) is 21.48 μm, but if we use the corresponding SRIM values of $dE/dx = 2.056$ MeV/μm with $dx = 21.48$ μm, then $dE/dx.dx = 44.16$ MeV. Since this value is less than 59.7 MeV, the ^{12}C ion would thus leave the 21.48 μm target with an energy of 15.54 MeV. The reason for this is due to the dependence of dE/dx on E, that is $\frac{dE}{dx}(E)$. Therefore, for better accuracy, values of dE/dx should be calculated for many different values of E.

Secondly; the centroid of the elastic peak energy distributions obtained for each of the rings in the experiment and simulation is the quantity of interest. Comparing the values obtained from SRIM (in table 3) with the values of these peaks is erroneous, because the centroid of a particular elastic peak is not expected to correspond to the energy of a particle scattered to the center of the corresponding ring in the detector. At smaller scattering angles the projectile will lose less energy due to smaller apparent thickness of the target. Energy transfer due to an elastic Rutherford scattering event is also less at smaller angles. Together with this, the distribution of scattered particles decreases (rapidly) with an increase in scattering angle, therefore the centroid of the elastic peak is expected to correspond to a particle scattered at angles smaller than the angle corresponding to the center of the ring. However, due to the small solid angle offered by each ring segment, the energies corresponding to the a particle trajectory to the center of each ring are not expected to be very different from the energies corresponding to the peak of each energy spectrum.

The SRIM package offers more sophisticated particle tracking techniques by so-called TRIM calculations. TRIM (Tracking the Range of Ions in Matter) offers the option of tracking individual ions through a material. A calculation of 59.7 MeV ^{12}C ions incident on ^{194}Pt is visualized in figure 23. Incorporating the results from such a TRIM calculation was not attempted due to the format of the output file and the long runtime of such a simulation. Nevertheless, TRIM offers a Monte Carlo simulation of the path of projectiles through matter and, due to the relative simplicity of performing such calculations, is thus a good candidate for simulating particle energy spectra. Such calculations should provide energy peaks with greater broadening at larger (differential) scattering angles and may therefore prove to be very useful.

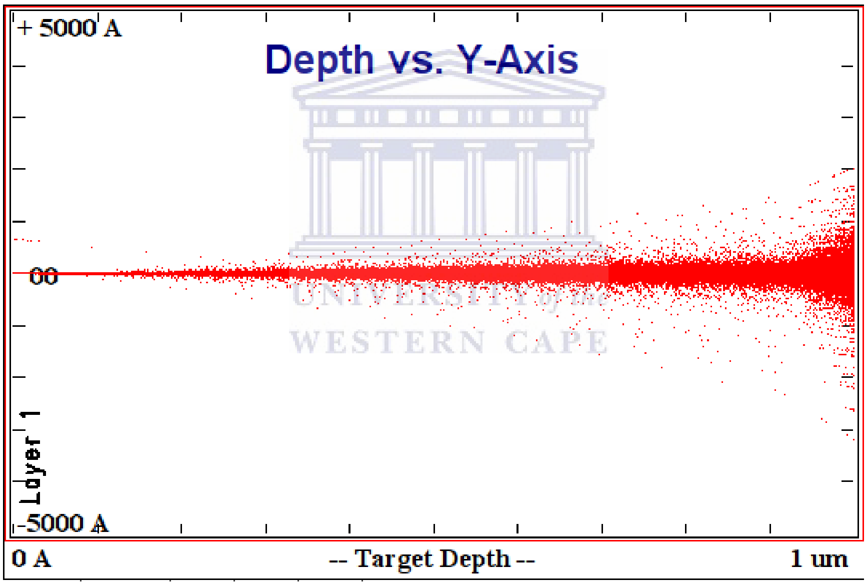

Figure 23: A TRIM plot of 59.7 MeV ^{12}C ions incident on ^{194}Pt.

4 GEANT4 Simulations

A simulation of the experiments carried out at TRIUMF was carried out using the GEANT4 package [12]. In this section, an introduction and overview of the GEANT4 toolkit is given, along with the aforementioned simulation. GEANT4 version 10 was used for this work. Doing the simulation described in this section is very problematic in older versions of GEANT4. This is briefly discussed in the introduction of appendix A.

4.1 Introduction to GEANT4

The GEANT4 project was started in 1994 in order to provide a flexible toolkit that could simulate the interaction of particles with matter. It is an object-oriented toolkit written in the C++ language [36] that provides a large degree of functionality for applications in fields such as particle physics, nuclear physics, accelerator design, space engineering and medical physics. A notable example of its use is at the Large Hadron Collider at CERN [39] where every LHC detector is modeled in GEANT4. GEANT4 works on the basis of an abundant set of physics models that are represented by large data libraries. These are implemented on the basis of Monte Carlo simulation methods and can handle the interactions between incident particles and matter for an energy range from about 250 eV to 1 TeV. GEANT4 thus acts as a repository which includes a large part of all that is known about particle interactions.

The following aspects of the simulation process are included in the GEANT4 toolkit:

1. The geometry of the system.
2. The relevant materials that form part of the geometry.
3. The fundamental particles of interest.
4. Time generation of the primary particles for events.
5. Tracking of the particles as they traverse through the materials and any externally applied fields.
6. The physics processes that govern particle interactions.
7. The response of sensitive detector components.
8. The generation of event data.
9. The storage of events and tracks.
10. The visualization of the detector and particle trajectories.
11. The capture and analysis of simulation data at different levels of detail and refinement.

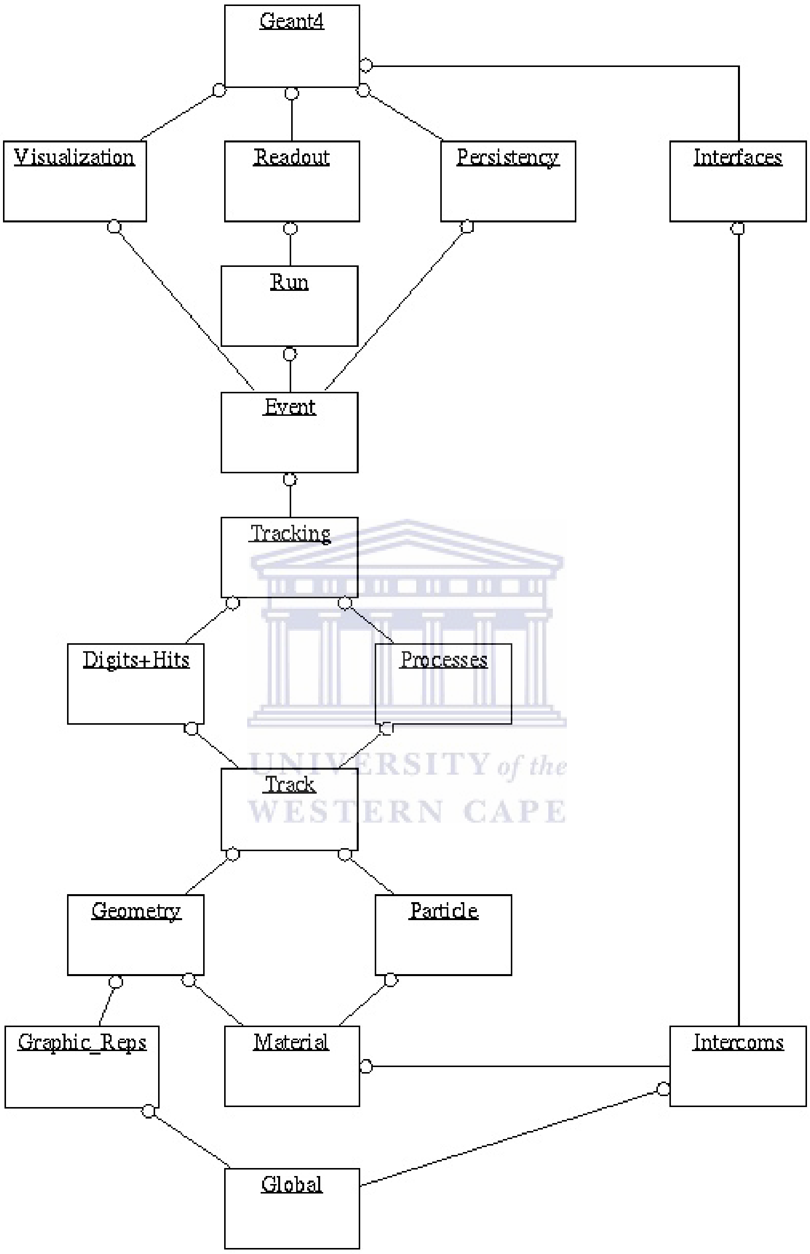

Figure 24: The class category diagram of GEANT4.

These aspects of the simulation are controlled by the 17 class categories that exist in GEANT4. The great benefit the object-oriented framework brings is that these 17 class categories can be developed and maintained independently, while the interface between each of these categories is maintained separately. The categories and their relationships are shown in figure 24. Each box represents a class category, and a straight line with an open circle represents a usage relationship. The category at the circle end uses the adjoining category. The GEANT4 source code is organized and built according to this structure.

The GEANT4 kernel handles run, event, track, step, trajectory and particle. A brief explanation of each of these functionalities follows:

Run is the largest unit of simulation in GEANT4. As an analogy with a real experiment, a run in GEANT4 starts with the command “BeamOn”. During a run the user cannot change the detector geometry and the settings of the various physics processes. Conceptually, run is thus a collection of events that share the same detector conditions. At the beginning of a run, the geometry is optimized for navigation and cross section data tables are calculated according to the materials that appear in the geometry.

Event is the main unit of simulation and represents the entire path of a generated particle from its inception by the particle gun through to its traversal of the created geometry and its subsequent interactions. The number of events is thus set before each run, because the user sets the amount of particles that are to be generated.

Track is a snapshot of the particle and is updated by each *step*. Track does not record all previous quantities, but only physical quantities of current instance. This is in order to preserve system memory.

A *step* in GEANT4 consists of two points of a particle’s path along with “delta” information from the track of the particle. This information includes the energy loss on the step, the time of flight during the step, etc.

Trajectory is the class which copies the desired information from the track (as mentioned above, track does not keep its trace).

A *particle* in GEANT4 is represented by three layers of classes, G4Track, G4DynamicParticle and G4ParticleDefinition. Once again, the position and other geometrical information is represented by G4Track. G4DynamicParticle contains the “dynamic” physical properties of a particle, such as momentum, energy and spin. G4ParticleDefinition contains the “static” properties of a particle such as mass, charge, life time, decay channels etc. Together, these represent a particle in GEANT4.

4.1.1 Building a Simulation in GEANT4

When building a simulation in GEANT4, most of the class interactions above are hidden from the user. The minimum input the user needs to give in order to build a simulation is the construction of the geometry of the detector system, the relevant physical processes and the setup of the simulation conditions. The flow process of a GEANT4 simulation is shown in figure 25. It can be seen here which actions are mandatory for the user to implement in his program.

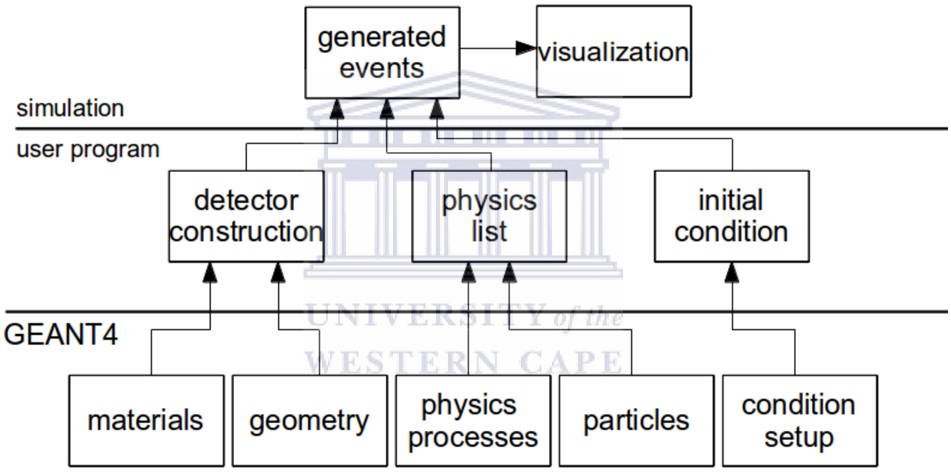

Figure 25: The flow process diagram of GEANT4.

From the diagram we can see the three categories of input that the user needs to provide the toolkit: the construction of the geometry and the relevant materials, the physics processes and particles that are applicable to the simulation and the initial conditions. Building a simulation usually involves editing one of the numerous example files that are provided along with the GEANT4 toolkit. A user will typically try to find an example that is as close to the desired simulation as possible and then proceed to edit the above three facets of the simulation as required.

4.1.2 A Simple Example of a GEANT4 Simulation

This section shows how a simple GEANT4 simulation of geantino[3] transportation is constructed according to the diagram in figure 25.

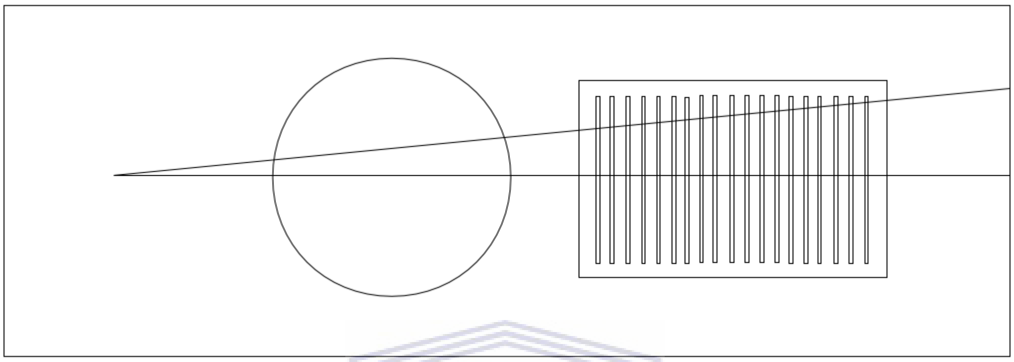

Figure 26: Visualization of geantino transport through a tracker tube and a calorimeter block in GEANT4.

Detector Construction
The geometry of the detector is defined in the source file for detector construction. This simple example uses a tracker tube made of aluminium to measure the coordinates of the incoming beam particles, and a calorimeter block made of lead is used to measure their energy. The classes G4Tub and G4Box are used to design the desired detector elements with their respective dimensions.

Physics List
The only particle involved in the simulation is the geantino; therefore only the geantino needs be defined in the physics list source, and the only physical process is transportation.

Initial Conditions
The initial conditions only consist of the amount of geantinos that are to be fired by the particle gun, their energy and direction. Many more commands are available, but this is the minimum required to get the simulation to work. After building the simulation according to the above, it can now be run in

---

[3] Geantinos are virtual particles used in GEANT4 to illustrate the transportation process of particles only. They do not interact with matter, and there is thus no energy loss due to any type of interactions. Geantinos behave much like neutrinos, hence the similarity in the given name for these created, virtual particles.

order to get the results. They are displayed in table 4. This simulation output shows the desired information of a single geantino at each step along its path. It can be seen how the kinetic energy of the geantino remains unchanged, while the x- and z-coordinates change as it traverses the geometry. It is often useful to know in which volume a particle is and which process was responsible for the change between steps, hence the displaying of these in the table.

Table 4: Results of simulation of geantino transport in GEANT4.

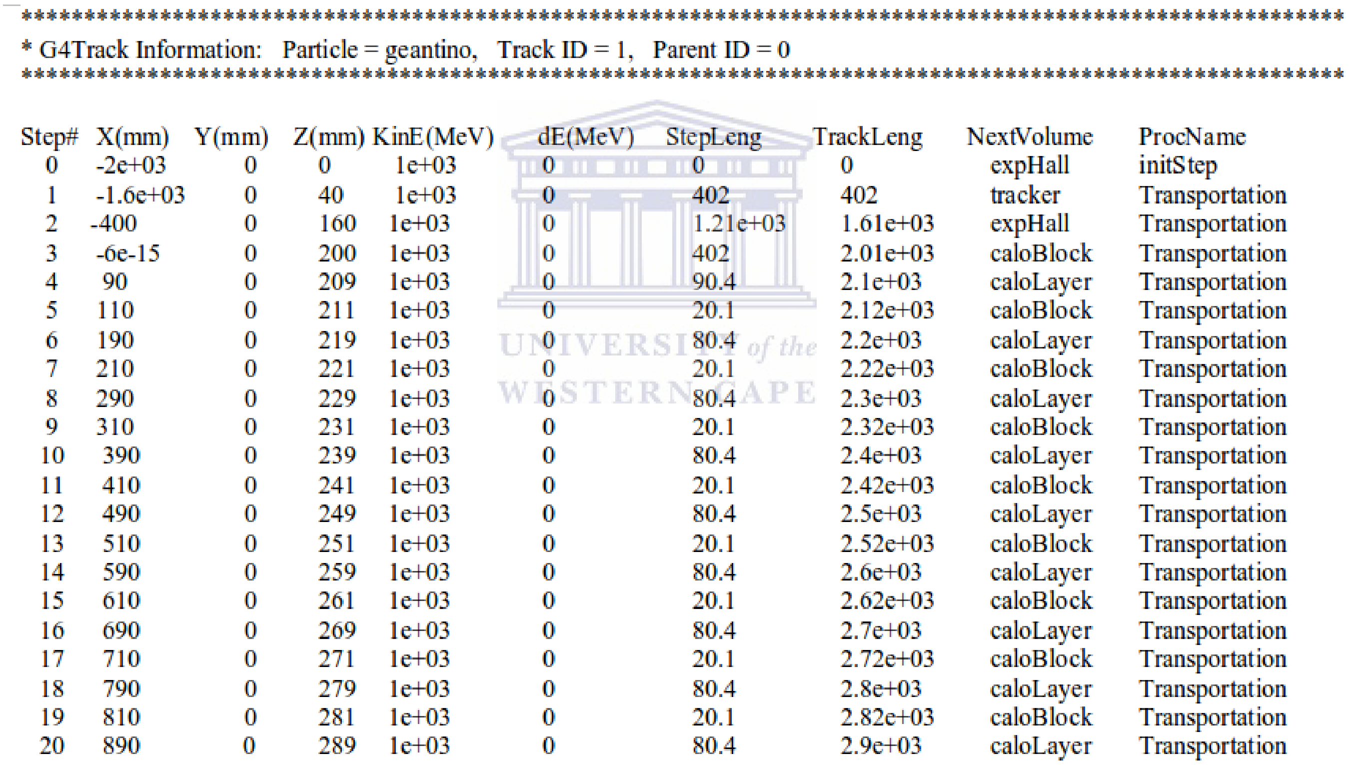

```
*****************************************************************************************
* G4Track Information:   Particle = geantino,   Track ID = 1,   Parent ID = 0
*****************************************************************************************

Step#  X(mm)     Y(mm)  Z(mm) KinE(MeV)  dE(MeV)  StepLeng   TrackLeng  NextVolume  ProcName
  0    -2e+03      0      0     1e+03      0       0          0          expHall    initStep
  1    -1.6e+03    0     40     1e+03      0       402        402        tracker    Transportation
  2    -400        0    160     1e+03      0       1.21e+03   1.61e+03   expHall    Transportation
  3    -6e-15      0    200     1e+03      0       402        2.01e+03   caloBlock  Transportation
  4     90         0    209     1e+03      0       90.4       2.1e+03    caloLayer  Transportation
  5    110         0    211     1e+03      0       20.1       2.12e+03   caloBlock  Transportation
  6    190         0    219     1e+03      0       80.4       2.2e+03    caloLayer  Transportation
  7    210         0    221     1e+03      0       20.1       2.22e+03   caloBlock  Transportation
  8    290         0    229     1e+03      0       80.4       2.3e+03    caloLayer  Transportation
  9    310         0    231     1e+03      0       20.1       2.32e+03   caloBlock  Transportation
 10    390         0    239     1e+03      0       80.4       2.4e+03    caloLayer  Transportation
 11    410         0    241     1e+03      0       20.1       2.42e+03   caloBlock  Transportation
 12    490         0    249     1e+03      0       80.4       2.5e+03    caloLayer  Transportation
 13    510         0    251     1e+03      0       20.1       2.52e+03   caloBlock  Transportation
 14    590         0    259     1e+03      0       80.4       2.6e+03    caloLayer  Transportation
 15    610         0    261     1e+03      0       20.1       2.62e+03   caloBlock  Transportation
 16    690         0    269     1e+03      0       80.4       2.7e+03    caloLayer  Transportation
 17    710         0    271     1e+03      0       20.1       2.72e+03   caloBlock  Transportation
 18    790         0    279     1e+03      0       80.4       2.8e+03    caloLayer  Transportation
 19    810         0    281     1e+03      0       20.1       2.82e+03   caloBlock  Transportation
 20    890         0    289     1e+03      0       80.4       2.9e+03    caloLayer  Transportation
```

4.2 GEANT4 Simulations of the Silicon CD Detector

It has been shown that GEANT4 is a suitable framework for simulating the cross sections due to Rutherford Scattering[4] [13] and energy loss due to the stopping power of the material [22]. One of the main objectives of this thesis is to simulate a silicon detector system that serves as an end detector for a beam that has been scattered by the nuclei in a target. This section discusses the details of the implementation of the experimental parameters in GEANT4, and the results of these simulations. The experimental parameters are discussed in section 5 and are thus only mentioned here.

4.2.1 Geometry of the Silicon CD Detector

The geometry of the CD detector was implemented in GEANT4 according to the details given in section 3.2.1. The detector is visualized in figure 27. Note that the sectors that are visible are artifacts of the visualization technique used and thus do not correspond to the 32 physical sectors of the detector.

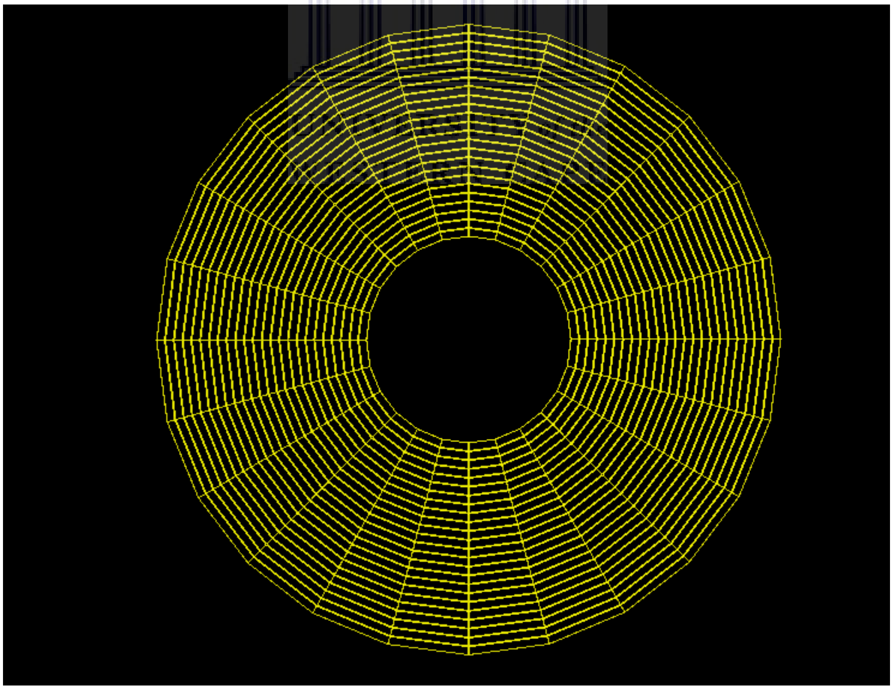

Figure 27: A Silicon S3 detector visualized in GEANT4.

---

[4] It is worth noting that α-particles were used for these simulations. More importantly, only the scattering cross sections were measured - the stopping power of the material was irrelevant to this study.

Each of the silicon ring and sector components are created using the *G4Tubs* class, and these separate parts are then placed next to each other to create the detector as seen in the figures. In order for these silicon components to be sensitive, i.e. to be able to obtain physical values from their interaction with particles, the built in GEANT4 class *G4SDManager* is used. Furthermore, a user created class, *RootAnalysis* is implemented to output the data from each ring and sector into a ROOT file [27].

4.2.2 Other Experimental Parameters

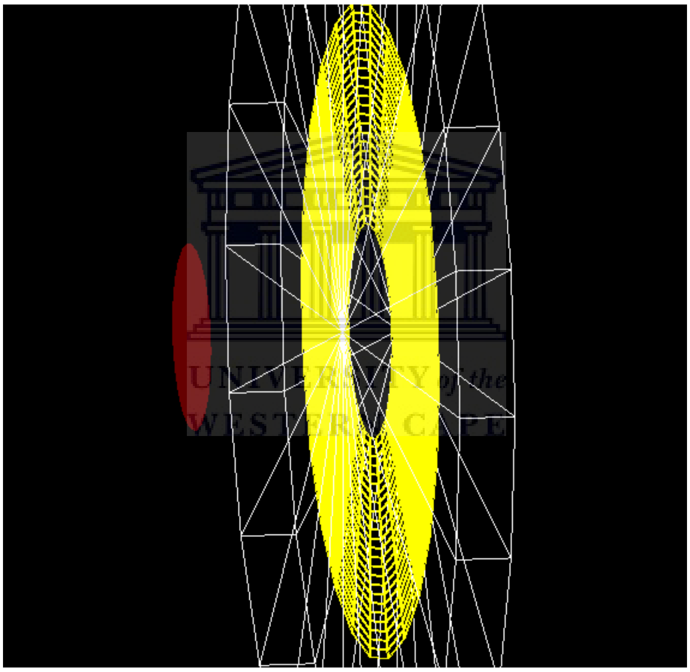

Figure 28: A ^{194}Pt target and silicon S3 detector visualized in GEANT4. The dimensions of the target have been greatly increased for visualization purposes. The white volume around the yellow CD detector is the logical volume.

Enriched (96.5%) ^{194}Pt serves as the target, and this was implemented in the *Detector Construction* class as is described in appendix A. The target was placed 1.94 cm in front of the CD detector. For simulating CVD diamond, the detector material was simply replaced with carbon at a density of 3.515 g/cm^3. Figure 28 shows a visualization of the target next to the CD detector. The logical volume can also be seen in figure 28 - this volume is necessary for data collection.

The particle gun that produces the ^{12}C beam is constructed in the *Primary Generator* class to produce ^{12}C ions at 59.7 MeV and their direction is set to be along the axis adjoining the target and the detector. Additionally, one can set a statistical energy and direction deviation. The beam profile can also be set to any shape. These details may be useful in simulations that require very high precision and where the beam characteristics are known very well. For this simulation all the beam particles are simply being generated out of the same point. 20 Billion particles were produced by the *Primary Generator* to simulate the experiment. A visualization of the complete simulation with fifty thousand incident particles is shown in figure 29

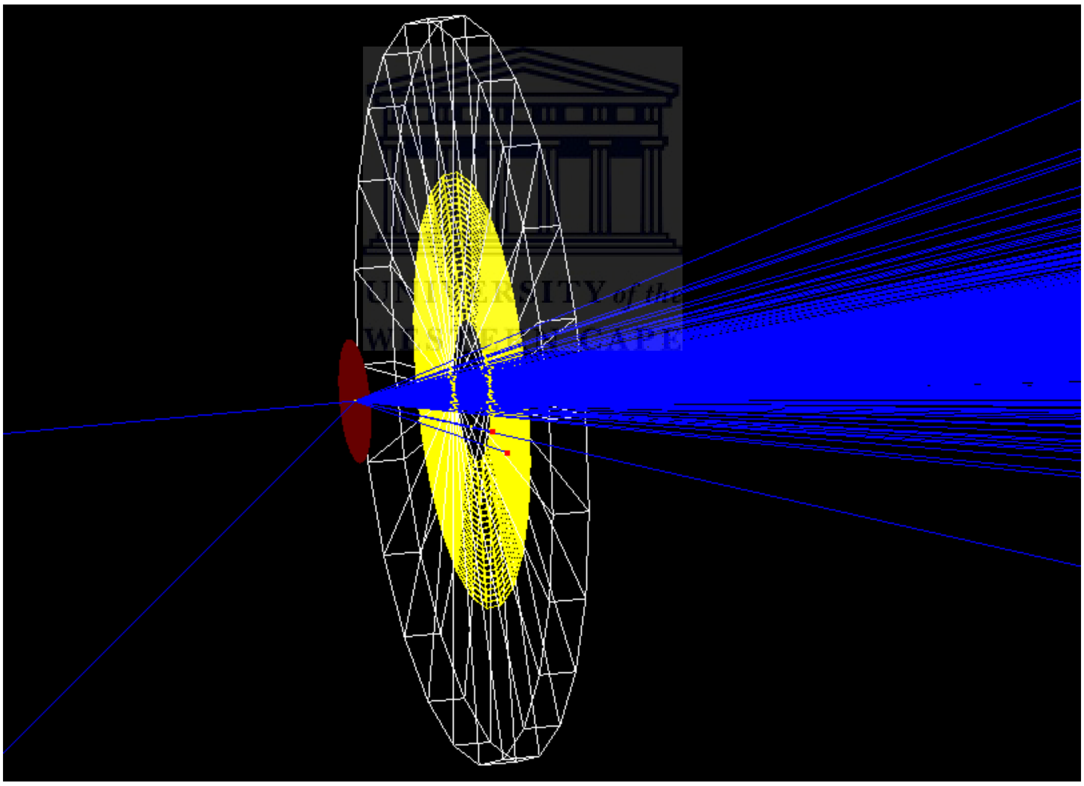

Figure 29: A visualization of the complete simulation in GEANT4. Most of the particles go through the hole in the center of the CD detector. One particle can be seen to have backscattered. The red dots represent particles striking the detector.

4.2.3 Results of GEANT4 Simulations for the Silicon S3 CD Detector

The energy spectra obtained from the GEANT4 simulations for the silicon detector are presented in this section.

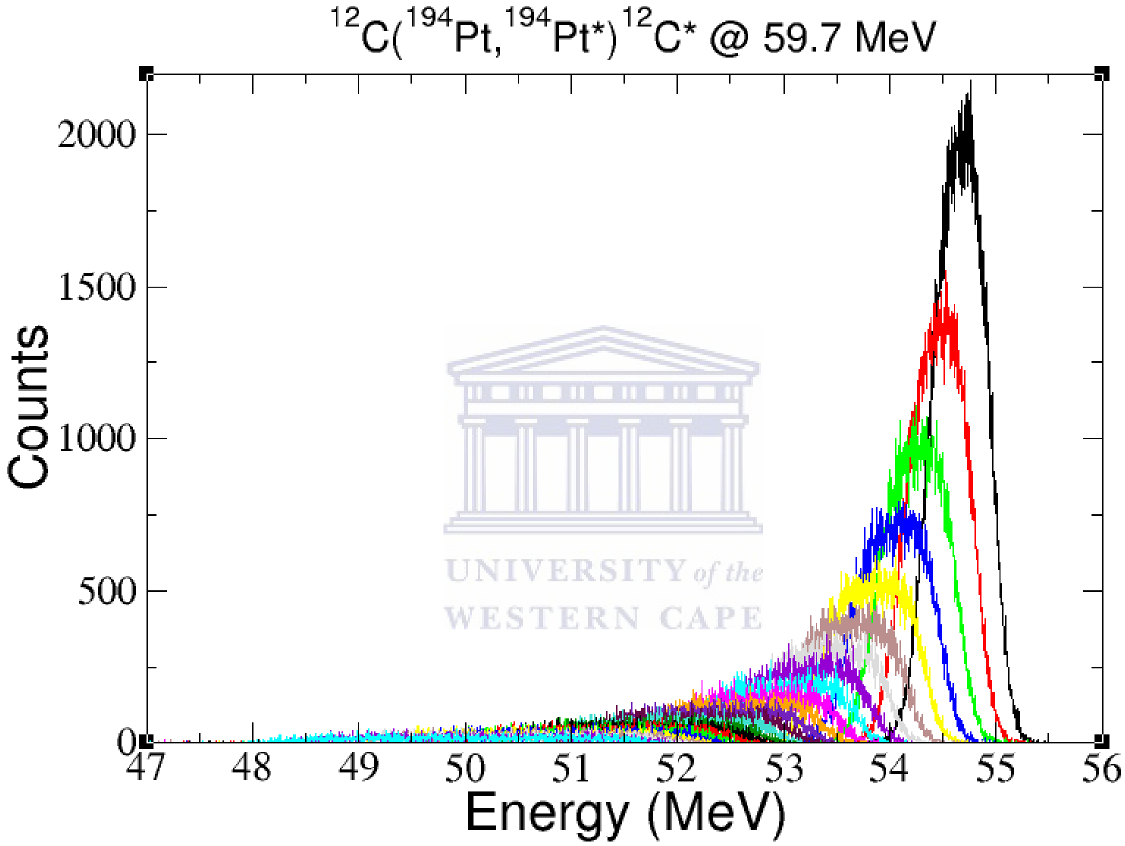

Figure 30: Results of GEANT4 simulations of rings A to X of a silicon CD detector.

The simulation output of all the rings is shown in figure 30. Since the purpose of the simulation is to only simulate the elastic peak, it has to be verified that no inelastic peak is present in the data. This was done by counting the number of γ-rays that are created in the target. The γ-ray spectrum was indeed found to be empty. This result was expected. GEANT4 is capable producing γ-rays due to nuclear de-excitation [30], but nuclear Coulomb excitation is not possible. To simulate Coulomb excitation of nuclei, the GOSIA simulation [29] package is required.

The spectra obtained from the sectors were all nearly identical. This is to be expected since all the relevant physical processes are symmetric about the incident beam direction. A plot of 4 of the sectors in figure 31 shows this. The data for the rings were fitted in ROOT using the MINUIT [28] fitting program. The application of such a fit along with the associated goodness-of-fit values are shown in figure 32. The fitting is discussed in section 6.

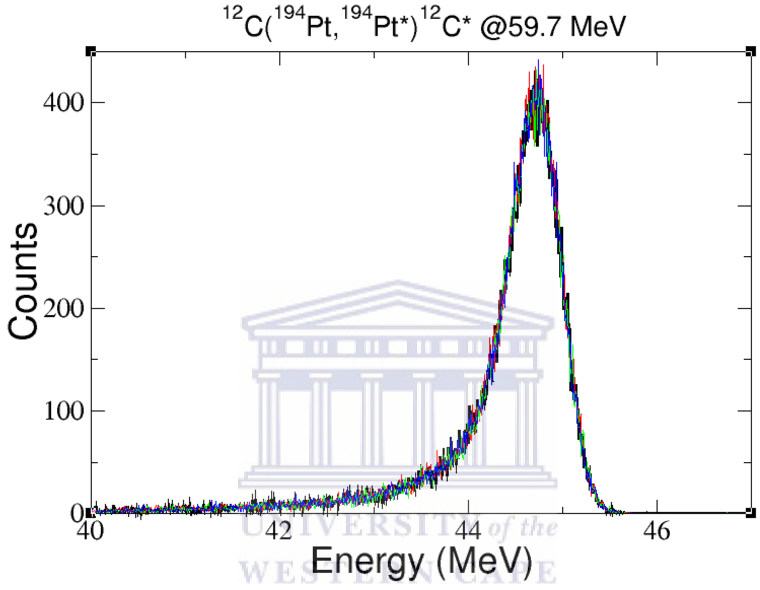

Figure 31: The spectra of 4 sectors of a silicon S3 CD detector simulated in GEANT4.

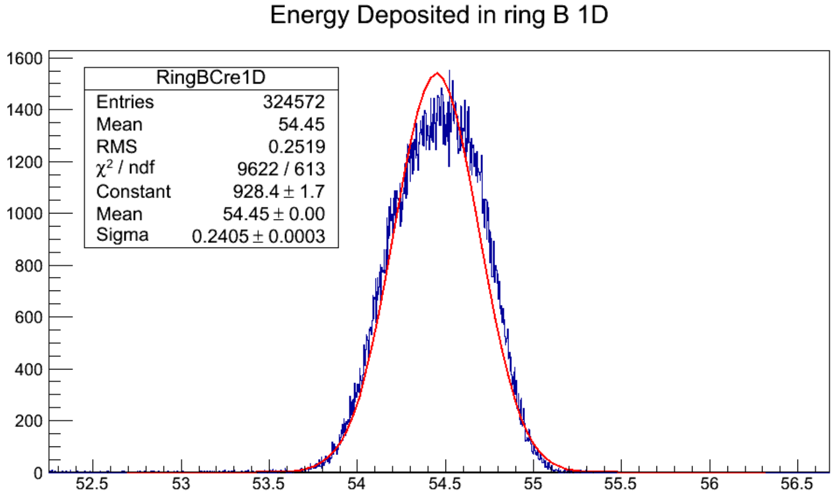

Figure 32: Fitting of ring B in ROOT using MINUIT.

The raw data from the simulation of the silicon CD detector is shown in figure 33. The values extracted from these data are discussed in section 6.

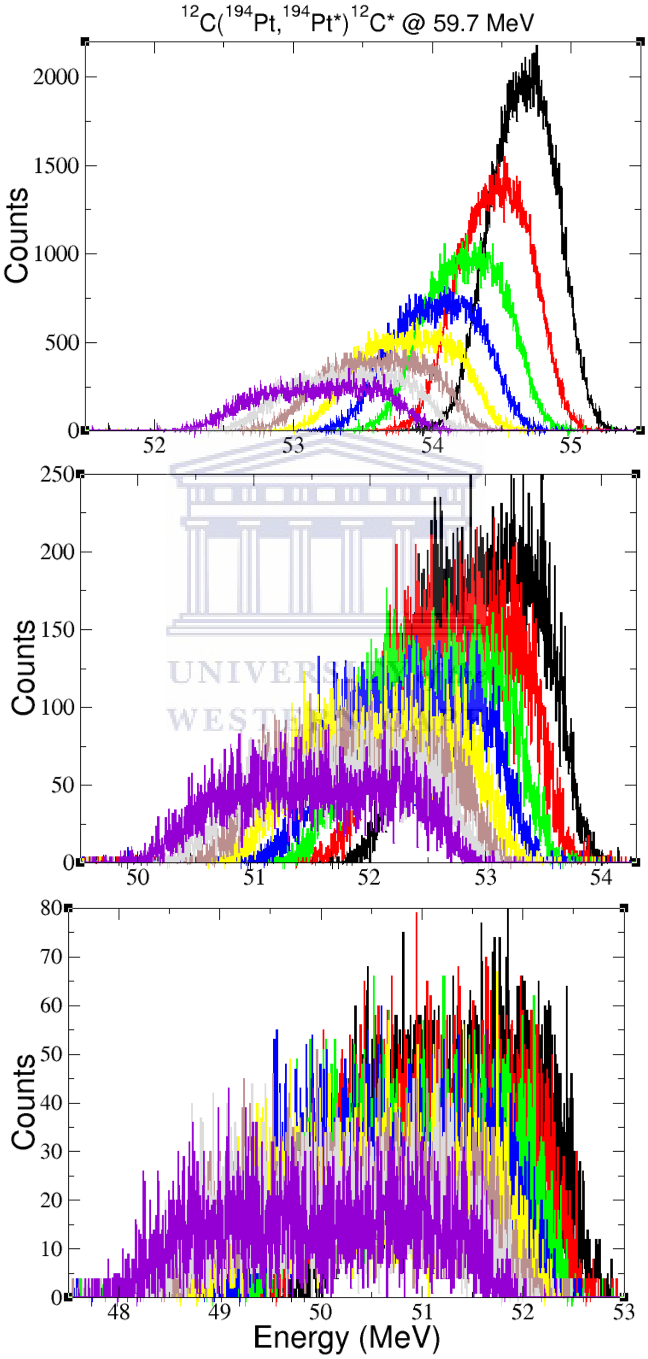

Figure 33: Results of GEANT4 simulation of the silicon S3 CD detector for rings A to H (top panel), I to P (middle panel) and Q to X (bottom panel).

The fitted functions of the simulations for the silicon CD detector are shown in figure 34. The validity of the fits are discussed in section 6.

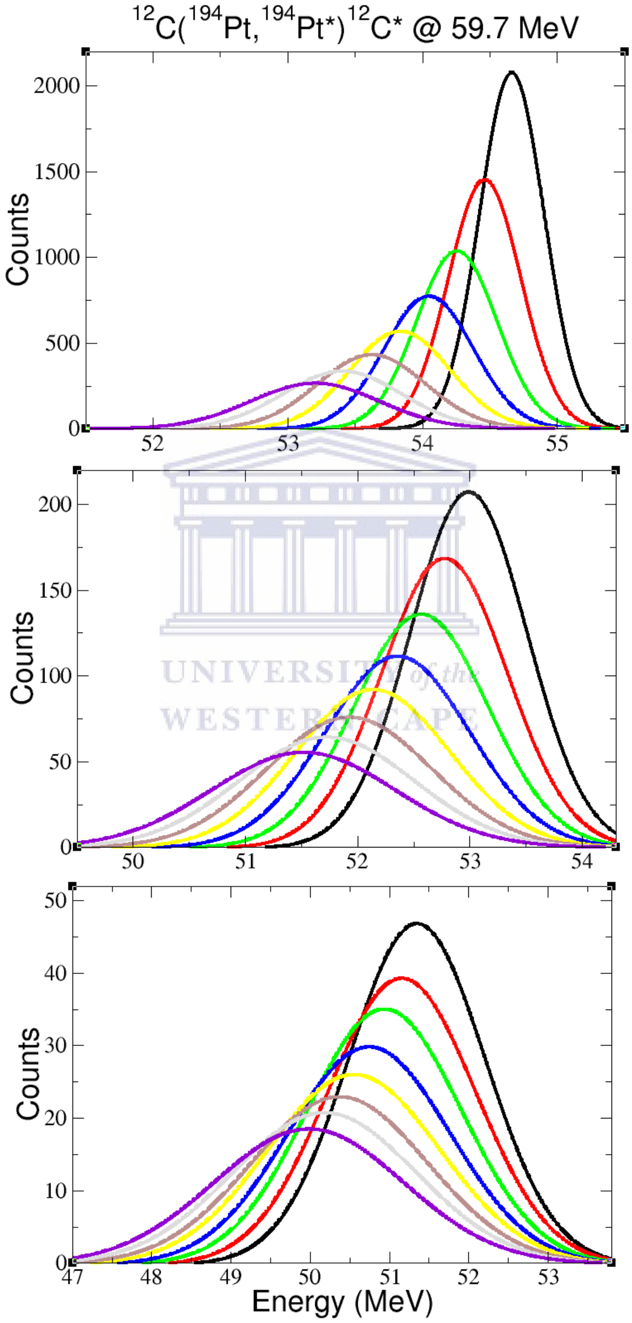

Figure 34: Fitted functions of spectra of GEANT4 simulation results for rings A to H (top panel), I to P (middle panel) and Q to X (bottom panel).

4.2.4 Results of GEANT4 Simulations for the Diamond Detector

The output of the simulations for the diamond CD detector is presented in this section. Near identical results are obtained here to what was found for the silicon CD detector. A smaller run was performed for the diamond due to time constraints. The outermost rings therefore don't have very good data. The fits that were performed still gave results exactly like one would expect for the silicon, so a longer data run wasn't necessary. In figure 35 the raw simulation data from the simulation of the diamond detectors is shown.

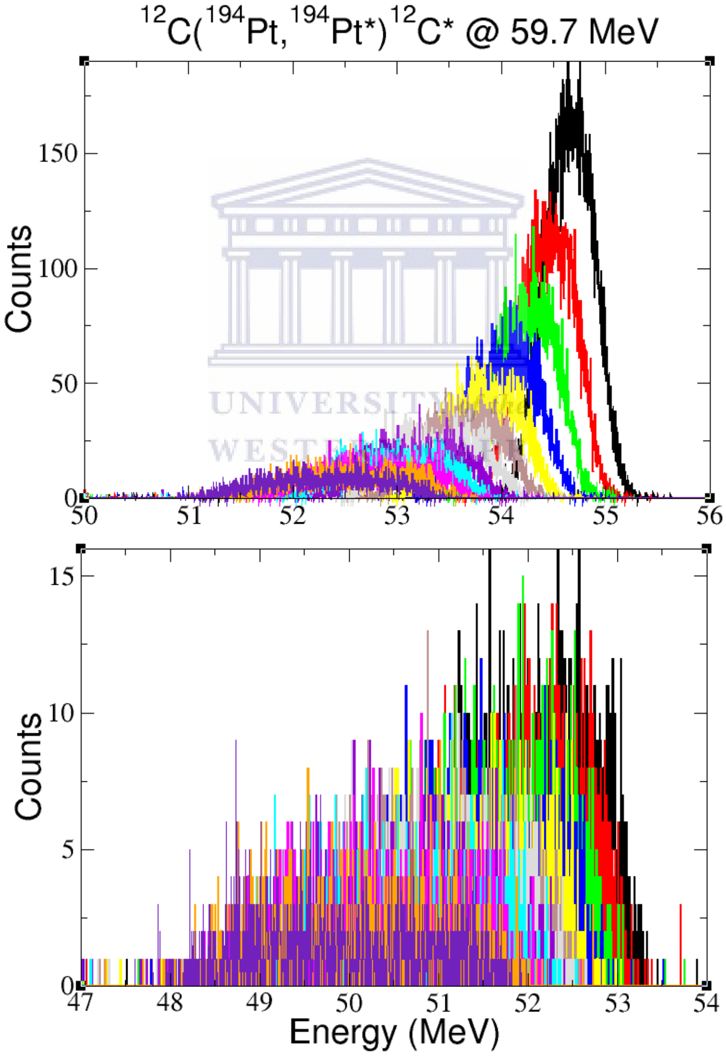

Figure 35: Results of GEANT4 simulation of the diamond S3 CD detector for rings A to L (top panel) and M to X (bottom panel).

The fitted functions of the simulations for the diamond CD detector are shown in figure 36. The comparison of these results with those from the simulation of the silicon S3 CD detector and the subsequent discussion appears in section 6.

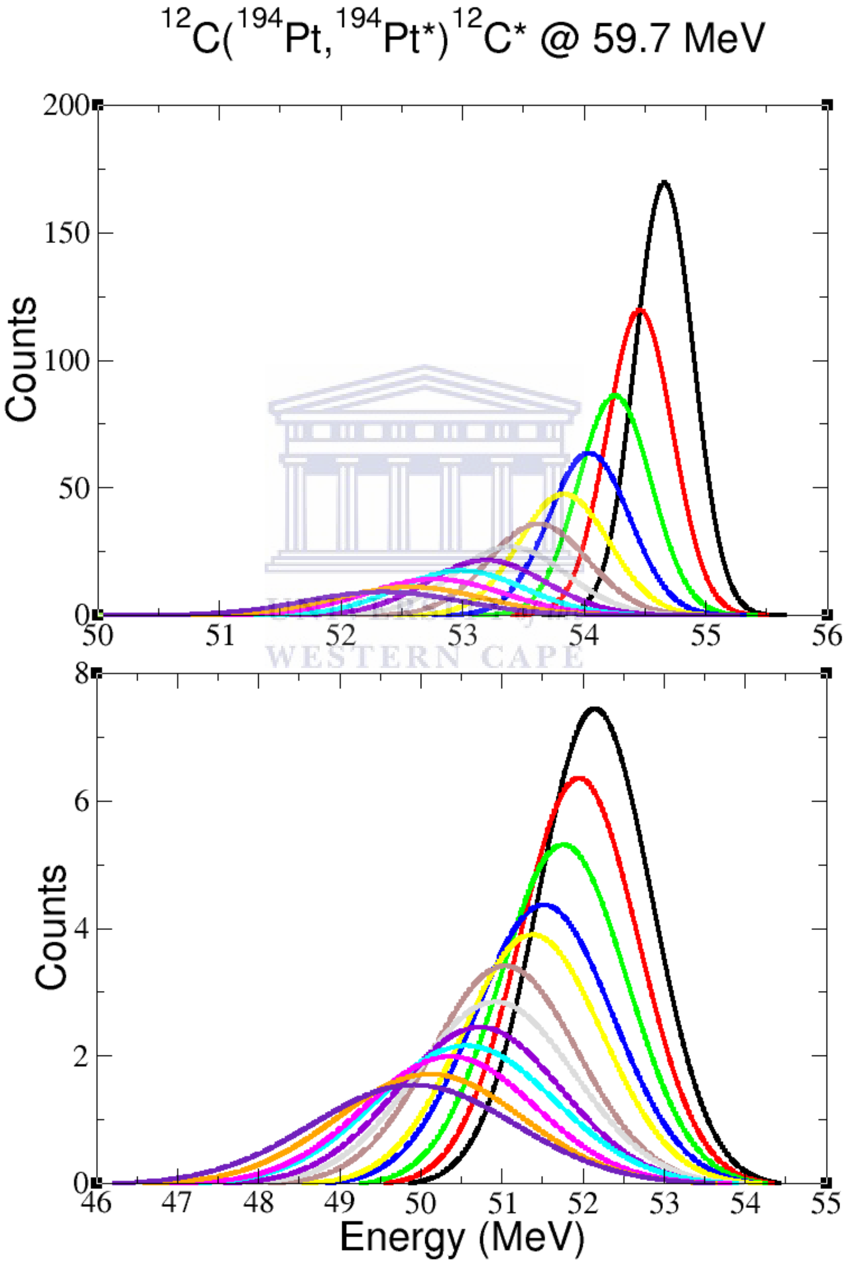

Figure 36: Fitted functions of spectra of GEANT4 simulation results for diamond rings A to M (top panel) and L to X (bottom panel).

5 Experimental Tests

A Coulomb-excitation study using a ^{12}C beam has been carried out using the TRIUMF/ISAC-II ion-beam facility. The ^{12}C beam was produced at an energy of 59.7 MeV over a period of 4 days, and made to impinge upon a 3.0 mg/cm^2 ^{194}Pt (96.5% enriched) target.

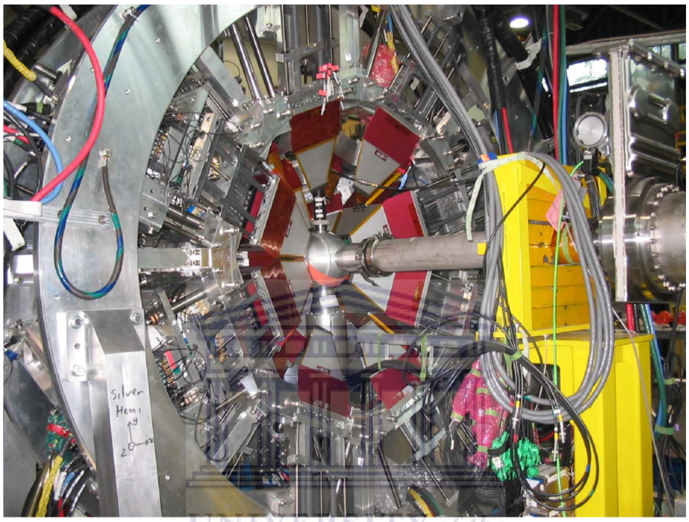

Figure 37: The TIGRESS HPGe γ-ray array at the TRIUMF facility.

Gamma rays emitted following the de-excitation of states in the target nuclei were detected by eight highly efficient and segmented, Compton suppressed TIGRESS clover detectors positioned 152 mm from the target and covering approximately 15% of 4π. The TIGRESS detectors subtended (θ, ϕ) laboratory angles, in a right-handed coordinate system with the z axis downstream of the beam direction, of (90°, 22.5°), (90°, 292.5°), (90°, 22.5°), (90°, 337.5°), (135°, 22.5°), (135°, 22.5°), (135°, 22.5°) and (135°, 292.5°). Each clover comprises 32-fold segmented HPGe crystals coupled with 12-fold segmented Compton suppression shields. Scattered ions were detected using an annular, double sided S3 silicon CD detector comprised of 32 sectors and 24 rings. This was mounted downstream at 1.94 cm from the target, aligned perpendicular to the beam axis and subtending laboratory θ angles between 30.6° and 61.0°. The scattered beam was fully stopped in the 140 μm thick silicon detector. A trigger rate of $\approx$2000 s^{-1} has been monitored for this experiment.

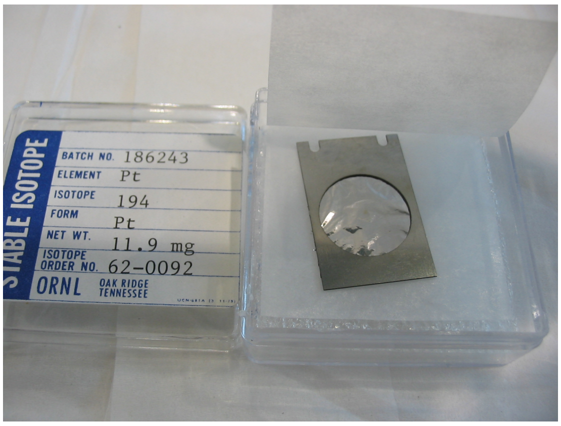

Figure 38: Photo of the ^{194}Pt target before the experiment.

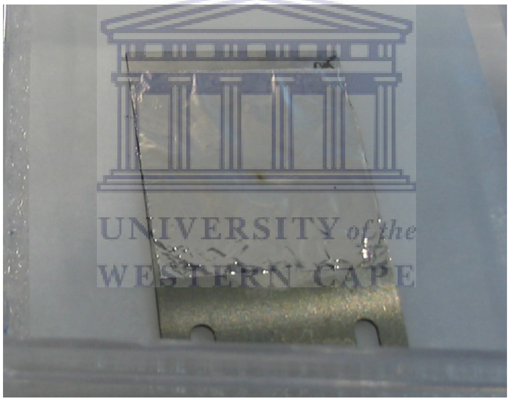

Figure 39: Photo of the ^{194}Pt target after the experiment. A small black dot can be seen in the center of the target due to irradiation effects during the experiment.

Since the purpose of this work is to simulate the particle energy spectra obtained from the silicon S3 CD detector, only these data are included. The γ-ray spectra obtained from the TIGRESS detectors will be presented in future work. The energy deposited in each of the 24 rings by the scattered beam is shown in figure 40. It can be seen how the energy peak shifts to lower energies as one moves to the outer rings. There is also a distinct broadening effect that increases with an increase in scattering angle. A few energy spectra from the sectors have been included simply to illustrate that they differ considerably. These are shown in figure 41. The reason for this is that these data have not been calibrated as yet. In theory, as with the simulated results, the spectra data should be near identical. A comparison of these data with the GEANT4 simulation data is presented in the section 6.

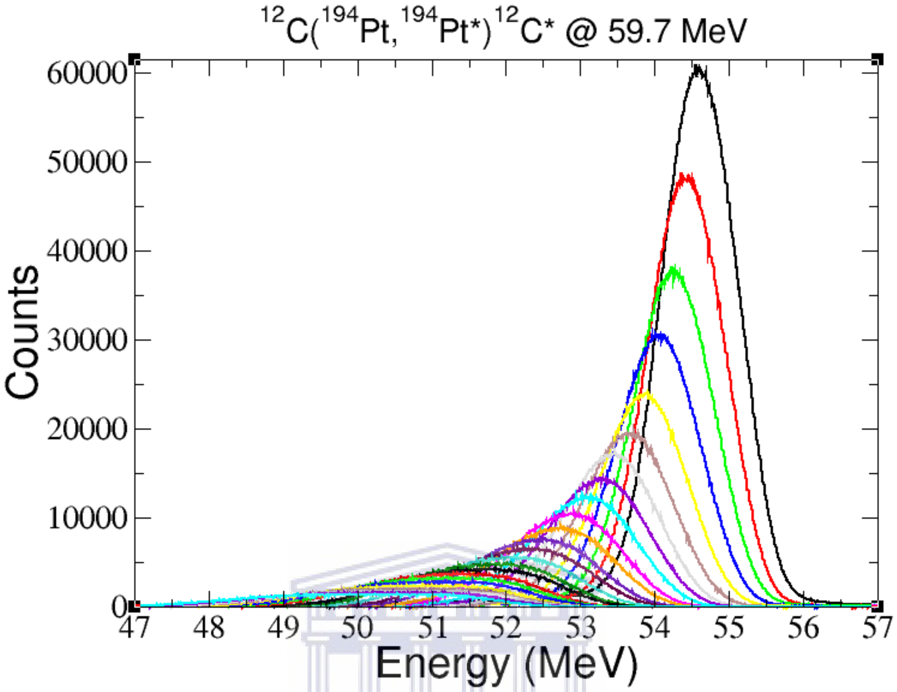

Figure 40: Results of experimental tests for rings A to X of the silicon S3 CD detector.

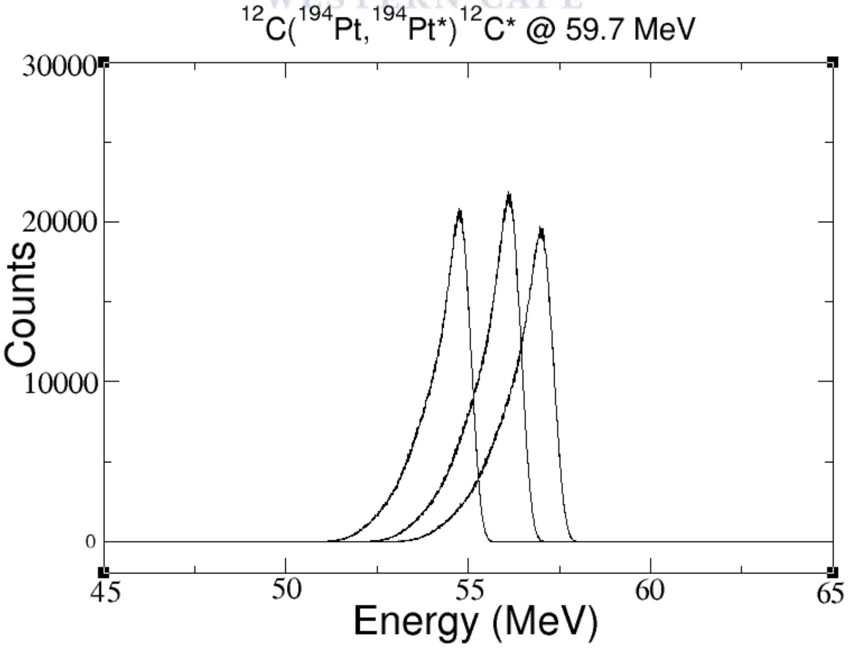

Figure 41: Results of experimental tests for 3 of the sectors of a silicon S3 CD detector. No calibration has been performed for these data.

Figure 42 shows the energy spectra for various rings in the CD detector.

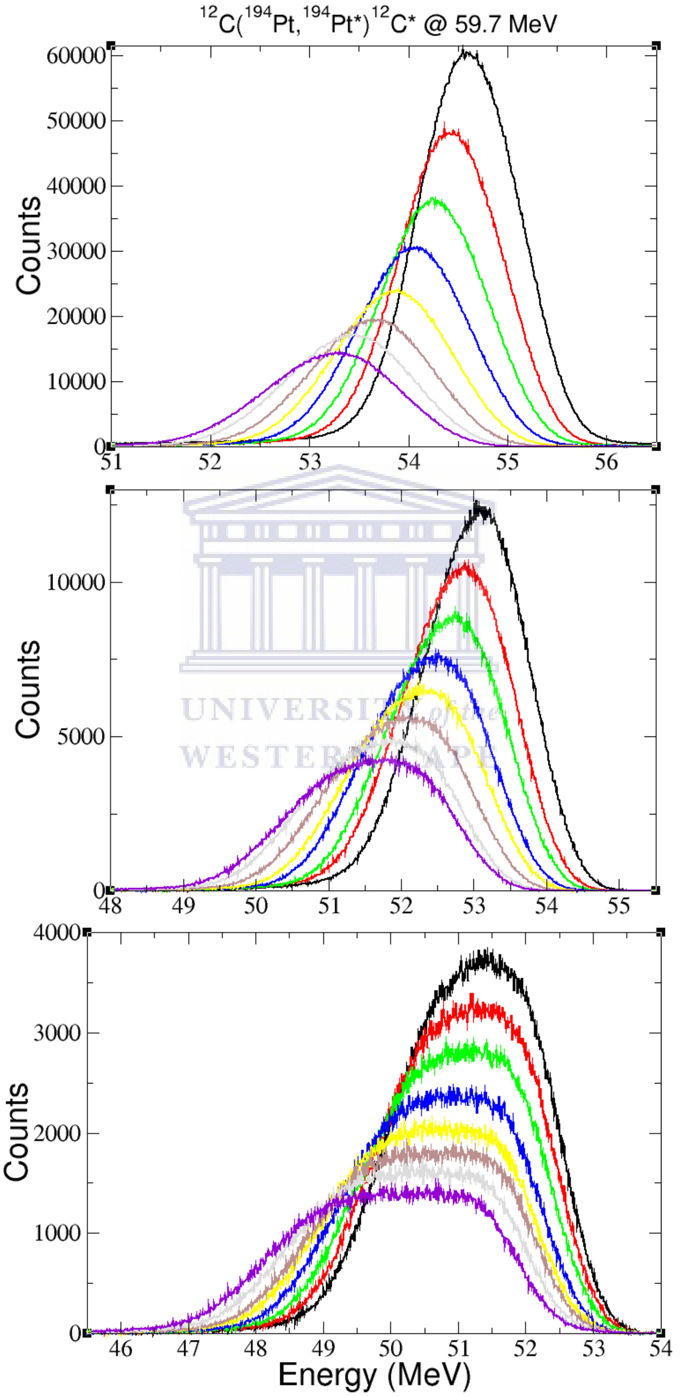

Figure 42: Results of experimental tests for rings A to H (top panel), I to P (middle panel) and Q to X (bottom panel) of the silicon S3 CD detector.

As with the results of the GEANT4 simulation, the energy spectra obtained from the experiment have been fitted in ROOT using MINUIT. For visual comparison, the fits of rings A to F are plotted along with the experimental data in figure 43. The fitted functions are shown in figures 44 & 45.

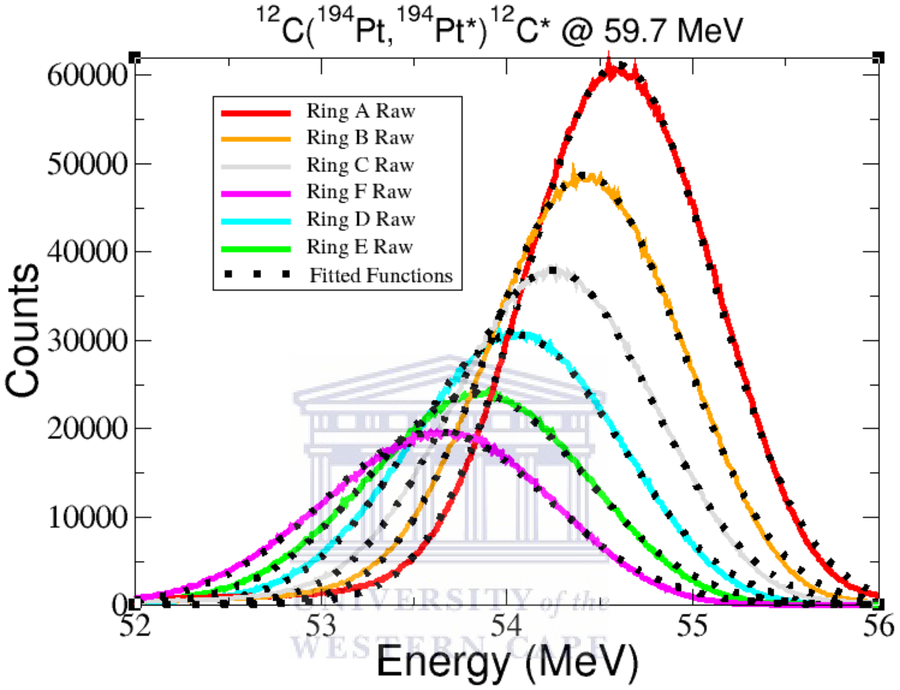

Figure 43: Results of experimental tests for rings A to F of a silicon S3 CD detector, along with their fitted functions.

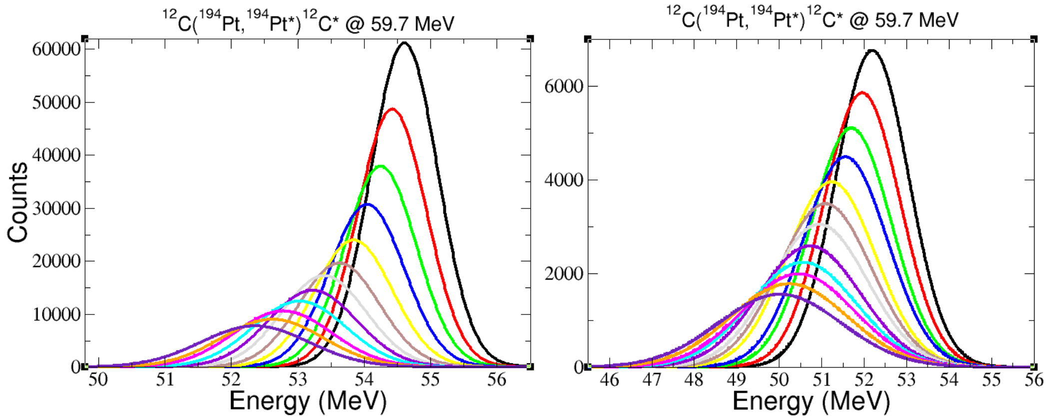

Figure 44 & 45: Fitted functions of experimental energy spectra for the silicon CD detector corresponding to rings A to M (left) and L to X (right).

6 Discussion of Results

In order to compare the results of the GEANT4 simulations with experiment, functions had to be fitted to the data. The method for doing so has been mentioned - using the MINUIT package in ROOT. All the data were fitted with Gaussian functions, but, as can be seen in figures 46 & 47, the choice of function is questionable. The χ^2 goodness-of-fit[5] test indicates that the fits are poor. A different goodness-of-fit test, the so called R^2 coefficient of determination[6] yields better results. For the experimental results the value of R^2 was greater than 0.98 for all the rings, while for the simulation R^2 varies from 0.99 for ring A to 0.86 for ring X. For the purposes of a meaningful comparison, the fitted functions are accepted as representative of the data.

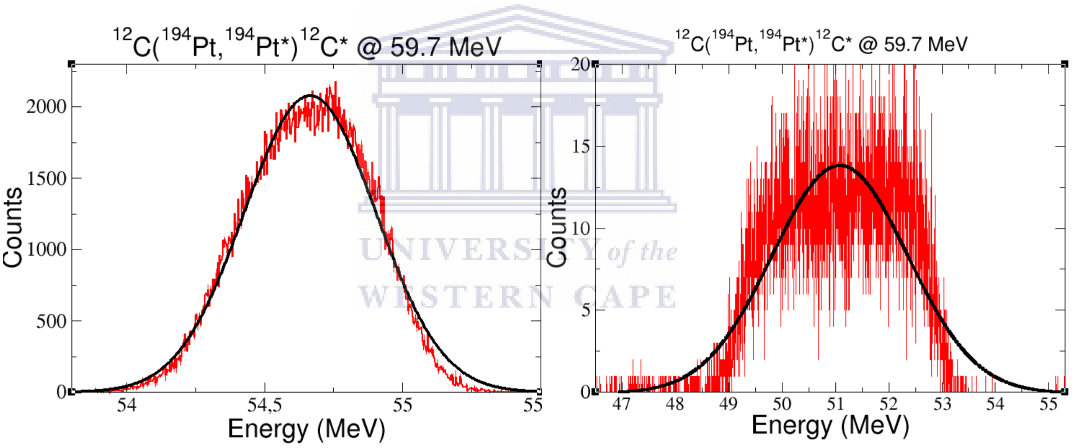

Figure 46 & 47: Fitted functions and raw data of the GEANT4 simulations of ring A (left) and X (right) shown to illustrate the goodness-of-fit.

Parameters extracted from the fits can thus be compared. The centroid, width and relative size of the particle energy spectra are the quantities of interest.

In table 5 the centroids of the energy peaks of the experiment and simulations are compared. The results for the silicon and diamond detectors were nearly identical. At larger scattering angles the difference is expected to in-

---

[5] Pearson's χ^2 test is defined as $\chi^2 = \sum_{i=1}^{n} \{(O_i - E_i)^2/\sigma^2\}$ where O_i and E_i are the observed and expected values in bin i and σ the variance.

[6] The R^2 test is defined as $R^2 = 1 - SS_{res}/SS_{tot}$ where SS_{res} is the residual sum of squares and SS_{tot} is the total sum of squares.

Table 5: Energy of the centroid of fitted functions for the experimental results and the GEANT4 simulations of silicon and diamond, along with the energy of a particle scattered to the center of the applicable ring calculated with SRIM, for ^{12}C incident on ^{194}Pt @ 59.7 MeV.

Ring	Experimental (MeV)	Silicon (MeV)	Diamond (MeV)	SRIM (MeV)
A	54.60	54.65	54.66	54.75 ±0.20
B	54.42	54.45	54.46	54.56 ±0.21
C	54.25	54.24	54.25	54.36 ±0.21
D	54.04	54.03	54.04	54.15 ±0.22
E	53.84	53.81	53.85	53.95 ±0.23
F	53.62	53.60	53.63	53.75 ±0.24
G	53.40	53.38	53.39	53.54 ±0.25
H	53.22	53.17	53.20	53.34 ±0.25
I	53.02	52.97	52.99	53.14 ±0.26
J	52.78	52.74	52.77	52.94 ±0.27
K	52.62	52.53	52.57	52.74 ±0.28
L	52.35	52.34	52.35	52.54 ±0.29
M	52.19	52.10	52.15	52.35 ±0.29
N	51.96	51.89	51.95	52.16 ±0.30
O	51.70	51.71	51.76	51.97 ±0.31
P	51.56	51.51	51.52	51.78 ±0.32
Q	51.23	51.35	51.38	51.60 ±0.32
R	51.09	51.11	51.04	51.41 ±0.33
S	50.94	50.88	50.92	51.23 ±0.34
T	50.73	50.78	50.73	51.06 ±0.35
U	50.56	50.53	50.56	50.88 ±0.35
V	50.45	50.35	50.37	50.71 ±0.36
W	50.23	50.15	50.12	50.54 ±0.37
X	50.02	50.01	49.92	50.37 ±0.37

crease due to the low counts in the outer rings. Considering that one of the goals at the outset of this work was to test the viability of a diamond detector system, these results seem positive. The results should not be interpreted in this way however. The simulations that were built for this project were rather primitive; that is, they do not represent the full-scale testing of detector systems that is required in order to fully validate the production of such devices. GEANT4 simulates the interaction of particles with matter and hence any type of analysis of a detector system that includes the electronics of such a system cannot be tested directly. The simulation itself simply measures the loss of energy of the scattered particles, hence any material would suffice as a detector material as long as it completely stops the impinging particle. Semiconductor material properties that are so vital to a detector system are also not taken into consideration since the basic definition of materials in GEANT4 only includes parameters such as atomic mass and density of the desired materials. More sophisticated methods for testing detector systems have been done to great effect [21], but such simulations are beyond the scope of this work. The results provided herein do however represent a first step in simulating diamond detectors thoroughly through GEANT4 simulations. Subsequent discussions will omit results from the simulation of the diamond detector due to its results being, in effect, the same as that for silicon.

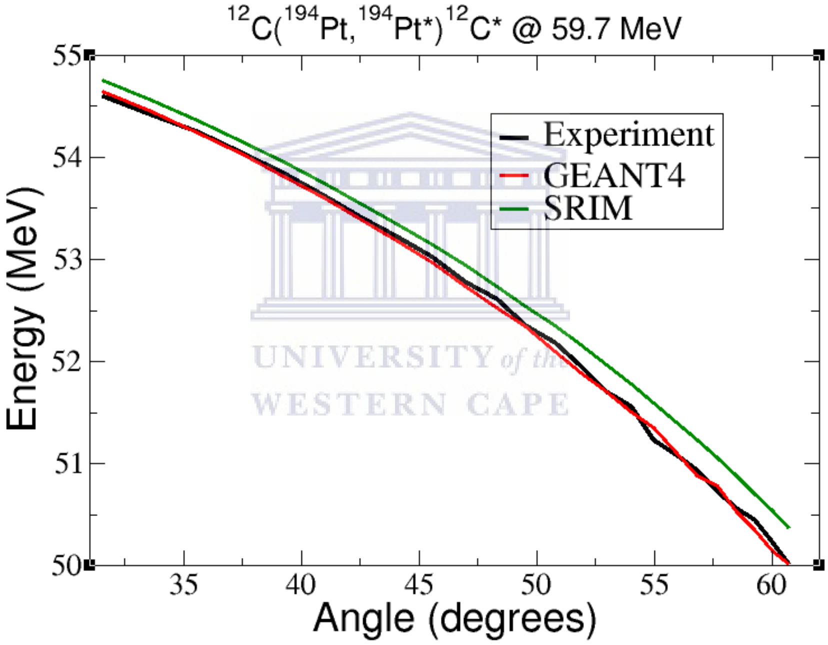

Figure 48: Centroid energy vs scattering angle θ comparison of Experimental results, GEANT4 simulations and SRIM calculations.

Figure 48 is constructed from the values in table 5. The values of the centroids of the energy peaks obtained by GEANT4 are in excellent agreement with the experimental results. As discussed in section 3.6, the SRIM calculations are not expected to be very accurate. It was not the goal of this work to obtain accurate values for the energy centroids using SRIM. It was mainly used as a general measure of accuracy during the building of the GEANT4 simulation. For this reason, only 2 iterations were used as the ^{12}C ion traversed the ^{194}. An accurate simulation of the *shapes* of the peaks is of value in this work, therefore a framework that offers sophisticated Monte Carlo simulations, such as GEANT4, is necessary.

As discussed in section 4.2, GEANT4 has been proven to simulate the cross section well for Rutherford scattering. However, the concurrent simulation of Rutherford scattering with energy loss due to stopping powers has not. In figure 49 the differential cross section is represented as a scattered fraction - i.e. the number of particles scattered into each ring segment as a percentage of the total number of incident particles. GEANT4 is found to follow the theoretical prediction of the Rutherford scattering cross section very accurately.

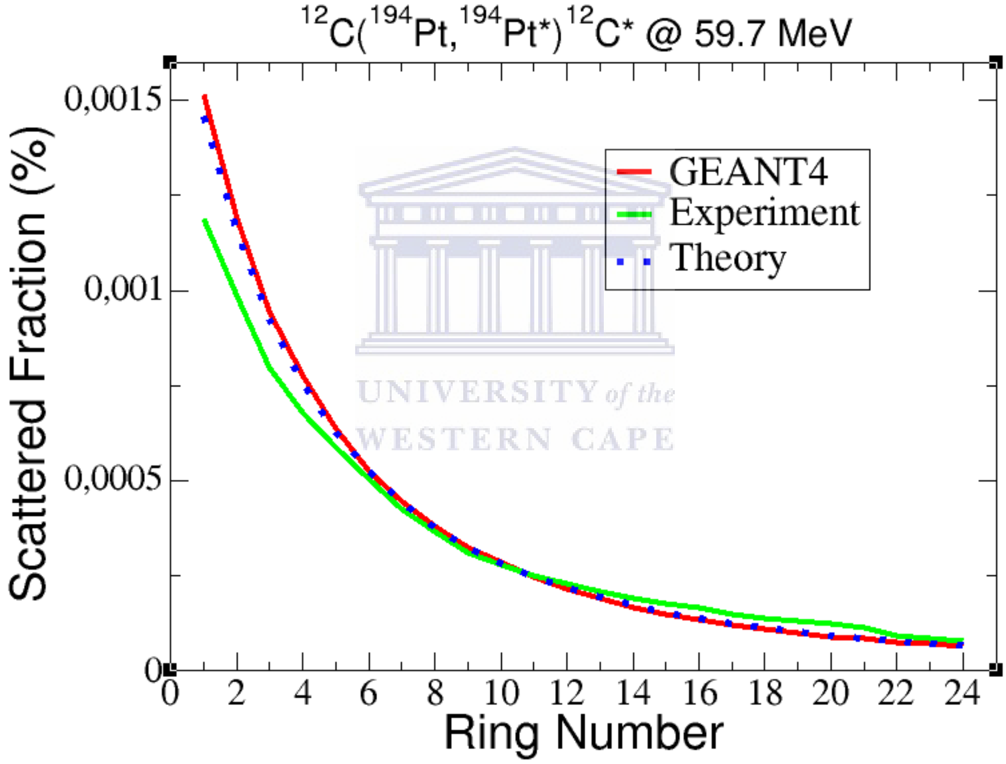

Figure 49: A comparison of the percentage of particles scattered into each ring, numbered 1 to 24, for the experimental results, GEANT4 and values obtained through calculations of the differential cross section with the appropriate conditions.

The deviation of the experimental results from this curve can be attributed to various factors. It is expected that the inner rings will be more damaged due to irradiation than those at larger scattering angles. This is a possible explanation for the deviation of the inner rings from the curves representing the GEANT4 and theoretical cross sections. For the outer rings, the electronic mechanisms and dead layers affect the data more due to the increase in angle and consequently larger solid angle presented by these detector features.

Background noise and the resolution of the detector will also influence the total number of counts obtained. Additionally, the exact number of particles produced for the experiment is difficult to ascertain, so the normalization of this curve is not very accurate. Nevertheless, the counts of each ring element relative to the others will not change. The scattered fraction of particles into each ring element is shown in table 6. The experimental values are omitted from the table due to the uncertainty of the total number of incident particles in the experiment.

Table 6: Comparison of theoretical and GEANT4 differential cross sections by comparing percentage of particles scattered into each detector element.

Ring	Theoretical (%)	GEANT4 (%)
A	1.46×10^{-3}	1.52×10^{-3}
B	1.15×10^{-3}	1.19×10^{-3}
C	9.25×10^{-4}	9.45×10^{-4}
D	7.55×10^{-4}	7.78×10^{-4}
E	6.25×10^{-4}	6.38×10^{-4}
F	5.23×10^{-4}	5.24×10^{-4}
G	4.42×10^{-4}	4.48×10^{-4}
H	3.78×10^{-4}	3.81×10^{-4}
I	3.26×10^{-4}	3.25×10^{-4}
J	2.83×10^{-4}	2.85×10^{-4}
K	2.47×10^{-4}	2.45×10^{-4}
L	2.18×10^{-4}	2.16×10^{-4}
M	1.93×10^{-4}	1.90×10^{-4}
N	1.72×10^{-4}	1.67×10^{-4}
O	1.53×10^{-4}	1.50×10^{-4}
P	1.38×10^{-4}	1.36×10^{-4}
Q	1.25×10^{-4}	1.22×10^{-4}
R	1.13×10^{-4}	1.10×10^{-4}
S	1.03×10^{-4}	1.01×10^{-4}
T	9.36×10^{-5}	9.06×10^{-5}
U	8.58×10^{-5}	8.38×10^{-5}
V	7.88×10^{-5}	7.66×10^{-5}
W	7.26×10^{-5}	7.14×10^{-5}
X	6.71×10^{-5}	6.61×10^{-5}

The broadening of the energy peaks due to an increase in target thickness is characterized by the FWHM of the function fit to the data. A comparison of the FWHM of the results from the GEANT4 simulation and the experimental tests is presented in table 7. The spectra obtained from experiment have a larger FWHM than any of their corresponding values obtained with GEANT4. For the inner rings, the difference in FWHM is larger between the two sets of data than for the outer rings. The energy lost due to the stopping power of the target is directly related to the broadening of the energy peaks. The greater the stopping power of the material, or the target thickness, the more broadening will be observed.

Table 7: Comparison of the FWHM of the energy peaks obtained from the GEANT4 simulations and the experimental tests.

Ring	Experimental (MeV)	GEANT4 (MeV)
A	1.19	0.58
B	1.22	0.65
C	1.27	0.74
D	1.32	0.83
E	1.38	0.92
F	1.43	1.02
G	1.49	1.11
H	1.57	1.21
I	1.66	1.32
J	1.74	1.43
K	1.82	1.55
L	1.91	1.65
M	2.01	1.78
N	2.11	1.88
O	2.22	2.01
P	2.34	2.08
Q	2.46	2.20
R	2.57	2.35
S	2.69	2.44
T	2.82	2.56
U	2.98	2.67
V	3.10	2.78
W	3.24	2.89
X	3.41	2.99

The simulated spectra are expected to differ substantially from the experimental spectra in terms of the broadening of the peaks. The silicon S3 CD detector, as with any detector system, has an inherent resolution. The current created due to the creation of electron-hole pairs in the semiconductor material is not in one-to-one agreement with the energy deposited by the particle that is stopped in the detector volume. As mentioned before, a semiconductor is damaged by irradiation during particle detection experiments - this will also affect its efficiency and contribute to the broadening of the obtained energy peaks. Other factors like background noise also influence the spectra. Another possible reason for the greater broadening of the peaks observed in the experimental data is a variation in beam direction during the experiment. For these reasons the experimental peaks were expected to have greater broadening than those from the GEANT4 simulation. The simulated peaks may be artificially broadened to correspond to the experimental peaks. A method for doing this will be discussed briefly in section 7.

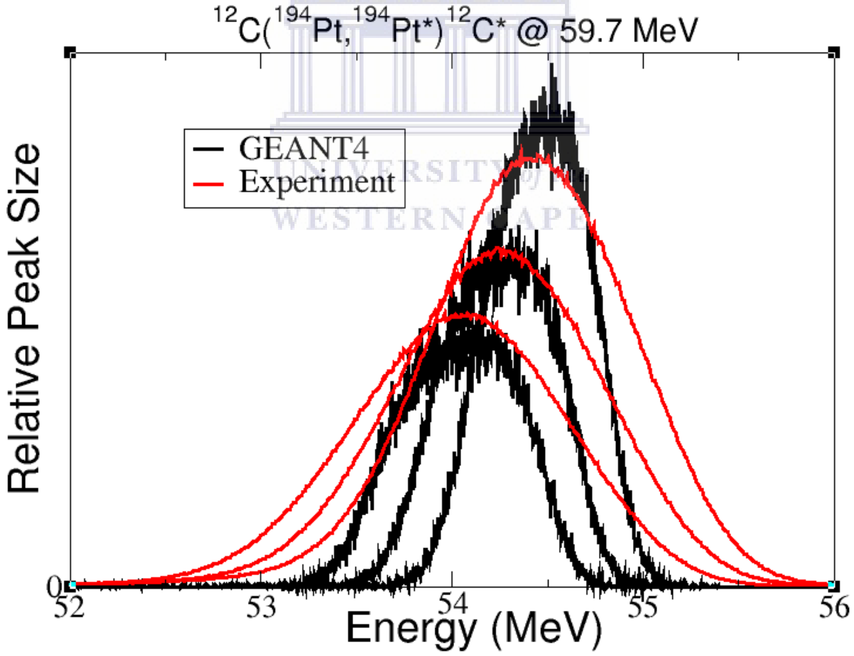

Figure 50: Comparison of raw experimental and GEANT4 data of rings B, C and D.

In figure 50 the shapes of spectra for 3 of the rings obtained by experiment and GEANT4 simulations are compared. The GEANT4 spectra had to be vertically scaled for this comparison. It is clear that these spectra differ considerably due to the increased broadening of the experimental peaks.

7 Conclusions and Future Work

GEANT4 simulations of ^{12}C ions scattered through a ^{194}Pt target at energies below the Coulomb barrier produce results in excellent agreement with the theoretical and experimental values. The values of the energy centroids as compared in table 5 show close correlation between the experimental and simulated values for each of the rings. Similarly, the comparison of the Rutherford cross sections in figure 49 shows that GEANT4 follows the theoretical cross sections throughout the angular range of the CD detector.

The accuracy of GEANT4 in simulating the energy loss in matter of a ^{12}C ion has been previously studied in human tissue [26], but not in the heavier targets simulated in this work. In addition to this energy loss, the concurrent simulation of Rutherford scattering to obtain particle energy spectra at different scattering angles has not been performed before. GEANT4 is used in a variety of fields, as mentioned in section 4.1, but the most active areas of research are high energy particle physics, space physics and medical physics. The results of this simulation validate the use of GEANT4 for simulating particle energy detectors at energies below the Coulomb barrier. Due to the close correlation between the GEANT4 results and the theoretical predictions, the conclusion is made that the differences between the experimental and GEANT4 cross sections are strictly due to factors related to the detector instrument, and not to fundamental physical principles.

During the course of this work, it has become apparent that certain aspects of the simulation and subsequent analysis can be improved. A variation in beam direction, however small, will broaden the simulated peaks. This can be implemented in GEANT4. Very precise beam diagnostics are required for this. The geometry of the CD detector can be improved by an addition of dead layers and electronic mechanisms. If one considers the simulated results of the outermost rings, then the value of performing an optimized, high-count run of the simulation are worth considering. GEANT4 simulations have been done at Center for High Performance Computing[7] [40] before, and similarly, future simulations built on this work will benefit considerably from the extra computing power offered at such facilities. The fits of the data used in this work served the purpose of comparing data sets to a reasonable accuracy. However, the comparison of the simulated and experimental data will be more precise if better functions can be found to fit the raw data. A tentative

---

[7] Jeyasingam Jeyasugiththan's current PhD work (University of Cape Town) on GEANT4 simulations have been simulated at CHPC

suggestion of the skew Gaussian function is made for a better goodness-of-fit.

With regards to the simulation of diamond detectors, it has been mentioned that more sophisticated methods are required for simulating such devices. These include the use of the so-called scoring mesh that tracks physical quantities in numerous cell-like volumes inside the detector. Quantities such as surface charge, number of terminated tracks (particles that were stopped), and a variety of others can be obtained for any position in the detector volume. To test a detector fully, its method of operation needs to be understood in terms of these quantities. If it is known what the prerequisites for a functional detector are, then the implementation and testing of such a device in GEANT4 is, in principle, straightforward. Future deposition of diamond layers through the hot-wire technique at the University of the Western Cape will benefit from more detailed simulations of a double sided diamond CD detector. Such developments will eventually expand the possibilities of running experiments with heavy ion beams at iThemba LABS.

The broadening of the peaks due to the increase in apparent thickness of the target due to the scattering angle is observed in the simulated spectra, but the values of the FWHM were not comparable to what was found experimentally. Reasons for this were suggested in section 6. Briefly, the additional broadening is due to the detector instrument. Incorporating the effects observed in a real particle detector in GEANT4 requires further investigation. An alternative to simulating the additional broadening due to the detector is also plausible; a typical alpha-source may be used to obtain an energy spectrum of a specific particle detector - in this case the silicon S3 CD detector. A simulation of this situation may then be carried out in GEANT4, and by comparing the resulting energy spectra, a broadening factor may be extracted from the relationship between the two sets of data. In any case, for the purpose of tagging the elastic peak, as discussed in section 1, a very accurate and efficient method of obtaining the elastic peak shape is required for the process to be beneficial.

In section 1 the motivation for simulating elastic peaks was given. In short, a very accurate simulation of the position and shape of these elastic peaks would permit a more accurate study of the inelastic peaks - as was illustrated in figure 3. Overall, the study of nuclear shapes would benefit from such simulations. A high measure of accuracy is required of the simulation in order to fulfill these purposes, and further refinements to the simulation may provide this.

The future analysis of the γ-ray spectrum obtained through the experiment will be discussed briefly. A spectrum obtained during the experiment is shown in figure 51. Particle spectra are to be calibrated by an α-source of ^{239}Pu, ^{241}Am and ^{244}Cm together with kinematics considerations for the scattered ^{12}C ions; both including energy losses in the ^{194}Pt target and the 0.58-mg/cm^2 thick ^{197}Au coating on the silicon strips. An additional particle-energy condition, $\mid E_{ring} - E_{sector} \mid \leq 350$ keV, will account for the energy sharing between the rings and sectors and dead layers in the silicon detector. Application of this energy condition cleans up the low- and intermediate-energy regions of the particle spectra enabling a particle energy selection of the ^{12}C inelastically scattered particles.

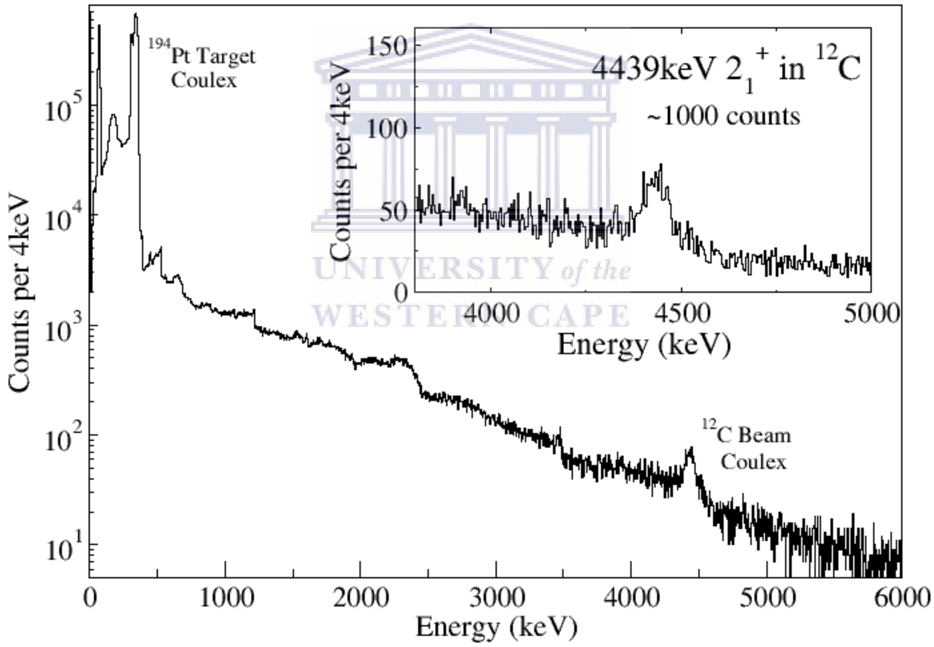

Figure 51: A raw γ-ray spectrum obtained with the TIGRESS spectrometer at TRIUMF for ^{12}C incident on ^{194}Pt @ 59.7 MeV.

During the offline sorting, a particle-γ coincidence condition can be satisfied by requiring a germanium hit and a hit in both the θ ring and ϕ sector of the silicon detector within a time window of 195 ns. Background γ-rays from the experimental hall, beam-dump decays and interactions can be suppressed by requiring a particle-γ coincidence condition. Events with germanium hits outside of this window are considered to be random coincidences and background subtracted. This coincidence technique has been utilized successfully in previous TIGRESS/BAMBINO experiments.

The relative angle between the registered particle in the silicon detector and the γ- ray is determined using the geometric center of the hit segment in the TIGRESS clovers. In the case of multiple crystals triggering in the same module, the crystal with the highest deposited energy is identified and the center of the segment with the highest energy within that crystal is used to Doppler correct the add-back energy.

The application of a particle energy condition, $\mid E_{ring} - E_{sector} \mid \leq 350$ keV will account for the energy sharing between the rings and sectors and dead layers in the silicon detector. This energy condition enables a particle energy selection of the inelastic peak. This same energy sharing condition as well as a broad particle-energy selection, which includes both inelastic and elastic peaks, will be employed to ensure full collection of the 328 keV γ-ray transition in ^{194}Pt.

Following the methodology described above, a study of the Coulomb excitation reaction by analysis of data from the TIGRESS γ-ray spectrometer and the double sided silicon S3 CD detector will be carried out. The use of GEANT4 as an aid to the particle-γ coincidence conditions will be explored further. In this way, through obtaining accurate, clean γ-ray spectra at different angles, the spectroscopic quadrupole moment of the first excited state of ^{12}C may be measured with sufficient accuracy to draw conclusions about its nuclear deformation.

A Building a Simulation in GEANT4

The fundamentals of practically building a GEANT4 application are described herein. A GEANT4 user should be able to replicate and build upon the simulation presented in this thesis by following this section. The general process a new user should go through is to pick an example given in the GEANT4 package that is as similar to the desired simulation as possible, and then edit the relevant parts. The simulation of the CD detector was done by using the built-in novice example N03, but many of the examples serve as good starting points. The examples shown in this section are either from the source code used for the simulation of the CD detector, or from the GEANT4 manual for application developers. Many other examples are provided by the GEANT4 manual in addition to the built-in examples provided with the GEANT4 package. GEANT4.10.0 was used for this work.

It is worth noting that GEANT4.8 and GEANT4.9 were used at the outset of this project and that the simulation carried out in this work was technically impossible to do with these versions. The problems associated with performing the simulation in these versions are documented in appendix B.1.

A.1 Geometry

The detector geometry in GEANT4 is made of a number of logical and physical volumes. Everything that happens during the simulation happens inside a (virtual) World volume. This World volume must contain, with some margin, all other volumes used in the detector geometry. The World volume is usually a box.

Each volume is given different attributes regarding its shape, materials, electronic structure, particulars of visualization and other user defined properties. It is then given a position within the world volume by placing it inside any existing volume and specifying its coordinates relative to its containing volume. These two volumes are labeled as the “daughter” and “mother” volume respectively. The World volume can also be a mother volume. One exception to this process is the World volume which doesn’t have a mother.

A volume is given a shape and dimensions in GEANT4 by creating a geometrical object called a solid. One chooses from a predefined library of solids (box, torus, cone, cylinder, trapezoid, etc.) in GEANT4 and then assigns a name and different parameters to the solid. For example, to create a box that serves as the world volume the following code is added to the detector construction part in the source file:

```
G4double worldX = 1.0*m;
G4double worldY = 0.5*m;
G4double worldZ = 0.5*m;

G4Box* worldS
        = new G4Box(”world”, worldX, worldY, worldZ);
```

This creates a box named “world” that extends from -1.0 meters to +1.0 meters along the X axis, from -0.5 meters to +0.5 meters along the Y axis and from -0.5 meters to +0.5 meters along the Z axis. It should thus be noted that the actual dimensions of this (and any) volume are twice the input parameters.

In addition to the physical, solid volume, a “logical volume” needs to be defined for this World volume. The logical volume is primarily used to specify the material of the created volume, but more advanced attributes can also be assigned using this built-in GEANT4 class. Below the code that specifies the solid volume, the following is added to fill the volume with a vacuum:

```
G4LogicalVolume* worldLV
    = new G4LogicalVolume(worldS, vacuum, ”World”);
```

This creates a logical volume named “worldLV” for the World box that contains all the attributes of the box.

The final step required to complete the construction of this volume is to place it. Since the current example is the World volume, it won’t be placed inside any other volume:

```
G4LogicalVolume* worldPV
        = new G4PVPlacement(0, G4ThreeVector(),
        worldLV, ”World”, 0, false, 0, fCheckOverlaps);
```

The first 7 parameters passed to the GEANT4 class G4PVPlacement are: The rotation of the solid, its translation position relative to its mother, its logical volume, its name, its mother volume, any relevant boolean operations and its copy number. Zero is passed as the fifth parameter since the World volume doesn’t have a mother. An additional argument, fCheckOverlaps, has been added to the class to explicitly check that there are no overlaps between logical volumes. This function has been created specifically for this simulation and is thus non-standard, so it should normally be omitted by the user since G4PVPlacement expects only 7 parameters. It is however very useful and relatively common as it is the most efficient method of checking whether the geometry is correct, therefore it is highly recommended.

The other two volumes used in the simulation, the ^{194}Pt target and the CD detector, are also included in this section. Below is the code for the ^{194}Pt target:

```
G4double targetRadius = 1.*cm;
G4double targetLength = 0.0007*mm;
```

Note that the radial size of the target has been greatly increased for visualization purposes. The actual length of the target will be twice the value passed on to the GEANT4 class tubs, as was the case with the box example at the beginning of the section.

```
G4ThreeVector positionTarget = G4ThreeVector(0, 0, −1.94*cm);
G4Tubs* targetS
        = new G4Tubs(”target”, 0., targetRadius, targetLength, 0.*deg, 360.*deg);
```

Once again, the definition of the solid volume is followed by defining its logical volume and then its placement. Note the slight difference in the definition here and the one above for the World volume. For any volume other than the World volume, the usage of G4PVPlacement is done in the following way:

```
fLogicTarget =
        new G4LogicalVolume(targetS, fTargetMaterial, ”TargetLog”, 0, 0, 0);
        new G4PVPlacement(0, positionTarget, fLogicTarget, ”TargetPhy”,
        worldLV, false, 0, fCheckOverlaps);
```

From the above it can be seen that the mother volume of the target is the World volume. Defining the CD detector is more complicated than the above example, since there are 24 rings and 32 sectors, there are thus 768 individual detector segments. Instead of having very complicated code to implement this, two separate simulations - one for the rings and one for sectors, were done. This was done by using the tubs class and, for the rings, incrementing the inner and outer radius of the tub class 24 times, while the sectors are simulated by incrementing over the angle 32 times. It is worth mentioning that one cannot simply create a loop and increment these volumes in the obvious way; The method for doing this properly in GEANT4 is to use the parameter, copy number, that is passed when creating a logical volume. Following convention, the detector is referred to as “tracker” throughout the code. The code for the detector rings is included below:

```
G4ThreeVector positionTracker
        = G4ThreeVector(0, 0, 0);
G4Tubs* trackerS
        = new G4Tubs(”tracker”, 0, 6*cm, 0.3*cm, 0.*deg, 360.*deg);
G4LogicalVolume *trackerLV
        = new G4LogicalVolume(trackerS, vacuum, ”TrackerLog”, 0, 0, 0);
        new G4PVPlacement(0, positionTracker, trackerLV, ”TrackerPhy”,
        worldLV, false, 0, fCheckOverlaps);
```

The CD detector needs to be made “sensitive”. This means that the tracking of particles and their energy loss at each step of the simulation is available to the user. This is done as by invoking the GEANT4 sensitive detector manager. In the code below “SD” refers to sensitive detector:

```
G4String trackerChamberSDname
        = ”TrackerChamberSD”
TrackerSD* aTrackerSD
        = new TrackerSD(trackerChamberSDname,
        ”TrackerHitsCollection”);
G4SDManager :: GetSDMpointer()
        − > AddNewDetector(aTrackerSD);
```

The following code creates the 24 rings of the CD detector and the 0.58 mg/cm^2 gold layer:

```
    for(G4intcopyNo = 0; copyNo < 25; copyNo + +) {

        if(copyNo < 24){

            G4double Zposition = 0.0;
            G4double innerRadius = 1.148*cm+
                copyNo*0.0886*cm + copyNo*0.01*cm;
            G4double outerRadius = 1.148*cm + copyNo*0.0886 ∗ cm+
                copyNo*0.01*cm + 0.0886*cm;
            G4Tubs* chamberS
```

```
                = new G4Tubs(”chamber”, innerRadius,
                outerRadius, 0.07.*mm, 0.*deg, 360.*deg);
        fLogicChamber[copyNo]
                = new G4LogicalVolume(chamberS,
                fChamberMaterial, ”ChamberLog”, 0, 0, 0);
        fLogicChamber[copyNo]
            − > SetSensitiveDetector(aTrackerSD);
        rmaxIncr = 0.5*(lastLength − firstLength)/(23);
        new G4PVPlacement(0, G4ThreeVector(0, 0, Zposition),
                fLogicChamber[copyNo], ”ChamberPhy”,
                trackerLV, false, copyNo, fCheckOverlaps);
    }
    if(copyNo = 25){

        G4double rmax = rmaxFirst + copyNo ∗ rmaxIncr;
        G4double innerRadious = 0.9 ∗ cm;
        G4double outerRadious = 1.2 ∗ cm + copyNo ∗ 0.2 ∗ cm;
        G4double halfWidth = 0.00030052/2 ∗ mm;
        G4double Zposition = −0.07 − halfWidth ∗ mm;

        G4Tubs* chamberS
             = new G4Tubs(”chamber”, innerRadius,
                outerRadius, 0.07*mm, 0. ∗ deg, 360. ∗ deg);

        fLogicChamber[copyNo] =
            new G4LogicalVolume(chamberS,
                fChamber2Material, ”ChamberLog”, 0, 0, 0);
            new G4PVPlacement(0, G4ThreeVector(0, 0, Zposition),
                fLogicChamber[copyNo], ”ChamberPhy”,
                trackerLV, false, copyNo, fCheckOverlaps);

    }
}
```

The above constitutes the entire geometry for the simulation and serves as an example for creating any other volumes that the user requires. The last *if statement* creates the gold layer implanted on the silicon. How materials assigned to variables such as **fChamberMaterial** are defined is shown in the next section.

A.2 Materials

GEANT4 allows the user to specify any material for the geometrical objects defined in the detector construction. This is done by either using one of the preconstructed elements, isotopes or materials, or by constructing new materials through these three classes: **G4Isotope**, **G4Element** and **G4Materials**.

The **G4Isotope** class describes the properties of isotopes:

- Atomic number
- Number of nucleons
- Atomic mass
- Shell energy
- Quantities such as cross section per atom, etc.

An example of an isotope definition is shown by the following code:

```
G4Isotope* isoU235
      = new G4Isotope(”U235”, 92, 235, 235.01*g/mole);
```

This creates the isotope ^{235}U with atomic number 92, 235 nucleons and an atomic mass of 235.01 g/mole.

The **G4Element** class describes the properties of elements:

- Effective atomic number
- Effective number of nucleons
- Effective mass per mole
- Number of isotopes
- Shell energy
- Quantities such as cross section per atom, etc.

An example of an element definition is shown by the following code:

```
G4Element* elH
        = new G4Element(”Hydrogen”, ”H”, 1, 1.01*g/mole);
```

This creates the element named Hydrogen with symbol “H”, atomic number 1 and an atomic mass of 1.01 g/mole.

An element can also be created from isotopes with different relative abundances. An example of an element definition from isotopes is shown by the following code:

```
G4Element* elU
        = new G4Element(”enrichedUranium”, ”U”, 2);
        elU− > AddIsotope(U5, abundance = 90.*percent;
        elU− > AddIsotope(U8, abundance = 10.*percent;
```

This creates the element “enriched Uranium” with symbol “U” and two components: 90% isotope U5 (Uranium-235) and 10% isotope U8 (Uranium-238).

The **Materials** class describes the macroscopic properties of matter:

- Density
- State
- Temperature
- Pressure
- Macroscopic quantities like mean free path, stopping powers dE/dx etc.

An example of a material definition is shown by the following code:

```
density = 2.33*g/cm^3;
a = 28.09*g/mole;
G4Material*Si
        = new G4Material(”Silicon”, 14, a, density);
```

This creates the material silicon.

Another method for creating a material is to define different chemical molecules by their elemental components and then defining a mixture in terms of the fractional mass of each of these molecules. The gas molecule $C0_2$ is defined in this way below:

```
density = 27.*g/cm3;
pressure = 50.*atmosphere;
temperature = 325.*kelvin;
G4Material* C02
        = new G4Material(”C02”, density,
        2, kStateGas, temperature, pressure);
C02− > AddElement(elC, 1;
C02− > AddElement(elO, 2);
```

This creates the $C0_2$ molecule by defining the appropriate density, chemical composition, state, temperature and pressure.

To conclude this section, the code showing how the 96.5% enriched ^{194}Pt target was created is included below:

```
G4Isotope* isoPt194 = newG4Isotope(”Pt194”, 78, 194);
G4Element* Pt = newG4Element(”Platinum”, ”Pt194”, 1);
Pt− > AddIsotope(isoPt194, 100.*perCent);

G4Isotope* NisoPt194 = newG4Isotope(”NPt194”, 78, 195);
G4Element* NPt = newG4Element(”NPlatinum”, ”NPt194”, 1);
NPt− > AddIsotope(NisoPt194, 100.*perCent);

G4Material* TPlatinum = newG4Material(”TPlatinum”, 21.45*g/cm3, 2);
TPlatinum− > AddElement(Pt, 3.5*perCent);
TPlatinum− > AddElement(NPt, 96.5*perCent);
```

Using the definitions shown thus far, the following statement is made to assign a specific, created, material to a variable:

```
fTargetMaterial = TPlatinum
```

A.3 Particles

The following types of particles can be defined and used in a GEANT4 simulation:

- ordinary particles, such as electrons, protons and gammas
- resonant particles with very short lifetimes, such as vector mesons and delta baryons
- nuclei, such as deuterons, alpha particles and heavy ions (including hyper nuclei)
- quarks, di-quarks and gluons

The particles to be used in a simulation are defined in the *PhysicsList* part of the program. There are three class definitions to be made for each particle type that is used; Each of these characterizes a different aspect of the particle's properties. **G4ParticleDefinition** contains the static information of the particle, such as its name, mass, spin, life time and decay mode. **G4DynamicParticle** contains the dynamic information, such as its energy, momentum, polarization and proper time. **G4Track** contains information necessary for tracking a particle during a simulation, such as time, position and step length.

Particles are organized into six major categories:

- leptons
- mesons
- baryons
- bosons
- ions
- short-lived particles

The user is also free to define any type of particle, such as the geantino that was defined in section 4.1.2.

A.4 Physics Processes

At each step of a simulation, GEANT4 references a vast set of data libraries to determine the appropriate evolution of the simulation. This is done by specifying the desired physics processes in the *Physics List* part of the program. There are seven major categories for the user to choose from:

- electromagnetic
- hadronic
- transportation
- decay
- optical
- photolepton-hadronic
- parameterization

The user can customize this aspect of the simulation to a large degree. For instance, the *logical volumes* defined in the *detector construction* part of the program can each have their own applied physical process. Pre-defined physics lists are available for use and are the easiest to implement, but the user is free to create his own custom physics list.

The physics list *standardNR* was used for the simulation in this work. Many other pre-defined physics lists were tried first with little success, and $StandardNR$ also gave incorrect results with the older GEANT4.9.6. The user is free to activate the desired process by defining it in the actual C++ code, or the physics list may be referenced in batch mode or even in the script file (such as the run.mac files in every example). This is very simply done by the command:

/Physics/addPhysics standardNR

Note that this method only works for pre-defined physics lists.

A.5 User Action Classes

Along with the mandatory user action classes, there are five, optional, user "hook" classes. These optional classes enable the user to output and store data from a simulation run. These optional classes are described below:

G4UserRunAction

This class enables the user to perform actions at the beginning and end of each run. Its uses include setting variables which affect the physics table, initializing histograms and analyzing the results from the processed run at its end.

G4UserEventAction

This class enables the user to perform actions at the beginning and end of each event. Uses for this include initializing and writing data to histograms, or to analyze the results of each event.

G4UserStackingAction

By using this class, the user can control the various stacking mechanisms and customize access to the track stacks.

G4UserTrackingAction

This class is instantiated whenever a track is created or completed. It can be used to decide whether a particular trajectory should be stored by comparing it to a set of predefined trajectories and thereby save memory and computational time. Analysis of a track can also be processed upon its completion.

G4UserSteppingAction

This class can be used to customize the behaviour of the simulation at the end of each step, or simply to analyze what is happening in the simulation during each step.

The data analysis package, ROOT [27], was used to obtain data from the CD detector simulation. ROOT is built to be compatible with GEANT4, and there are built in GEANT4 classes for instantiating a ROOT output. Briefly, the ROOT histogram was created at the beginning of each *run*, while the energy deposited in each ring was added up after each *step*. At the end of each *event* the total energy deposited during that event is sent to a user created class *RootAnalysis* which fills up the histogram. This method is much more complicated to implement than simply outputting the energy deposited to text files. The reason it was done in this way was to keep all the data from the simulation in one file as opposed to having a separate file for each sector and ring. This is possible due to ROOT storing data in a so-called *ntuple*[8]. Fitting functions is simple in ROOT due to the built-in MINUIT [28] minimization package. Various data analysis functions such as this are incorporated into ROOT, and this type of functionality thus makes ROOT a very effective environment for the data output of a simulation. With ROOT it is also possible to view an energy spectrum mere seconds after the simulation is completed.

---

[8] A tuple is a data structure that has a specific number and sequence of elements. ROOT calls its tuples *ntuples*.

B GEANT4 Troubleshooting

A user may encounter many erroneous results in the course of performing GEANT4 simulations. The major difficulties encountered in the course of this work are documented in this section. In section B.1 the failed attempt to concurrently simulate (using versions of GEANT4 prior to GEANT4.10) Rutherford scattering and energy loss due to the stopping power of the target is discussed. In section B.2 a user mistake and the discovery of the solution is documented.

B.1 Simulations using GEANT4.9

The results of performing the simulation in GEANT4.9 is shown in figure 52. The only difference between the energy spectra obtained for the different rings are the amount of counts in the peaks, i.e. the cross sections. The peaks are not shifted to lower energies at larger scattering angles and the broadening of all the peaks is identical. The peaks are also found at the improbable energy of ≈37.5 MeV. Clearly the results are nonsensical.

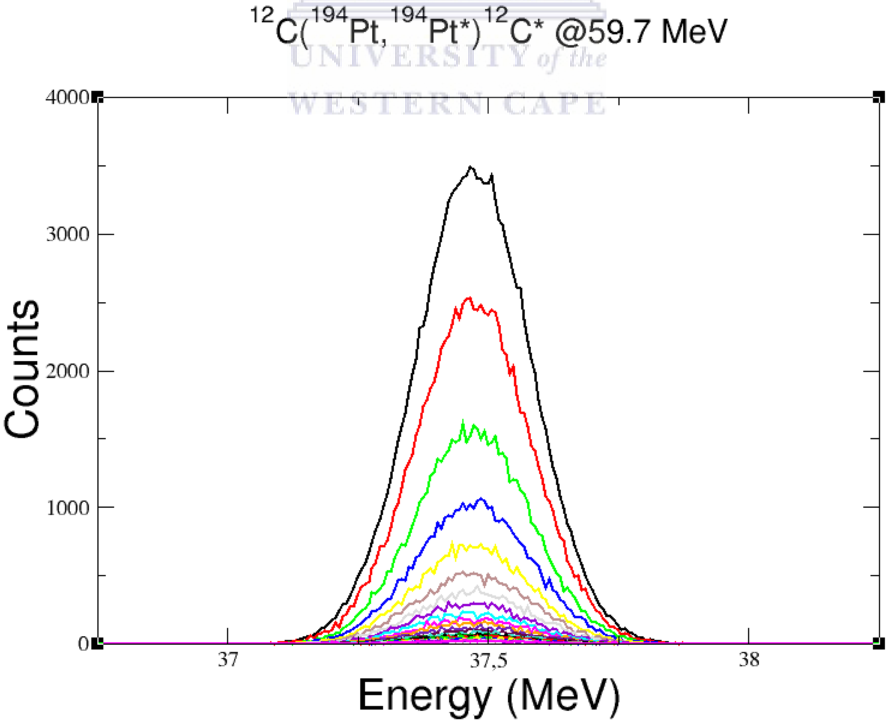

Figure 52: Simulation of the silicon CD detector in GEANT4.9.

The reason for these results was only found when the simulation was presented to Dr. Alexander Howard who is part of the group that develops and maintains GEANT4: versions 8 and 9 of GEANT4 were never tested for particle detection of this kind and were not simulating the physical processes correctly. Version 10 only launched late 2013, and this led to a delay of this work. GEANT4 users should thus investigate whether the simulation they are attempting to write is viable, i.e. something similar has been done successfully, before undertaking the task. Previously, a user would have had to rewrite the GEANT4 source code or have implemented a novel solution to the problem to obtain sensible results.

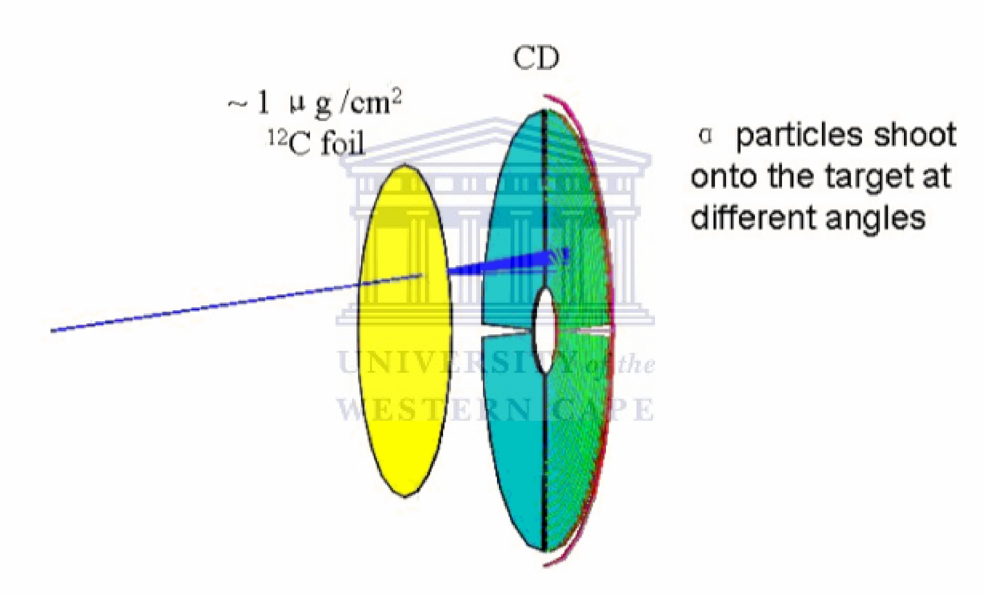

Figure 53: An example of incident particles directed at a specific ring element as opposed to a proper simulation of Rutherford scattering in the target [37].

In simulations of particle energy detectors where Rutherford scattering is of importance, the method of shooting the incident particles at different angles through the target has been used previously [37]. This method is an *artificial* way of simulating elastic Rutherford scattering and has inherent limitations. When choosing a scattering angle corresponding to the center of a detector element, say a ring as in the CD detector, then all scattering angles that would result in the particle being detected in the ring are omitted except the angle corresponding to the very center of the ring. Moreover, in such a simulation the scattering position in the target has to be assumed. The results of using this method are therefore incorrect on account of these two simplifications. A visualization of such a simulation is shown in figure 53. In a very practical sense, the simulation would, in the case of the silicon S3 CD detector, have to be repeated 24 times - once for each scattering angle. More importantly, the very use of GEANT4 for such a simulation comes into question. The only benefit in using GEANT4 for such a simulation over much simpler methods such as SRIM calculations would be the spread of energies of the resulting energy spectrum. But this spread of the energy spectrum (measured in one specific ring) has, in and of itself, no value since it is not related to the spread one would find by experiment or proper simulation methods. An energy spectrum that is simulated properly has to take into account that elastic Rutherford scattering may occur anywhere inside the target and that particles may be detected at any position in the detector element. The probability of scattering (from the cross section of the interaction) everywhere in the target is not the same however, which is why such calculations are impractical without a powerful simulation environment such as GEANT4. For the two aforementioned reasons, the position of scattering in the target and the range of scattering angles corresponding to a specific detector element, such simulations hold little practical value as opposed to much simpler methods that offer the same results.

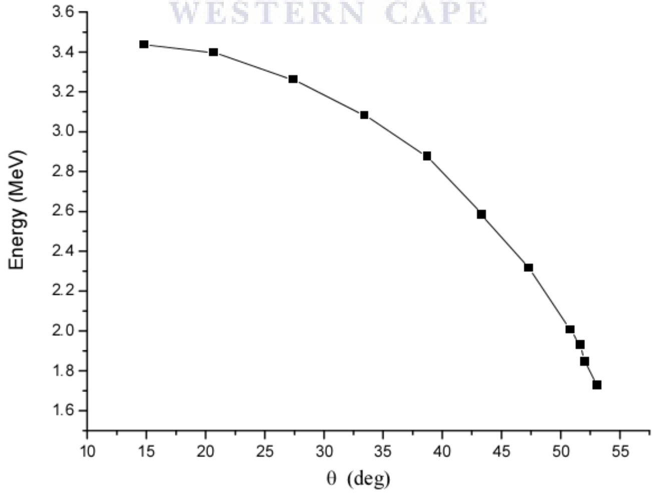

Figure 54: Energy measurements in a particle detector at various angles by varying the incident direction of the beam in GEANT4 [37].

In figure 54 the results of such an artificial simulation of Rutherford scattering in GEANT4 are shown. These results could be replicated by simply doing a SRIM calculation. This was, in fact, done in section 3.6. The spread in energy measured in each ring may also potentially be calculated by using the TRIM package.

A brief explanation of the reasons for the inability of older versions of GEANT4 to properly simulate what was done in this work is given here. Before GEANT4.10 there was an inconsistency between hadronic elastic scattering and multiple scattering models. Versions of GEANT4 older than GEANT4.8 may not have had this problem, but it is difficult ascertain this since there are four models that would have to be investigated - hadronic elastic, multiple scattering, single scattering and ionization energy loss that are shared across two working group categories (EM and hadronic). The usage of the single scattering model should have given correct results in earlier versions of GEANT4, but there would have been some form of double counting between the hadronic elastic and the electromagnetic scattering. Usage of multiple scattering models would also result in incorrect results as only the scattered particle's direction would be changed but not its energy.

B.2 Anomaly in Simulated Results of Ring A

During the course of analyzing the data obtained from the GEANT4 simulations, it was found that the energy peak simulated for ring A was higher than expected relative to the other peaks. Moreover, the amount of counts in this peak was larger than expected by a factor of about 2.5. These findings are indicated in figure 55. The reason for the anomaly will be presented in this section.

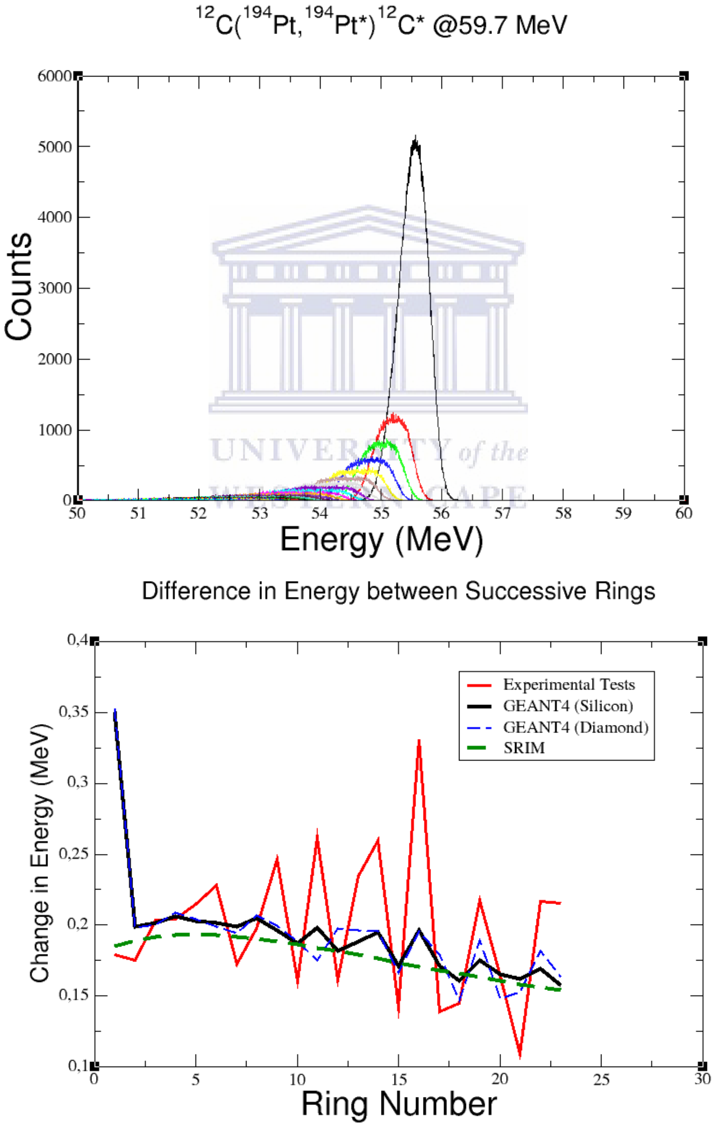
$^{12}C(^{194}Pt,^{194}Pt^*)^{12}C^*$ @59.7 MeV

Difference in Energy between Successive Rings

Figure 55: The faulty energy spectrum obtained from GEANT4 simulations (top panel) and the difference in energy in successive rings (bottom panel).

The reason for the erroneous results obtained from the simulation is the manner in which the detector geometry was constructed. Briefly, the detector was assigned a thickness that was too large and this influenced the data obtained for ring A. The CD detector was initially given a thickness of 25 mm. This was done for visualization purposes, but was not changed at a later stage because it was considered to not have any effect on the output of the simulation. It is not obvious that the thickness of the detector will influence the results, after all, all the particles are stopped in the detector in any case.

If we consider that the maximum amount of energy a particle should have when striking the CD detector is when it is scattered with the smallest possible angle by the target (see figure 56), then the thickness of the detector starts playing an important factor in the resulting spectra for ring A.

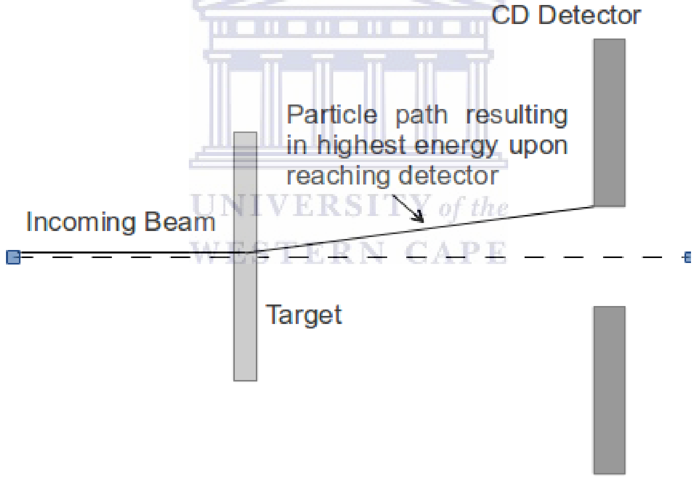

Figure 56: Shortest path of a scattered particle striking the front side of ring A.

The full width of each ring is 1 mm, but the apparent width of ring A is increased by the thickness of the CD detector. A particle may thus strike ring A on its inside and deposit its energy. This is visually represented in figure 57.

The effect of the overly thick detector was investigated and a discussion on the findings follows. Note that this investigation was carried out before the gold layer was added to the detector - the energies discussed will therefore be higher than what was eventually obtained through the simulations. Furthermore, the geometry of the simulation was not optimized yet according to exact factory specifications, so the width of each ring was specified as 1 mm. This has a small effect on the angles used in this calculation. Importantly, the relative energy positions between the peaks and their counts are the quantities of interest, therefore the unrefined version of the simulation is appropriate for this discussion.

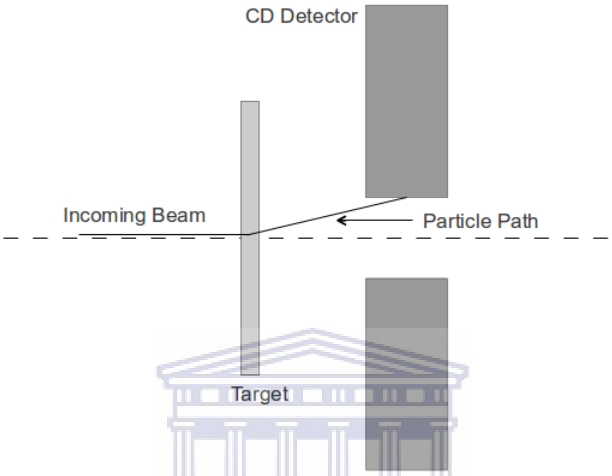

Figure 57: Scattered particles striking the inside of ring A.

The scattering angle corresponding to what the maximum energy should be upon reaching ring A (when striking the inner edge as in figure 56) is given by $\theta = 29.55°$. Performing SRIM calculations and considering the energy transferred due to Rutherford scattering for this scattering angle results in an energy of 55.25 MeV. The projected range of a 55.25 MeV ^{12}C particle in silicon, once again calculated with SRIM, is approximately 73 μm. This thickness would thus have been sufficient to stop any relevant particle in the detector completely.

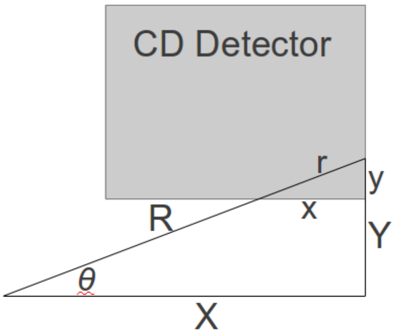

Figure 58: A diagram illustrating the methodology in establishing the apparent width of ring A for all particles completely stopped in its volume.

For the 25 mm thick CD detector, geometrical arguments can be used to find the highest energy particles that are completely stopped in the simulations, as well as the apparent thickness of the simulated CD detector for all particles that are stopped completely. Consider the geometrical representation of a the highest energy particle stopped completely in the detector as shown in figure 58. Particles that are not stopped in the detector are not of interest because the manner in which the scoring has been defined in the GEANT4 code is to only add the total energy lost to the relevant bin once the particles reaches zero energy. Therefore, particles scattered at angles smaller than θ as shown in figure 58 will not *be seen* by the detector. Hence the need for establishing theta to find the apparent thickness as illustrated in figure 59.

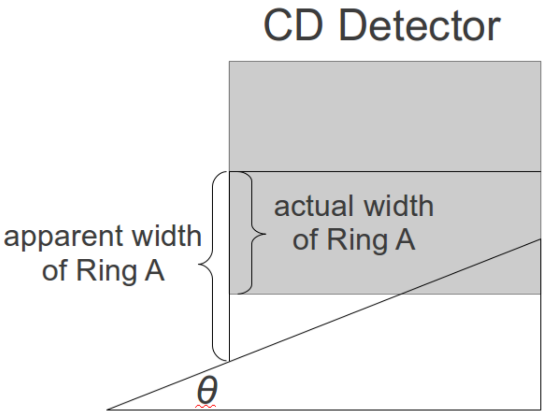

Figure 59: A diagram illustrating the apparent width of ring A. All particles scattered within this region will be completely absorbed and hence be represented by the simulation output.

In principle, this problem is solvable analytically when one consider that the path length of this particle in the detector, r, is dependent on its energy, which is in turn dependent on the scattering angle θ. Since the energy is larger for smaller angles of θ, the particle scattered at an angle θ which is stopped at the very end of the detector will have deposited the maximum amount of energy in the target. If $E_{scattered}$ is the amount of energy this particle has when reaching the detector, then one has to find the value of r such that $E_{scattered} + (dE/dr)r = 0$. This is a very complicated problem since $E_{scattered}$ is dependent on θ and r is also dependent on θ. Not only this, but from the Bethe equation (65) the value of (dE/dr) is shown to be dependent on E. To solve for r then would require solving the following:

$$E_{scattered}(\theta) + \frac{dE(E)}{dr} r(\theta) = 0 \tag{68}$$

Additionally, the value of $r(\theta)$ is found by considering the triangles in figure 58 with sides XYR and xyr. To calculate r the lengths of either x or y are required in addition to θ. Since these are similar, right-angled triangles, it follows that

$$\frac{Y}{X} = \frac{y}{x},\ \frac{Y}{R} = \frac{y}{r},\ \frac{X}{R} = \frac{x}{r},\ R^2 = X^2 + Y^2,\ r^2 = x^2 + y^2 \tag{69}$$

Since X (the distance from the target to the detector) and $Y - y$ (the radius of the hole in the detector) are known, the above can be solved for r as a function of θ and either x or y. This solution for r ends up being a 5th degree polynomial with a further dependence on θ since x and y are dependent on θ as well.

Instead of doing the above, an approximate solution is easier to find numerically. Furthermore, since the range of the incident particle in the detector for the energies in the simulation is of the order of tens of μm, while the detector has a thickness of 25 mm, this range (r in figure 58) is smaller than the dimensions of the detector by a factor of more than a thousand. The full thickness of the detector would thus serve for calculating the apparent thickness of the 25 mm thick CD detector to illustrate the erroneous data found for ring A. Nevertheless, r was found numerically by iterating over different scattering angles θ to find the corresponding energy $E(\theta)$, and then subtracting the energy lost due to equation 65 for the appropriate path length, $r(\theta)$, of the particle in the target. This results in $\theta \approx 26.74°$. Using this value of θ, the apparent width of ring A (visualized in figure 59) is found to be 2.23 mm.

The apparent thickness of ring A in the experiment for particles depositing all their energy in the detector is shown here to be roughly too big by a factor of 2. This explains the higher than expected energy found for the peak of the spectrum in ring A in the simulations relative to the other peaks, and the higher than expected count number.

The reasoning above can be validated by calculating the scattering cross sections for the angles corresponding to the apparent width of ring A as calculated in this section, and the actual width of ring A. Equations 25 and 41 derived in section 3.3 combine to give the scattering cross section of a projectile incident on any target nucleus. The scattering angle in the LAB frame, $\theta = 26.74$°converted to the CM frame is $\psi = 28.33$°. In the general case of a projectile with atomic number Z_p, this becomes

$$\frac{d\sigma}{d\Omega}(\psi) = \frac{Z_t^2 Z_p^2 k e^4}{16E^2} \frac{1}{sin^4(\psi/2)} \tag{70}$$

so that

$$\sigma = \left(\frac{\pi Z_t^2 Z_p^2}{4}\right)\left(\frac{ke^2}{E}\right)^2\left(\frac{1+cos\psi}{1-cos\psi}\right) \tag{71}$$

Here, Z_t refers to the atomic number of the target nuclus,E the energy of the projectile and e is the elementary charge constant. The scattering cross section is then calculated using the angle corresponding to the innermost part of the apparent and actual width of ring A, $\psi_{apparent} = 28.33°$ and $\psi_{actual} = 31.29°$. The ratio of these numbers describes the theoretical factor increase in counts due to an increased apparent width caused by making the CD detector too thick. If $\sigma_{apparent}$ and σ_{actual} are the scattering cross sections corresponding to $\psi_{apparent} = 28.33°$ and $\psi_{actual} = 31.29°$ respectively, then

$$\frac{\sigma_{apparent}}{\sigma_{actual}} = \frac{1.69 \times 10^{-4}}{1.38 \times 10^{-4}} = 2.66 \tag{72}$$

By vertically scaling down ring A with this obtained factor, figure 60 is obtained.

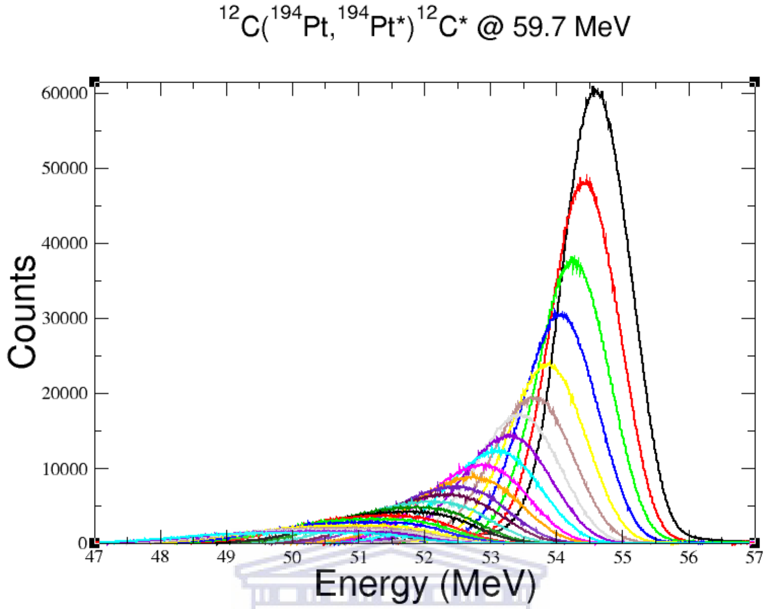

Figure 60: Result of vertically scaling ring A by the factor obtained in equation 72.

For further comparison, the ratio of the total counts of the experimental results and the GEANT4 simulations of rings A and B can be analyzed. In the experimental case,

$$\left(\frac{Counts_A}{Counts_B}\right)_{exp} = \frac{8150001}{6526448} \approx 1.25 \tag{73}$$

This ratio is what would be expected if ring A was simulated with an appropriate thickness. This is not exactly true of course, due to the presence of an inelastic peak and background in the experimental results, but since the elastic peak is considerably larger than these, it can be accepted as approximately true. For the (faulty) GEANT4 simulation of the CD detector,

$$\left(\frac{Counts_A}{Counts_B}\right)_{sim} = \frac{8150001}{6526448} \approx 3.64 \tag{74}$$

When dividing this result with the result of equation 72, the value of $\left(\frac{Counts_A}{Counts_B}\right)_{sim}$ is then corrected. Doing this,

$$\left(\frac{\frac{Counts_A}{Counts_B}{}_{sim}}{\sigma_{apparent}}\right)\sigma_{actual} \approx 1.37 \tag{75}$$

This value is comparable to what was found for equation 73 and thus validates the argument presented in this section for the anomalous size and energy of the peak in the simulated results of ring A. This section serves as an example of the effect the thickness of a simulated detector may have on the resulting data.

References

[1] K. Alder, A. Bohr, T. Huus, B. Mottelson and A. Winther, *Study of Nuclear Structure by Electromagnetic Excitation with Accelerated Ions*, Rev. Mod. Phys. **30**, 353 (1958).

[2] J. N. Orce *et al.*, *Reorientation-effect measurement of the* $\langle 2_1^+ \parallel \hat{E}2 \parallel 2_1^+ \rangle$ *matrix element in* ^{10}Be, Phys. Rev. **C 86**, 041303(R) (2012).

[3] C. H. Townes, *Determination of Nuclear Quadrupole Moments*, Hand. Phys. **8/38/1**, 377 (1958).

[4] K. Heyde, J.L. Wood, *Shape coexistence in atomic nuclei*, Rev. Mod. Phys. **83**, 1467 (2011).

[5] W.J. Vermeer *et al.*, *Electric quadrupole moment of the first excited state of* ^{12}C, Phys. Lett. **B122**, 23 (1983).

[6] A. N. Andreyev *et al.*, *A triplet of differently shaped spin-zero states in the atomic nucleus* ^{186}Pb, Nature **405**, 430 (2010).

[7] E. Rutherford, *The Scattering of* α *and* β *Particles by Matter and the Structure of the Atom*, Phil. Mag. **21**, 669 (1911).

[8] A. Ostrowski, S. Cherubini *et al.*, *CD: A double sided silicon strip detector for radioactive nuclear beam experiments*, Nucl. Instr. Meth. **A480**, 448 (2002).

[9] P. Rahkila *et al.*, *Shape coexistence at the proton drip-line: First identification of excited states in* ^{108}Pb, Phys. Rev. **C 82**, 011303 (2010).

[10] J. P. Svenne, R. S. Mackintosh, *Spin-orbit force and the deformation of* ^{12}C, Phys. Rev. **C 18**, 983 (1978).

[11] C. E. Svensson, P. Amadruz *et al.*, *TIGRESS: TRIUMF-ISAC gamma-ray escape-suppressed spectrometer*, J. Phys. G: Nucl. Part. Phys. **31**, S1663 (2005).

[12] GEANT4 Collaboration, S. Agostinelli, J. Allison *et al.*, *Geant4 - a simulation toolkit*, Nucl. Instr. Meth. **A506**, 250 (2003).

[13] R. Rujiwarodom, B. Asavapibhop, P. Sangpeng, *Study of Rutherford Scattering Cross Section via GEANT4 Methods*, Nat. Sci. **45**, 960 (2011).

[14] H.A. Bethe, *Zur Theorie des Durchgangs schneller Korpuskularstrahlen durch Materie*, Ann. Phys. **5**, 325 (1930).

[15] K. Fabisiak, E. Staryga, *CVD diamond: from growth to application*, JAMME, **37/2**, 264 (2009).

[16] K. Hibino, T. Kashiwagi *et al.*, *The Design of Diamond Compton Telescope*, Astrophys. Space Sci. **309.1**, 541 (2007).

[17] M. Bruzzi, H. F. Sadrozinski, A. Seiden, *Comparing Radiation Tolerant Materials and Devices for Ultra-Hard Tracking Detectors*, Nucl. Instr. Meth. **A594**, 754 (2007).

[18] P. Bergonzo, D. Tromson, C. Mer, *Radiation Detection Devices Made from CVD Diamond*, Semicond. Sci. Technol. **18.3**, S105 (2003).

[19] M. Landstrass, D. Fleetwood, *Total dose hardness of diamond-based silicon-on-insulator structures*, Appl. Phys. Lett. **56**, 2316 (1990).

[20] A. T. Collins, *Diamond electronic devices - a critical appraisal*, Semicond. Sci. Technol. **4**, 605 (1989).

[21] G. Soti *et al.*, *Performance of Geant4 in simulating semiconductor particle detector response in the energy range below 1 MeV*, Nucl. Instr. Meth. **A728**, 11 (2013).

[22] K .Amaka *et al.*, *Comparison of Geant4 electromagnetic physics models against the NIST reference data*, Trans. Nucl. Sci. **42.4**, 910 (2005).

[23] J. Biersack, L. Haggmark, *A Monte Carlo computer program for the transport of energetic ions in amorphous targets*, Nucl. Instr. Meth. **174**, 257 (1980).

[24] C. Wrede *et al.*, *A double sided silicon strip detector as a DRAGON end detector*, Nucl. Instr. Meth. **B204**, 619 (2004).

[25] H. Paul, A Schinner, *Judging the reliability of stopping power tables and programs for heavy ions*, Nucl. Instr. Meth. **B209**, 252 (2003).

[26] A. Lechner *et al.*, *Validation of recent Geant4 physics models for application in carbon ion therapy*, Nucl. Instr. Meth. **B268**, 2343 (2010).

[27] R. Brun, F Rademakers, *ROOT - An object oriented data analysis framework*, Nucl. Inst. Meth. **A389**, 81 (1997).

[28] F. James, M. Roos, *Minuit - a system for function minimization and analysis of the parameter errors and correllations*, Comput. Phys. Commun. **10.6**, 343 (1975).

[29] T. Czosnyka, *et al.*, *E2 properties of the ground state band in ^{248}Cm*, Nucl. Phys. **A458**, 123 (1986).

[30] A. Howard, *et al.*, *Validation of Geant4 against the TARC benchmark and new developments in PreCompound/De-Excitation modelling*, PSI, Switzerland: 1st Workshop on Accelerator Radiation Induced Activation (2008).

[31] J. Ziegler *et al.*, *Handbook of the Range Distributions of Energetic Ions in All Elements*, New York: Pergamon Press (1980).

[32] J. Ziegler *et al.*, *SRIM - The Stopping and Range of Ions in Matter*, Pennsylvania: SRIM Co. (2008).

[33] S. T. Thornton, J. B. Marion, *Dynamics of Particles and Systems*, 5th ed. California: Thomson Brooks Cole (2003).

[34] G. F. Knoll, *Radiation Detection and Measurement*, New Jersey: John Wiley and Sons (1979).

[35] W. R. Leo, *Techniques for Nuclear and Particle Physics Experiments*, Berlin: Springer-Verlag (1987).

[36] B. Stroustrup, *The C++ Programming Language*, Boston: Addison-Wesley Professional (2000).

[37] J. Chen, *GEANT4 Simulations and Experimental Tests of a Silicon Cd Detector*, Ontario: McMaster University (2006).

[38] SRIM release notes, http://www.srim.org/SRIM/SRIM2011.htm/ [22.05.2014]

[39] CERN - The Center European Organization for Nuclear Research, http://cern.ch/ [22.05.2014]

[40] CHPC - The Center for High Performance Computing, http://chpc.ac.za/ [22.05.2014]